

UNIVERSITA' DEGLI STUDI DI VERONA

DEPARTMENT OF

Diagnostics and Public Health

GRADUATE SCHOOL OF

Natural Sciences and Engineering

DOCTORAL PROGRAM IN

Nanoscience and Advanced Technologies

Cycle / year XXXII / 2016

LIGHT EMITTING FUNCTIONALIZED POROUS SILICON MICROPARTICLES AS
MULTIMODAL SYSTEM IN THERANOSTICS

S.S.D. FIS/01 – Experimental Physics

Coordinator: Prof. Franco Tagliaro

Tutor: Prof. Nicola Daldosso

Doctoral Student: Dott.ssa Elena Chistè

Quest'opera è stata rilasciata con licenza Creative Commons Attribuzione – non commerciale
Non opere derivate 3.0 Italia . Per leggere una copia della licenza visita il sito web:

<http://creativecommons.org/licenses/by-nc-nd/3.0/it/>



Attribuzione Devi riconoscere una menzione di paternità adeguata, fornire un link alla licenza e indicare se sono state effettuate delle modifiche. Puoi fare ciò in qualsiasi maniera ragionevole possibile, ma non con modalità tali da suggerire che il licenziante avalli te o il tuo utilizzo del materiale.



NonCommerciale Non puoi usare il materiale per scopi commerciali.



Non opere derivate —Se remixi, trasformi il materiale o ti basi su di esso, non puoi distribuire il materiale così modificato.

Light emitting functionalized porous silicon microparticles as multimodal system in theranostics – Elena Chistè

Tesi di Dottorato

Verona, 10 Dicembre 2019

ABSTRACT

Porous silicon (pSi) is a sponge-like material obtained by anodic porosification of a crystalline silicon wafer in HF; pSi microparticles can be obtained by sonication of the porous layer. This material is characterized by exclusive intrinsic properties that make it suitable for theranostics (i.e. the combination of therapy and diagnostic) with a faster and more specific response to the disease for each patient (i.e. personalized medicine). Due to a quantum confinement effect, this material was found to be photoluminescent at room temperature, allowing its traceability by optical imaging in-vitro and in-vivo. The electrochemical etching produces a material with a high surface to volume ratio, making pSi very attractive as a carrier, in perspective of drug loading and release. Furthermore, the ability to functionalize the surface is essential for the conjugation with other agents (molecules, dyes, magnetic nanoparticles, among all) and for further applications (contrast agent in magnetic resonance imaging and for photothermal and photodynamic therapy).

Optical properties and porosity, together with the biodegradability, the biocompatibility and the absence of immunogenicity are the major characteristics to exploit porous silicon microparticles as a multifunctional system in theranostics. Some of its limitations are related to (i) the broad size distribution, due to the top-down fabrication approach, and (ii) its degradation in aqueous media that causes a photoluminescence quenching.

One of the aims of this PhD thesis work was to overcome these limiting issues in an original and effective approach: (i) an ultrasonic post-functionalization treatment and (ii) an inorganic coating based on TiO₂ deposition have been experimentally validated, respectively.

Once fabrication and functionalization protocols are well addressed (first objective of this experimental work), pSi has several potentialities to be improved, for example, combining further diagnostic or therapeutic functionality. Along this direction, the second objective of this thesis work, the more applicative one, was the study about adding magnetic properties to this material by infiltrating and attaching magnetic nanoparticles inside its pores. As a fundamental step for the reliability in theranostics, the interaction with human immune cells is explored to evaluate the internalization mechanism, the biocompatibility and the immunogenicity of this

system. To complete the trajectory towards theranostics, preliminary results about the employment of pSi microparticles as immune adjuvant delivery are presented, in the perspective of immunotherapy. It is possible, that the presentation of these molecules carried by the microparticles could lead to enhanced cell activation, with respect to the presentation of the soluble molecule.

SOMMARIO

Il silicio poroso è un materiale con una struttura simile alla spugna, che si ottiene dalla porosificazione di fette di silicio cristallino in soluzione acida. Un'ulteriore sonicazione permette di frammentare lo strato superficiale e ottenere microparticelle porose. È un materiale caratterizzato da proprietà intrinseche molto interessanti in prospettiva di applicazioni teranostiche, neologismo che definisce l'unione di terapia e diagnostica, con risposta più veloce e specifica al trattamento in pazienti diversi (medicina personalizzata). L'intensa luminescenza a temperatura ambiente, causata dal confinamento quantico, favorisce il suo utilizzo come tracciante in imaging ottico sia in-vitro che in-vivo. L'etching elettrochimico produce un materiale poroso con grande area superficiale e lo rende interessante per essere utilizzato come vettore per il rilascio controllato di farmaci. Inoltre, la possibilità di funzionalizzare la superficie è essenziale per la coniugazione di altri materiali (molecole, coloranti, nanoparticelle magnetiche, tra le altre) e ulteriori applicazioni (traccianti in risonanza magnetica e terapia fototermica e fotodinamica). Le peculiari proprietà ottiche e strutturali, assieme alla biodegradabilità, biocompatibilità e assenza di immunogenicità, rendono questo materiale molto interessante come sistema teranostico multifunzionale. Alcune limitazioni sono legate (i) all'ampia distribuzione di taglia, dovuta al tipo di fabbricazione delle microparticelle, e (ii) alla degradazione della fotoluminescenza dovuta all'ossidazione in ambienti biologici acquosi.

Uno dei principali temi trattati nella tesi di dottorato riguarda la risoluzione di questi problemi con un approccio originale e efficiente: (i) un trattamento ad ultrasuoni post-funzionalizzazione e (ii) la deposizione di un coating inorganico (TiO_2) sono stati validati sperimentalmente.

Dopo aver messo a punto dei protocolli di fabbricazione e funzionalizzazione (primo obiettivo del lavoro sperimentale), il silicio poroso ha diverse potenzialità

che possono essere migliorate, ad esempio aggiungendo altre funzionalità diagnostiche e terapeutiche. Un focus più applicativo del presente studio (secondo obiettivo), riguarda l'aggiunta di funzionalità magnetiche, tramite l'infiltrazione di nanoparticelle magnetiche nei suoi pori.

Essendo un passaggio fondamentale in prospettiva di applicazioni teranostiche, è necessario uno studio sull'interazione delle microparticelle con le cellule del sistema immunitario: vengono valutati il meccanismo di internalizzazione, la biocompatibilità e l'immunogenicità di questo sistema. Per completare lo studio da un punto di vista applicativo, sono riportati alcuni risultati preliminari, riguardanti l'utilizzo delle microparticelle per il trasporto di adiuvanti immunitari in vista di studi di immunoterapia. In particolare, è possibile che la presentazione di adiuvanti immunitari portati dalle microparticelle scateni una risposta cellulare maggiore rispetto alla presentazione delle molecole da sole.

GRAPHICAL ABSTRACT

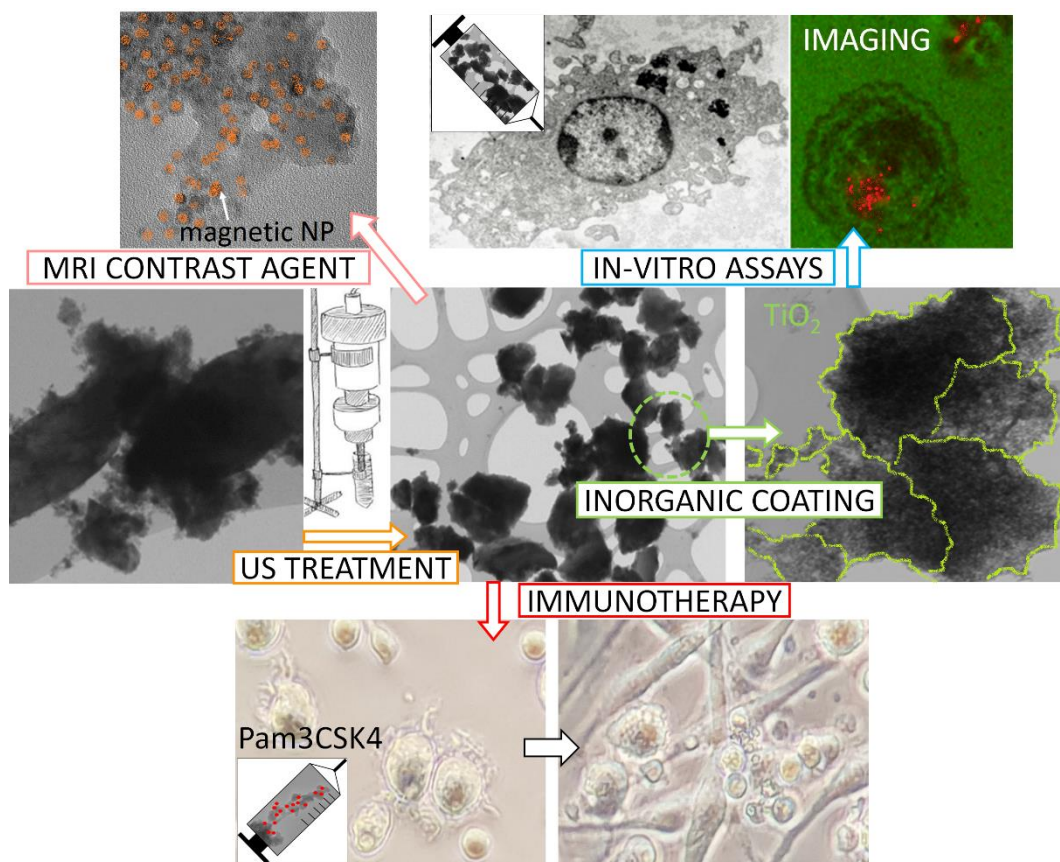


TABLE OF CONTENTS

Abstract.....	3
Sommario.....	4
Graphical abstract.....	5
Table of contents	6
Introduction.....	9
Chapter 1: Theranostics.....	15
1.1. Nanotechnology and nanomaterials	15
1.2. Nanotechnology applied to medicine.....	17
1.2.1. Diagnostic techniques.....	17
1.3. Theranostics	20
1.3.1. Nanomaterials for theranostic applications.....	22
Chapter 2: Porous silicon	28
2.1. Fabrication	28
2.2. Structural properties.....	31
2.3. Photoluminescence mechanisms.....	33
2.4. Surface chemistry.....	36
2.5. Main applications	39
2.6. Light-emitting pSi microparticles for theranostics	43
Chapter 3: Porous silicon microparticles fabrication and functionalization.....	47
3.1. Fabrication and functionalization procedures	47
3.2. Characterization techniques	49
3.3. Samples characterization.....	50
3.3.1. Surface properties	50
3.3.2. Optical analysis.....	52
3.3.3. Structural characterization	59
3.4. Conclusions.....	63
Chapter 4: Post-functionalization ultrasonic treatment	64
4.1. Experimental procedures and techniques.....	65
4.2. Optimization of the ultrasonic treatment.....	66
4.3. Optical properties.....	68
4.4. Structural and morphological characterization	70
4.5. Conclusions.....	75
Chapter 5: Inorganic coating of pSi microparticles.....	76
5.1. Atomic Layer Deposition of TiO ₂	78

5.2. TiO ₂ coated luminescent pSi microparticles	80
5.2.1. Structural, surface and chemical characterization	81
5.2.2. Optical properties.....	86
5.3. Conclusions.....	91
Chapter 6: In-vitro study: interaction with human immune cells	92
6.1. Immune system and dendritic cells	92
6.1.1. Interaction of DCs with nanoparticles	94
6.2. Porous silicon microparticles interaction with human DCs	96
6.3. Imaging of the human DCs and the microparticles.....	98
6.4. Cytotoxicity evaluation.....	103
6.5. Immune response evaluation.....	106
6.6. Conclusions.....	110
Chapter 7: Immune adjuvants delivery for immunotherapy: a preliminary study.....	112
7.1. Immunotherapy and vaccine adjuvants.....	112
7.1.1. Pam3CSK4	113
7.2. Porous silicon delivery of Pam3CSK4.....	114
7.2.1. Drug delivery and cell activation.....	116
7.2.2. Experimentals	117
7.3. Drug loading: fluorescence and confocal microscopy	118
7.4. Drug release in-vitro	120
7.5. Drug delivery and cell activation	121
7.5.1. Optical analysis.....	122
7.5.2. ELISA assays.....	123
7.6. Conclusions.....	124
Chapter 8: pSi infiltration with magnetic nanospheres	126
8.1. Magnetic resonance imaging	127
8.1.1. Magnetic principles and techniques.....	127
8.1.2. Magnetic nanoparticles.....	129
8.2. Infiltration of SPIONs within pSi microparticles.....	130
8.2.1. SPIONs functionalization	131
8.2.2. Functionalized SPIONs characterization	133
8.3. Magnetic porous silicon microparticles	138
8.3.1. Optical and structural characterization	138
8.3.2. Magnetic properties	145
8.4. Conclusions.....	149
Conclusions.....	151

References.....	Errore. Il segnalibro non è definito.
Appendix A1: Characterization techniques.....	167
Appendix A2: In-vitro cellular studies.....	171

INTRODUCTION

Nanoscience and nanotechnology are probably our present and future: nanostructures and nanomaterials are already present in our everyday life.

The ability of manipulating matter at the level of single atom and molecule, opened the way to researchers to synthesize or fabricate nanomaterials (i.e. material having at least one of its dimension measuring few to hundreds of nanometres), that have a wide range of applications due to their properties (strength, electrical resistivity/conductivity, and optical absorption) significantly different from the bulk, or the single-molecule, some of which appear and others are enhanced. As an example, carbon nanotubes combine the properties of diamond (strength) and graphite (electrical conductivity, but only in one direction). The role of nanoscience is to study and develop these materials in order to improve their unique properties. The role of nanotechnology is to engineer them, with potential applications in the fields of science, engineering, technology, and medicine. The idea at the basis of the nanotechnology research applied to medicine, is to use this knowledge to produce nanomaterials that interact with the organs aiming at diagnosing, treating and monitoring the cure of several diseases, thus helping the physicians in a quicker and more specific response to the disease, thus going towards a personalized medicine. In particular, the interest headed for such kind of materials is related to the possibility of encapsulating several medical agents in one single nanomaterial, thus obtaining a system to be used in theranostics. This word was invented as the union of therapy and diagnostic and relates to the possibility of having a unique multimodal tool that allows the diagnosis and treatment of disease at the same time in the same “place”, with consequent cure monitoring.

An example of nano-engineered material is porous silicon (pSi) which can be obtained by electrochemical etching of crystalline silicon wafers with a top-down approach. This produces a nanostructured material with high porosity, whose surface area depends on the fabrication parameters, and the appearance of photoluminescence (PL) at room temperature under UV excitation: PL emission wavelength depends on nanocrystal size and is tunable as a function of the fabrication parameters.

Moreover, pSi surface chemistry plays an important role in the wide range of applications, since its optical and structural properties can be finely tailored.

Among all the possible applications, for instance, electronics, optoelectronics, sensors, food and cosmetics, a lot of attention is directed towards biomedical applications. Usually, a nanomaterial must be properly functionalized after the synthesis or fabrication, to add specific properties (optical, magnetic, thermal, ability to load molecules) for its applicability in theranostics. Differently, porous silicon gained a lot of interest in this field because it is characterized by two intrinsic theranostic properties. Porosity and photoluminescence are indeed useful to exploit this material as a drug delivery carrier (therapy agent) while being monitored by imaging (diagnostic agent). Moreover, pSi is biocompatible, biodegradable and non-immunogenic. A sonication procedure allows producing mesoporous silicon microparticles with the right dimensions to interact with organs and cells of the human body. The topic of this thesis work is the utilization of opportunely functionalized pSi microparticles to obtain a reliable theranostics tool.

The main milestones, to be achieved for the employment of pSi microparticles as **traceable drug delivery carrier**, are:

- (i) Long-term photoluminescence *stability* for the storage of the microparticles in an organic solvent, as ethanol, which would avoid the development of bacteria in long-term conservation
- (ii) *Homogeneity* of the sample and *reduced average size*, since the dimension and the shape of the microparticles affect the cell uptake and behaviour
- (iii) Stabilization of the *photoluminescence in aqueous or biological media*, which otherwise would degrade due to the oxidation
- (iv) *Biocompatibility* and *immunogenicity* assessment: in-vitro test with human immune cells, for the reliability in biomedical applications
- (v) *Drug delivery test* in-vitro, to investigate the exploitability of porous silicon as a carrier
- (vi) *Addition of other properties* for a multi-modal approach, thus having several diagnostic and therapeutic applications, in a single tool

- (vii) *Targeting* toward specific organs/tissues, biodistribution evaluation (a pre-clinical test to study the target organs of such materials) and in-vivo tests.

When I began my PhD work, some of the milestones were already addressed, to reach and in some cases overcome the state of the art, and were reported in previous publications:

- (i) **surface functionalization** with COOH and NH₂ groups was employed to stabilize the pSi properties in ethanol for long-term conservation and degradation avoidance
- (ii) **biological stabilization** was investigated to preserve photoluminescence in biological media: covalent attachment of organic coating (PEG and chitosan) was used for this purpose
- (iii) the **interaction with human dendritic cells**, that are engaged in the immune response, was evaluated and neither toxic effect nor immunogenicity was observed for functionalized pSi microparticles
- (iv) preliminary **drug and release tests** in PBS were performed with Cbi (precursor of B12 vitamin) as drug test trial, that was efficiently loaded without losing its functionality and proved to be released with a slow-release, whose rate depends upon the microparticles surface charge.

Starting from these points,

IN THIS THESIS:

A brief overview to introduce the work is presented: the possibility to use nanotechnology in medicine (Chapter 1) and porous silicon with a focus on its biomedical application (Chapter 2) are necessary elements to explain some of the above milestones for the reliability of porous silicon in medicine.

The sample fabrication procedure is reported in Chapter 3; the characterization and a simple procedure to reduce the average size of microparticles are described in Chapter 4; the deposition of inorganic layers is investigated in Chapter 5 to stabilize the PL emission properties in aqueous media. Chapter 6 presents the result of cytotoxicity and immunogenicity of this material after incubation in human immune cells and preliminary results of immune vaccines delivery tests are shown in

Chapter 7. In Chapter 8 we focus on the possibility to add magnetic properties to pSi microparticles to increase its multimodal applications by MRI traceability.

The content of each chapter is summarized in the following:

In Chapter 1, we introduce the importance of nanotechnology to produce miniaturized materials that are actually used in our everyday life. The more interesting feature of nanomaterials, apart from their tiny dimension, is the variation of the properties with respect to the bulk material. It causes the appearance of new properties, such as photoluminescence in semiconductors, or the enhancement of preexistent properties, such as superconductivity in conductive materials. This opens the way to nanomaterials in a wide range of applications, that are briefly mentioned. We focus on medicine applications to produce a biocompatible multimodal system for real-time detection, treatment and monitoring of several diseases. The most investigated “nano-bio-materials” are reported with some applications and the reasons to use porous silicon in this field are indicated.

In Chapter 2, the discovery of porous silicon and the fabrication procedures are presented. The optical and structural properties are described, with a special focus on quantum confinement effect, to explain the pSi light emission at room temperature. The surface modifications to stabilize the properties of this material are reported too. The several applications found in the literature are briefly reviewed, with a focus on the possibility to obtain mesoporous microparticles for theranostic applications. The attempt to create a biocompatible carrier for biological molecules for in-situ diagnosis and therapy is described.

In Chapter 3, the experimental part of the thesis is introduced. The details of fabrication and functionalization procedures we used to produce porous silicon microparticles samples are reported. By using a carboxyl-functionalization, the photoluminescence is stabilized for several years in ethanol. A detailed characterization is performed to study and compare the samples' structural properties, i.e. average dimension, porosity, and the optical properties, i.e. steady-state and time-resolved photoluminescence.

In Chapter 4, the problem of inhomogeneity and broad size distribution of the samples related to the top-down fabrication approach and fragmentation by sonication is addressed. A simple, fast and cheap post-functionalization procedure to reduce the average size and disaggregate the microparticles reported. The procedure, based on ultrasounds, is effective without affecting the surface functionalization and the other properties.

→ Publication: E. Chistè, G. Ischia, M. Scarpa and N. Daldosso Mater. Res. Express **2019** 6 075006.

Chapter 5 concerns the pSi microparticles degradation and the relative PL quenching in aqueous media. After introducing the efficient protocol that was employed to cover the microparticles with an organic layer, PEG and chitosan, we identify the advantages and limitations. Thus, we reported an innovative method to deposit a titanium dioxide layer with tunable thickness by ALD, which allowed to stabilize the PL of the sample, without occluding the pores, due to the very thin deposition. Photoluminescence is monitored with time and structural properties are investigated.

→ Publication: E. Chistè, A. Ghafarinazari, M. Donini, V. Cremers, J. Dendooven, C. Detavernier, D. Benati, M. Scarpa, S. Dusi and N. Daldosso J. Mater. Chem. B **2018** 6 1815-1824.

In Chapter 6, we reported the study about the interaction of pSi microparticles with human immune cells that are responsible for the detection of pathogens, for the release of signalling molecules (called cytokines) and the relative inflammation response activation. In particular, the uptake by human dendritic cells (DCs) is examined: the internalization is investigated by optical and electron microscopy, the cell viability is evaluated by incubation of microparticles at different concentrations and the results for coated and uncoated microparticles are compared. We also evaluate the immunogenicity of the sample by detecting the number of released cytokines in the presence of the pSi microparticles, which reflects the

activity of the immune cells to activate the inflammation response. Finally, the photoluminescence of the sample inside the cell is investigated, in perspective of using pSi microparticles as imaging tracer.

→ Publication: E. Chistè, A. Ghafarinazari, M. Donini, V. Cremers, J. Dendoven, C. Detavernier, D. Benati, M. Scarpa, S. Dusi and N. Daldosso *J. Mater. Chem. B* **2018** 6 1815-1824.

In Chapter 7, some preliminary results concerning drug delivery and cell activation tests are reported. Here we present the development of previous promising results obtained with Cbi, employed as a drug test. Based on this, we choose a TRL agonist (Pam3CSK4), which is recognized by the toll-like receptors present on DCs membrane and is able to activate the immune response. The molecule loading on the pSi microparticles is evaluated by confocal microscopy (the superposition of the signal coming from the microparticles and from Pam3CSK4 labelled with a fluorophore). The effect on the cell activation is evaluated by quantification of the released cytokines, focusing on the possible synergic effect of the TLR agonist carried by pSi microparticles, with respect to the molecule and the microparticles, alone.

Finally, Chapter 8 reports an innovative method to add magnetic properties to the microparticles, with the scope of creating a multimodal theranostics system, traceable also by MRI. We used a simple, fast and cheap chemical procedure to infiltrate SPIONs (superparamagnetic iron oxide nanoparticles) inside the silicon pores interacting electrostatically with the COOH groups at the surface. Elemental composition, structural and magnetic properties of the samples are investigated to evaluate the reliability of the material as an MRI contrast agent.

→ E. Chistè, G. Ischia, M. Gerosa, P. Marzola, M. Scarpa and N. Daldosso “Porous Si microparticles infiltrated with magnetic nanospheres for theranostics” *Nanomaterials* **2020** 10 463.

In the Conclusions, the main obtained results and the future perspective are summarized.

CHAPTER 1

THERANOSTICS

In this introductory chapter, a brief overview is presented, to explain the reason why, recently, medicine is developing a growing interest in nanotechnology and nanomaterials and what is theranostics. The most commonly exploited nanomaterials are presented with the main benefits and limitations, and the advantages of using porous silicon in theranostics are pointed out.

1.1. Nanotechnology and nanomaterials

Nanotechnology refers to the manipulation of matter at the atomic and molecular scale and attracted a lot of attention for a broad range of scientific and industrial applications.¹ It involves the study of nanometric structures, i.e. the nanomaterials. They can be produced with two different approaches: top-down (starting from bigger materials) or bottom-up (starting from atoms or molecules) and they are characterized by at least one dimension shorter than 100 nm. The growing interest gained by nanomaterials, is due to the modification of a large number of properties with respect to the bulk material, passing from micro to nano-structures: the increase of the surface/volume ratio and the appearance of quantum effects due to size reduction, among all. This leads to an alteration of mechanical, thermal, optical and catalytic properties, such as the appearance of photoluminescence in semiconductors² and supermagnetism in small magnetic nanoparticles, increasing mechanical strength and plasticity,³ modification of melting point,⁴ wettability, catalytic activity,⁵ electrical⁶ and thermal conductivity.

A lot of nanoparticles are present in our everyday life since nanotechnology is able to increase strength, lightness, durability, electrical conductivity, and reactivity of materials. In fact, different fields find applications in this new technology: electron-

ics, transportations, energy and environment, space exploration, health and medicine, depending on the shape of the nanomaterials (nanoparticles, nanorods, nanotubes, nanogels).

In textile applications, the nanomaterials are very interesting due to their ability to improve the fabric properties, such as water resistivity and as an example, silver nanoparticles can reduce the bacteria growth without effect on the weight.⁷ Nanofilms are deposited on display or glasses to be water, scratch, UV or IR resistant, antireflective, self-cleaning and electrical conductive. Cellulose-base nanomaterials, such as film and gels, have proved to have interesting properties in several fields, for instance, healthcare, packaging, energy, thermal insulation and electronics.⁸ Nanoparticles, due to the high surface area, have strong catalytic activity in chemical reactions, thus reducing the necessary amount of material normally used for this goal. Furthermore, they have applications as environmental sensors and filters, such as air purifiers and antibacterial cleansers, and in paints to obtain self-cleanser walls or to increase thermal insulation. They are also added to sunscreens to protect from UV radiation.⁹ Moreover, they greatly contributed to the electronics and computer improvements, to create smaller and lighter systems, but increasing the performances: transistors size pass from hundreds of nm at the beginning, to few nm nowadays. Semiconductors, graphene and cellulose-based nano-membranes allow producing flexible electronics for medical and aerospace applications or photovoltaics.¹⁰ Also the field of civil engineering uses nanomaterials, such nano-sensor, and nano-devices, to monitor the stability of building, bridges and tunnels. Researchers are also studying the possible applications of nanotechnology for environmental friendly application, to provide clean and renewable energy, but without toxic effect to the environment, for example nanoparticles are embedded in solar cells for a more efficient light conversion, or to detect contaminants and impurities of water, which can become drinkable by desalination through MoS₂ nanoporous membranes.¹¹ Medicine aims at producing precise solutions for disease prevention, diagnosis, and personalized treatment by means of nanotechnology. It is interested also the possibility of single-molecule detection with minimal sample preparation and instrumentation. The use of nanomaterials in medicine, for drug

delivery, regenerative medicine and imaging is better described in the next paragraphs.

1.2. Nanotechnology applied to medicine

Nanomedicine can be briefly described as the application of nanotechnology to medicine, but there is no unique definition.¹² For the ESF (European Science Foundation) it is “*the science and technology of diagnosing, treating, and preventing disease and traumatic injury, of relieving pain, and of preserving and improving human health, using molecular tools and molecular knowledge of the human body*”. Two classes of agents, whose relative applications are shown in Figure 1.1, are used in medicine:

- (i) **therapeutic agents:** drugs and molecules to be delivered to a specific target, and released in a controlled way or under a stimulus¹³
- (ii) **diagnostics agents:** radionuclides, magnetic and fluorescent materials, used as contrast agents for imaging techniques.

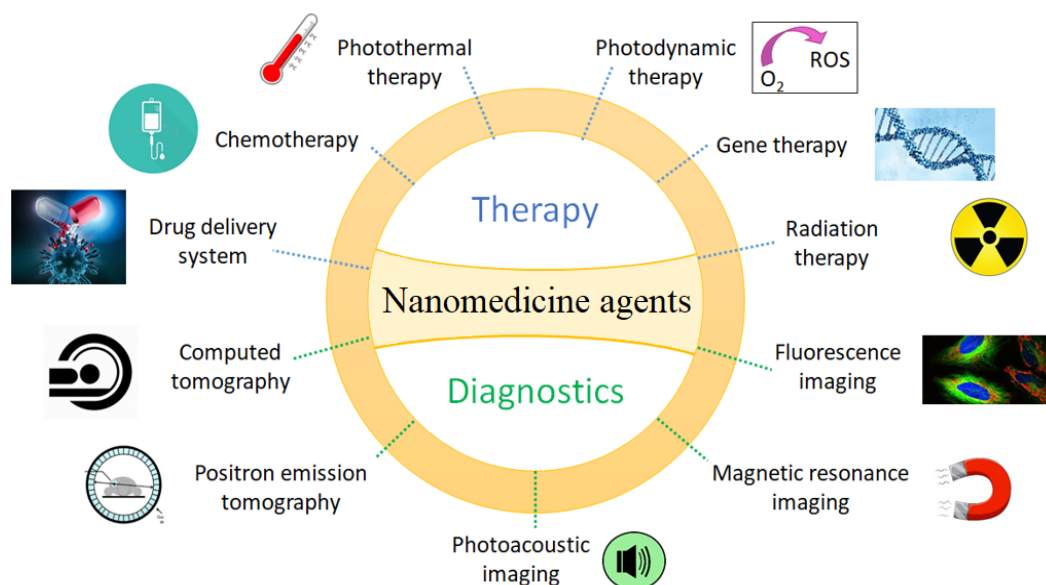


Figure 1.1 Examples of medicine agents' application for therapy and diagnostics.

1.2.1. Diagnostic techniques

The scheme in Figure 1.2¹⁴ resumes the main diagnostic techniques used in medicine, with the relative advantages and limitations: PET (positron emission tomography) and SPECT (single-photon emission computed tomography), CT (computed

tomography), MRI (magnetic resonance imaging), OI (optical imaging) and US (ultrasounds) imaging.¹⁴

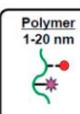
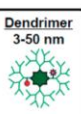


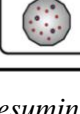
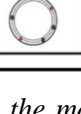
IMAGING	NANOMEDICINES	APPLICATIONS	ADVANTAGES	LIMITATIONS
PET SPECT	<div style="display: flex; flex-wrap: wrap;"> <div style="width: 50%;"> <p>Polymer 1-20 nm</p>  </div> <div style="width: 50%;"> <p>Dendrimer 3-50 nm</p>  </div> <div style="width: 50%;"> <p>Micelle 20-80 nm</p>  </div> <div style="width: 50%;"> <p>Liposome 80-150 nm</p>  </div> <div style="width: 50%;"> <p>Nanoparticle 5-250 nm</p>  </div> <div style="width: 50%;"> <p>Microbubble 800-3000 nm</p>  </div> </div>	<ul style="list-style-type: none"> • Drug targeting • Biodistribution • Blood pool imaging 	<ul style="list-style-type: none"> • High sensitivity • Quantitative results • Unlimited penetration 	<ul style="list-style-type: none"> • Limited spatial resolution • No anatomical information • Radioactive probes
CT		<ul style="list-style-type: none"> • Anatomical information • Hybrid imaging • Perfusion monitoring 	<ul style="list-style-type: none"> • High spatial resolution • Dynamic imaging • Quantitative results 	<ul style="list-style-type: none"> • Low contrast agent sensitivity • Poor soft tissue contrast • Radiation exposure
MRI		<ul style="list-style-type: none"> • Drug release • Drug efficacy • Cell tracking 	<ul style="list-style-type: none"> • High spatial resolution • High soft tissue contrast • High versatility 	<ul style="list-style-type: none"> • Low throughput • Low contrast agent sensitivity • Difficult quantification
OI		<ul style="list-style-type: none"> • Drug targeting • Hybrid imaging • Nucleic acid delivery 	<ul style="list-style-type: none"> • High throughput • High sensitivity • High probe versatility 	<ul style="list-style-type: none"> • Poor penetration depth • No anatomical information • Difficult quantification
US		<ul style="list-style-type: none"> • Drug targeting • Perfusion monitoring • Sonoporation 	<ul style="list-style-type: none"> • High sensitivity • High throughput • Dynamic imaging 	<ul style="list-style-type: none"> • Low probe versatility • High user dependency • No whole-body imaging

Figure 1.2 Scheme resuming the main diagnostic techniques used in medicine, with the relative advantages and limitations.¹⁴

PET and *SPECT* involve the use of radioactive probes: the positrons emitted from the radionuclide annihilate with surrounding electron thus generating two photons that are simultaneously detected in the case of *PET* and singularly in *SPECT*. They have high penetration depth and sensitivity, but low resolution and no anatomical information. *CT* is based on X-ray imaging and produces high-resolution anatomical images, due to the high sensitivity towards materials with different electron densities. In *MRI*, the image is elaborated from the response of hydrogen nuclei to the application of RF signals and the sequent realignment towards the external magnetic field direction when the RF is off.¹⁵ Contrast agents, for instance, gadolinium or iron oxide nanoparticles, are used to increase the resolution of the image. *Optical imaging*, by detecting the fluorescence emission, allows tracking the material in-vitro and in-vivo. It is not so expensive as other techniques and it does not expose the tissue to ionizing radiation, but it has low depth penetration and then, it is more difficult to be used in patients. For tissues investigation or in-vivo experiments on small animals, it is very effective. *US imaging* is based on the variability of US waves propagation and backscattering in different tissues. Recently, it has been also shown that US can be used to induce the release of drugs from some carriers. *Photoacoustic* (optoacoustic) imaging (PAI) is based on the photoacoustic effect. The excitation of biological tissue with NIR laser pulses causes the formation of sound waves that are produced by the light absorption and generation of heat. This causes

a thermoelastic expansion of the tissue components and thus pressure transient signals, which are analysed and transformed into an image by ultrasonic transducers. This technique is sensitive to the concentration of haemoglobin or melanin, but also of contrast agents, such as indocyanine green, employed to enhance the photoacoustic effect and to better visualize elements such as blood vessels.

1.2.2 Main therapies

Among the therapies, drug delivery systems (DDS), photothermal therapy (PTT) and photodynamic therapy (PDT) are widely used.

Drug delivery is one of the most exploited therapies since it can be applied to any disease, that needs treatment with a pharmaceutical compound (drug). It refers to the mechanism of transportation of a therapeutic substance into the body and it was introduced for the need of improving and prolonging the drug efficacy, but avoiding its degradation, or loss, and minimizing the side effects. Several routes of administration can be employed, depending on the application: enteral, parenteral (via injections), inhalation, topical and oral. The use of carriers (matrices) is involved to load, protect and transport molecules to be released at a controlled rate and to a specific target. The targeting can be passive (direct local application or due to the higher permeability of tumour tissues) or active (if a specific ligand is present on the carrier surface). It is very attractive because it can transport the drugs to sites difficult to be reached by the drug alone.

Three steps have to be assessed to evaluate the exploitability of material as DDS, after the choice of the proper drug:

- (i) drug chemical stability: it is important to avoid the degradation of the molecule after the encapsulation in the carrier
- (ii) evaluation of the loading capacity: it is determined by dissolving the carrier and quantifying the drug content. As a function of the type of carrier, several loading methods were implemented, such as adsorption, covalent bonding, encapsulation, or trapping by oxidation
- (iii) release time curve in-vitro: it is determined by measuring the quantity of released drug into a buffer medium. In the SS (Sample and Separate) method, the loaded carrier is introduced into the media and the supernatant

is sampled at set times (by filtration or centrifugation), to measure the quantity of the present drug. In the CF (Continuous Flow) method, the loaded carrier is immobilized and the medium flows and transport the drug, that is released: the buffer is collected at set times to monitor the drug release. In DM (Dialysis Method), the loaded carrier is introduced into a dialysis filter, through which only the drug can diffuse. The membrane is placed in a buffer medium, which is sampled at set times to measure the release.

PDT (photodynamic therapy) is a minimally invasive therapy, to treat cancer or other pathologies. It is composed of three steps: (i) a photosensitizer is injected and accumulated inside the cancer tissue, where it remains for a longer time respect to healthy tissue, (ii) it is illuminated to be activated, (iii) the oxygen inside the tissue is photosensitized to produce SO (singlet oxygen) and ROS (reactive oxygen species), which transfer the excess energy to the surrounding molecules and are very cytotoxic.

PTT (photothermal therapy) is based on overheating of cancer tissues, called hyperthermia, induced by light at temperatures higher than 40-41 °C (for T higher than 46 °C it is called thermoablation) and cause direct and specific cytotoxicity towards cancer cells. Nanomaterials are usually exploited, because, due to the EPR effect, they preferentially accumulate inside the tumours. Then, they can be excited by NIR light and they release heat (vibrational energy) to kill the cells. The possibility to excite the photothermal agent by long-wavelength light (less energetic) allows reducing the damages to healthy tissues.

Concerning the advantages and limitation of any single diagnostic and therapy modality, their combination could be very interesting to go beyond the limitations of each technique.¹⁴

1.3. Theranostics

One of the nanotechnology roles in medicine is to establish nanosized carriers able to improve the diagnosis ability, to fight against the disease at an earlier and more treatable phase. For this reason, the nanostructured materials are engineered to adsorb, trap, bind or encapsulate the diagnostic and therapy tools. Furthermore, by

conjugate a targeting ligand or a biomarker, it is possible to deliver the material to the desired tissue-organ, hence producing fewer side effects and more specificity. The need to produce a platform for specific and personalized medicine comes from the fact that the treatment efficacy varies from patient to patient. Thus, the goal is to tailor a personalized targeted medicine tool, taking into account the individual variability.^{15,16} With this intent, the concept of theranostics was created by John Funkhouser in 1998, as the union of the words “therapy” and “diagnostics”.^{17,18} Then, nanotheranostics was developed to integrate the monofunctional nanomedicine and the multimodal theranostics in a single nanocarrier. The role of nanoscience and nanotechnology is, therefore to combine the two functionalities in a single multi-functional system, with the purpose of diagnosing a disease, treat it and monitor the response of the therapy and its efficacy, specifically for any individual patient.

A wide range of application were evaluated to move towards personalized medicine: the most investigated are cancer therapy,^{19,20} neurodegenerative disorders, such as Alzheimer’s and Parkinson’s diseases, and in general pathologies relative to the brain, that are difficult to be treated due to the limited ability of drugs to cross the BBB (blood-brain barrier),²¹ but also cardiovascular diseases,²² CNS (central nervous system) and immune diseases.²³

The main steps about the nanotheranostics approach are shown in Figure 1.3, for cancer as a representative disease: the multimodal medication targeting allows to improve both the imaging diagnosis ability, the localized therapy and the effectiveness of the treatment, with reduced side effects.

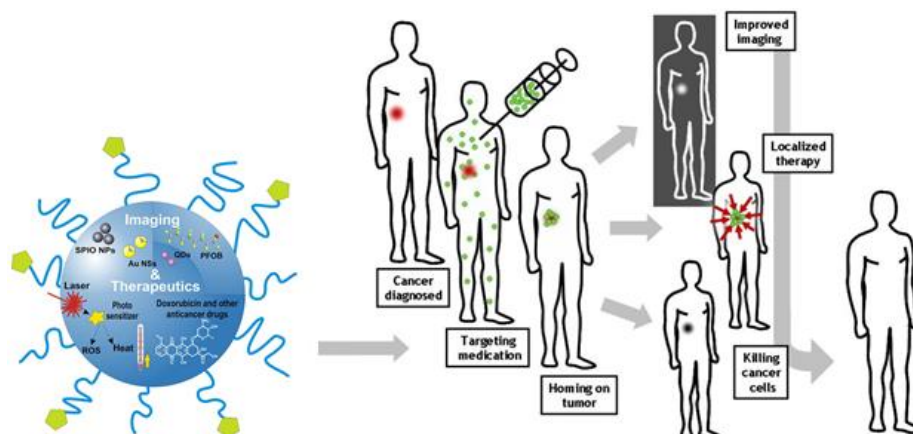


Figure 1.3 Steps involved in nanotheranostics: targeting, imaging and therapy.²⁴

1.3.1. Nanomaterials for theranostic applications

The use of nanomaterials in medicine has several positive aspects:

- (i) the high surface-to-volume ratio implies a higher area available for molecules or ligand attachment. For porous materials, it allows a high amount of loaded drug, which is protected from being dissolved in blood circulation
- (ii) the extravasation in large quantity from the leaky vessels of tumour tissues, where they remain due to the poor lymphatic drainage. This is known as EPR (enhanced permeability and retention) effect
- (iii) the possibility to functionalize it for a better stabilization or for targeting, which is fundamental to avoid the toxicity related to the drug accumulation in unwanted tissues, such as spleen and liver, typically
- (iv) the combination of diagnostics and therapeutics to monitor the efficacy of the treatment.

The main issues to be solved in this field are the material-related toxicity and the effect on the environment. In particular, it has to be considered that there is a difference between the toxicity related to the bulk material and the nanostructured form since the high surface area of the NPs imply higher reactivity. Thus, size, shape and surface chemistry have to be carefully investigated to evaluate the biocompatibility of the material, both concerning health and environment.

The nanomaterials used in medicine are inorganic or inorganic.^{25,26} Among the organic materials there are polymeric nanoparticles, such as micelle, nanospheres, hydrogel nanoparticles, nanocapsules and dendrimers, and lipidic nanomaterials (liposomes, that are already commercialized).

The inorganic nanoparticles are nanocrystals, metallic, magnetic and ceramic materials.

Figure 1.4 represents the nanomaterials used for nanomedicine, which are better described in the following. The organic nanomaterials, i.e. polymeric and lipid nanoparticles, are the most used materials also in clinics, and in particular as drug delivery carriers and regenerative medicine scaffolds, but inorganic nanomaterials are gaining more and more interest nowadays.²⁷

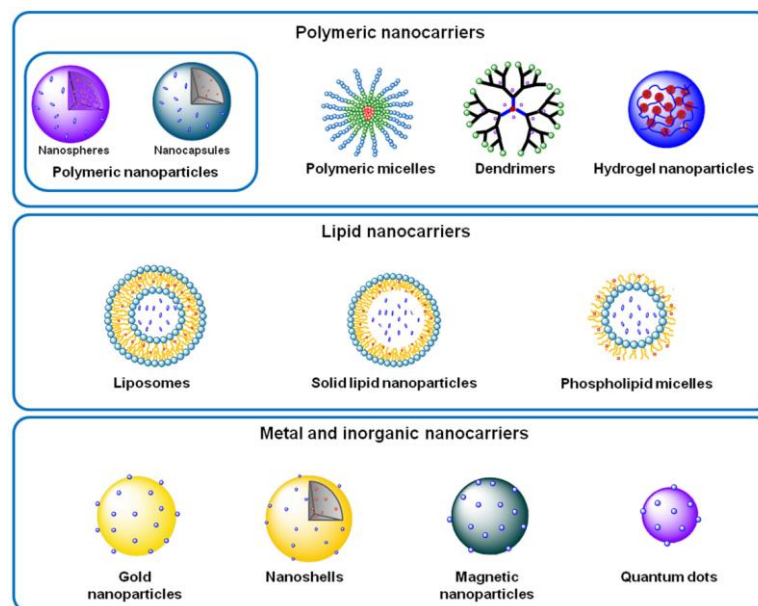


Figure 1.4 Examples of nanomaterials used in nanomedicine and classified by polymeric, lipid or inorganic materials.²⁸

Polymeric NPs are spherical structures composed of interconnected polymers, that can form a compact nanoparticle or a void nanoshell. The polymer can be natural or synthetic and the shape of the nanocarriers varies from nanospheres to nanosponges, or nanofibers. They can encapsulate hydrophobic molecules inside the NPs core structure, whose hydrophobicity depends on the used copolymers. Furthermore, the exposure of ligands on their surface is useful for controlled targeted drug delivery²⁹ and for example for wound healing.³⁰ PEG is employed in large quantity, due to the absence of immunogenicity and the increased time circulation in blood. It can be used as a core material or coating to improve the stability of bound molecules or nanoparticles, such as SPIONs to be delivered to a specific organ/tissue.³¹ For example, nanovesicles were produced with a polyglutamate core containing SPIONs, coated with PEG and coupled to FA (folic acid) for targeted delivery of DOX (doxorubicin, the medical model of anticancer drugs), which was loaded with a pH-sensitive ligand and found to be an improved contrast agent respect to the commercial SPION Feridex.³² Theranostic polymeric NPs were produced by coating a polymeric core with PEG and coupling it to the PDT sensitizer indocyanine, thus obtaining a theranostics agent with reduced target cancer cell growth by PDT effect.³³

Dendrimers are branched globular macromolecules composed of central hydrophobic monomers structure and functionalized peripheral branched hydrophilic groups. Their force is the low viscosity and possibility to be functionalized in a large variety of ways, thus being a very versatile material. Their controlled depolymerization is interesting for drug delivery applications³⁴ and they are also used to decorate other nanoparticles, such gold NPs optimized for biosensing applications.³⁵

Lipid nanocarriers, for example, liposomes are vesicles produced spontaneously when amphiphilic molecules are dispersed in water. These macromolecules are composed of a hydrophilic and a hydrophobic part, thus tending autonomously to aggregate and expose only the hydrophilic part towards the aqueous media. Furthermore, it is easy to load hydrophobic drugs inside the NPs and a surface PEGylation is useful to stabilize the circulation in blood.³⁶ The drug release is modulated by light, ultrasounds, enzymes interaction or magnetism.

Mesoporous silica NPs (MSNPs) porosity, shape and size can be fine-tuned by varying the synthesis procedure and chemical groups can be incorporated during the synthesis, due to the silanols groups present on the surface.³⁷ They are able to include a lot of molecules inside the pores and they were recently approved for human clinical trials.³⁸ On the contrary, it seems that a coating is needed, otherwise, they would be haemolytic, i.e. damaging the red blood cells.³⁹ It was proved that a photosensitizer can be loaded and its PTT action is enhanced by the MSNPs;³⁷ or magnetic nanoparticles can be loaded inside the pores for MRI tracking.⁴⁰ It is possible that the NPs agglomerate and thus a coating is necessary.

Iron oxide nanoparticles (IONPs), such as magnetite, maghemite and hematite, have strong magnetic properties and thus are very promising for diagnostics (employed as contrast agents for MRI), hyperthermia treatment, caused by entrapped NPs, magnetic separation, drug delivery and biosensors. They can be synthesized with several approaches, such as co-precipitation, sol-gel, ultrasonic, microwave and electrochemical methods.⁴¹ A surface functionalization is needed to stabilize their properties, to avoid the aggregation, and specific molecules can be attached for targeted delivery.⁴² For example, polyacrylic acid was employed to co-encapsulate IONPs, a NIR probe and an anticancer drugs-for MR and fluorescence

imaging; the addition of folic acid (FA) allows to target cancer cells overexpressing the relative receptor.⁴³ A pH-sensitive drug delivery system for cancer therapy was performed by coating the SPIONs with a biodegradable polymer, bound to amine groups, and other functional groups, as FA⁴⁴ to guide the drug toward the desired tissue and release the load according to the pH variation (it is known that cancer tissues are characterized by acidic pH).

Gold nanomaterials can be produced with different shapes, thus having different optical and photothermal properties: nanospheres, nanocages, nanostars, nanorods. The spheres adsorb in the visible and the others in the NIR (near-infrared) region, thus being useful for PTT (photothermal therapy),⁴⁵ PAI (photoacoustic imaging)⁴⁶ or as sensors. They are not fluorescent but are used as contrast agents in computed tomography (CT), due to high X-ray absorption coefficient, and as radiotherapy (RT) sensitizer. The functionalization of the surface with amine or thiols, limit the possibility of drug attachment, but to solve this issue, some studies on release by photothermal energy were performed, finding that, when exposed to heat, the AuNPs release the payload.⁴⁷

Quantum dots (QDs) are semiconductors nanocrystals, whose photoluminescence is tuneable as a function of size (few nm) and composition. Among them, the most investigated are CdSe, InAs, ZnSe. The nanometric dimension is interesting for diagnosis of micrometastasis with good imaging resolution. The main issue is their toxicity, related to the heavy metal they are composed of, which may limit their use, and could be solved by coating the QD core with other organic (encapsulation in micelles)⁴⁸ or inorganic materials,⁴⁹ or with thiolated ligands conjugated to their surface.

Carbon nanotubes (CNTs) are single or multiple concentric cylinders of graphene with nm diameters and hundreds of nm – few μm lengths. Due to their absorption in the NIR region, they can be applied for imaging or PTT (photothermal therapy)⁵⁰ and photothermal ablation (PTA) to ablate cancers cells.⁵¹ It is difficult to evaluate and generalize the toxicity, due to their shape, thus a polymer functionalization is usually necessary. They are able to stimulate the neuronal growth and to increase the electrical signal in neural and cardiac cells.⁵²

The main advantages and limitations of nanomaterials above described are summarized in Table 1.1.

Table 1.1. Main advantages and limitations to the use of nanomaterials in nanomedicine.

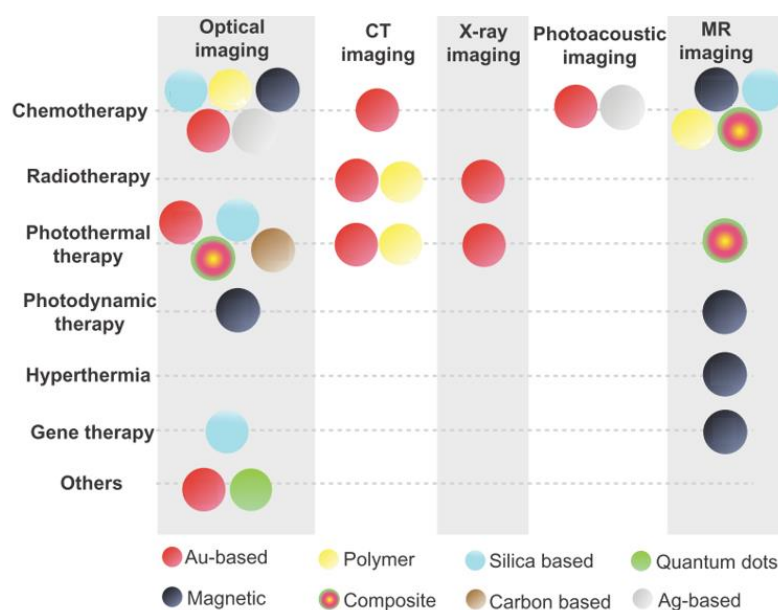
Nanomaterial	Advantages	Limitations
<i>Polymeric NPs</i>	<ul style="list-style-type: none"> - self-assembled colloidal NPs - micelles EPR higher than free drugs in tumours - biocompatible 	<ul style="list-style-type: none"> - limited stability in aqueous media - immunogenic - partial carrier degradation
<i>Lipid NPs</i>	<ul style="list-style-type: none"> - self-assembled vesicles with hydrophobic core → hydrophobic drug loading and hydrophilic molecules external binding - biocompatible 	<ul style="list-style-type: none"> - careful preparation is needed to have reproducible properties and efficiencies - cationic lipids cause toxicity
<i>Dendrimers</i>	<ul style="list-style-type: none"> - Very small: dimension controlled at a molecular level 	<ul style="list-style-type: none"> - conjugation of a low amount of drug - dose-dependent haemolysis
<i>SPIONs</i>	<ul style="list-style-type: none"> - Magnetic properties → CAs in MRI and hyperthermia - Biocompatible 	<ul style="list-style-type: none"> - poor colloidal stability - a coating could reduce the sensitivity to the magnetic field
<i>Porous SiO₂ NPs</i>	<ul style="list-style-type: none"> - a lot of space for drug loading - tuneable size and shape - incorporation of several functional groups is possible 	<ul style="list-style-type: none"> - uncoated are haemolytic - agglomeration
<i>QDs</i>	<ul style="list-style-type: none"> - very small and PL tuneable with dimension 	<ul style="list-style-type: none"> - toxicity related (heavy metals)
<i>Gold NPs</i>	<ul style="list-style-type: none"> - fabrication in several shapes for different applications - NIR absorption → PTT and PAI 	<ul style="list-style-type: none"> - only amine and thiol functionalization → limitation on drug loading
<i>CNTs</i>	<ul style="list-style-type: none"> - NIR absorption → PTT and imaging - increase the electric signal in neural and cardiac cells 	<ul style="list-style-type: none"> - Difficult to evaluate compatibility → functionalization - lung damage if inhaled

Very few of the previously reported nanomaterials are intrinsically multimodal systems, meaning that they have either therapeutic or imaging functionality, and they have to be completed by other molecules or materials to be exploitable in theranostics. A lot of composite materials are studied to produce a multimodal theranostics agent. For example, the covering of Au nanoparticles with SPIONs produces SP nanoroses that are very effective for PTT and it was proven that a dextran coating further improves the uptake by immune cells.⁵³ SPION cores were covered by an amorphous silica shell and coated with a gold layer. Due to the high

absorption in the NIR region, this material can be used for PTA. The photo-ablation treatment is modulated by varying the SPIONs concentration, time and power of treatment.⁵⁴ The system was further modified⁵⁵ by using mesoporous instead of amorphous silica, linked to Au nanorods, to load a chemotherapeutic (DOX) for the coupling of PTT, MRI and chemotherapy.

Table 1.2⁵⁶ shows the application of the different nanomaterials in diagnostic and therapeutic applications.

Table 1.2. Application of the different nanomaterials in diagnostics and therapy.



From the table above, we can deduce that inorganic materials are the most versatile since most of them are used for several applications at the same time. In fact, gold NPs can be traced by PAI and have photothermal effect; SPIONs can be traced by MRI and are used for hyperthermia treatment; mesoporous silica can be used for drug delivery and PTT. On the contrary, organic nanocarriers are usually employed only as drug delivery systems and are exploitable for their biocompatibility and biodegradability.

In the huge field of research of nanomaterials for medicine, during my PhD, I worked on porous silicon microparticles as a theranostic multimodal system. The interest in this material grows from its peculiar and intrinsic properties: photoluminescence, porosity, and biocompatibility, which make it suitable for drug delivery and traceable by fluorescence imaging. Properties, fabrication methods and applications are described and discussed in Chapter 2.

CHAPTER 2

POROUS SILICON

Porous silicon (pSi) is a sponge-like material of interconnected silicon wires that was accidentally produced for the first time in 1956 at the Bell Laboratories by the Uhlirs.⁵⁷ While performing some experiments on the electrochemical polishing of crystalline Si wafers in HF solutions, they observed that, under certain conditions, a dark layer was formed on the wafer surface, later known as porous silicon. Several years later, in 1990, Leigh Canham noticed that this material was characterized by intense photoluminescence at room temperature.⁵⁸ Due to this great discovery, the number of publications on porous silicon increased from 10 in 1990 to 1200 per year nowadays.⁵⁹

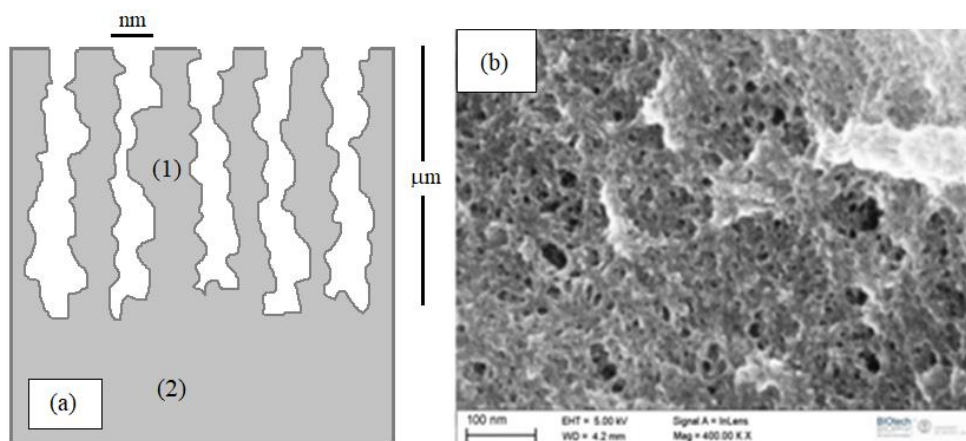


Figure 2.1 Porous silicon. Panel a: schematic picture of porous silicon (1) on a bulk silicon layer (2). Panel b: Porous silicon real surface, showing the sponge-like structure.⁶⁰

2.1. Fabrication

Two approaches are used to fabricate porous silicon: the bottom-up approach, based on a mechanical-physical process (Si clusters are put together and some voids are purposely introduced) and the top-down one, based on a chemical-physical process (pores are created by porosification of a crystalline structure).

More than 30 procedures have been proposed to obtain porous silicon and are based on chemical, thermal, irradiation, deposition and mechanical techniques. The porosification can be obtained by electrochemical etching (anodization etching is the most common), lithographic, and vapour etching (starting from Si wafer), or by metal-assisted chemical (MACE), stain and galvanic etching (starting both from Si-wafer and Si powder). Differently from these techniques, which allows obtaining “open porosity” structures and thus accessible from the outside, melt gasification and milling/sintering are used to obtain “closed” porosity.⁶¹

Hereafter, I briefly summarize the most used procedures to produce porous silicon.

There are three classes of etching: chemical, electrochemical and stain etching:

- (i) **chemical etching** does not involve free charge exchange, but chemical species attack the silicon wafer surface
- (ii) **electrochemical etching** involves the exchange of free carriers to overcome the kinetic potential of the reaction. With the anodization etching, an external bias is needed to create holes, while with photo-etching, a photon excitation is used for this purpose (this is mostly employed for the porosification of n-type Si wafers)
- (iii) **stain etching** is a spontaneous reaction, where an oxidizing agent, in solution phase, directly removes the electron from the valence band. Differently, galvanic etching needs the presence of a metal (Al or Pt) layer, where the oxidizing agent is reduced to catalyse the hole injection. A type of galvanic etching is MACE (metal-assisted chemical etching), which needs metal nanoparticles or nanostructured metals as electro-catalyst to produce pores or nanowires.

On the other hand, porous silicon can be produced starting from porous silica, silica nanoparticles or silicon-based molecules, by means of thermal, mechanical or chemical conversion methods:

- (i) **chemical conversion** process is a magnesiothermic reaction, where solid or porous silica is exposed to magnesium vapour and heated. The produced

silicon/magnesium oxide nanocomposite is transformed into porous silicon by acid extraction

- (ii) **mechanical synthesis** of porous silicon is based on milling (top-down approach), pressing (bottom-up approach) and sintering. The combination of these techniques allows tuning the resultant porosity over a large scale.

To produce the microparticles that are reported in this thesis, I exploited the most common procedure, which is the anodization etching in HF-based solution; the fabrication procedure and the parameters that I used to obtain pSi microparticles are described in Chapter 3.

During the etching reaction in the electrochemical cell, the Si surface is partially dissolved. Figure 2.2 shows the mechanism of silicon dissolution in acid solution (i.e. HF hydrofluoric acid), where holes injection is necessary.

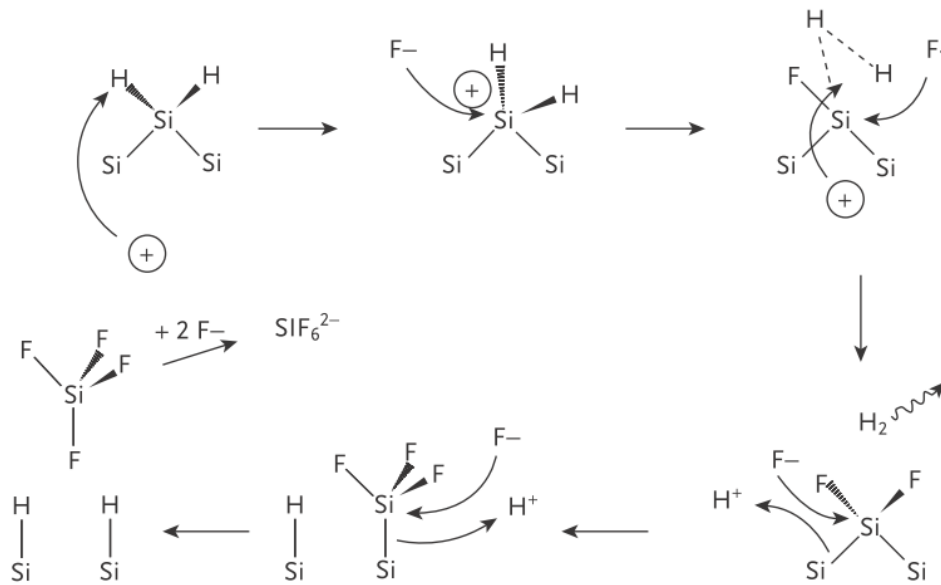


Figure 2.2 Electrochemical corrosion and porosification mechanism on the crystalline silicon wafer surface in HF solution.⁶²

First, the F atoms substitute the hydrogen atoms present on the surface (and H₂ is released), but when a Si atom binds a fluorine atom, it is more easily attacked by other F and it is immediately removed from the surface, which is hydrogen passivated. Hence, SiF₄ molecules are released in solution and the Si surface is passivated by hydrogen atoms. Therefore, the as-etched silicon has Si-H, Si-H₂ and Si-H₃, but almost no O and F atoms on its surface. This procedure of pore formation begins in

correspondence of Si surface defects, then the wafer start corroding and the pores create inside the bulk silicon, as it is schematized in Figure 2.1 (a). The pore dimension and the structure depend mainly on current density, but also on temperature, HF concentration, anodization time, wafer resistivity and doping type. Porous silicon can be produced starting from p-doped (B - boron) or n-doped (Sb - antimony) silicon crystalline wafers. The p-type is more stable to oxidation, even if less surface area can be produced.⁶³

The solution in the electrochemical cell is composed of a mixture of hydrofluoric acid and ethanol: this is necessary to increase the cleared surface wettability, to better allow the HF to enter the pores, to help to remove the hydrogens generated during the reaction and increase the homogeneity of the porous layer.⁶⁴

2.2. Structural properties

The above-mentioned fabrication techniques allow obtaining porous structures with different dimensions (Figure 2.3), depending on the substrate type and the fabrication procedure. For this reason, it is useful to classify porous silicon (pSi) depending on the pore characteristic sizes, which are pore dimension and inter-distance. According to the IUPAC (International Union of Pure and Applied Chemistry) guidelines, there are microporous, mesoporous and macroporous silicon structures:

- **microporous silicon** has pores with an average dimension lower than 2 nm (panel a). It is produced at high HF concentration
- **mesoporous silicon**, with an average pore dimension between few nm and 50 nm (panel b). Usually, the pore size obtained by electrochemical etching has a broad distribution between 3 and 20 nm, till 50 nm in some cases.⁶⁵ The morphology depends on substrate type and on fabrication conditions
- **macroporous silicon**, with more than 50 nm pore size (panel c). The morphology depends on substrate type and on fabrication conditions. When produced by electrochemical etching, the pores grow in the crystallographic directions, for n-type wafer, while in the current lines for the p-type.

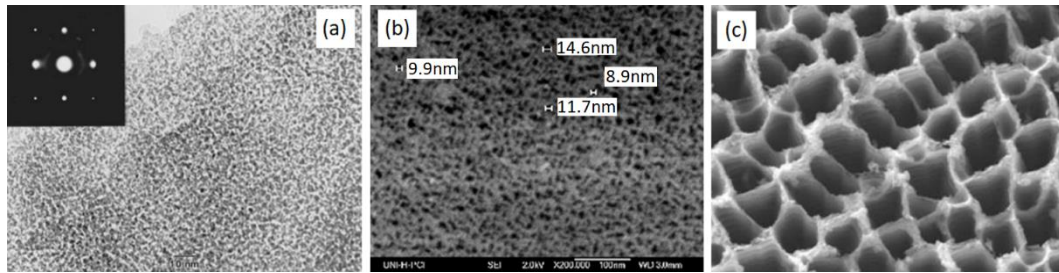


Figure 2.3 Examples of microporous (a), mesoporous (b) and macroporous (c) structures of porous silicon layers.⁶⁶

As previously said, the nanostructure features depend on the fabrication conditions: the higher is the HF concentration, the smaller are the produced pores; the tunability of the porosity is also dependent on current density and time of treatment. In particular, porosity increases with current density, etching time and n-type wafer doping; it decreases with HF concentration and p-type wafer doping.

For anodization etching fabrication, the structural properties are mainly dependent on the anodization conditions and wafer resistivity. Typical values of porous layer thickness are of the order of μm and it increases, as the anodization time or the current density does. The surface area of this material can be as high as $800\text{ m}^2/\text{cm}^3$, with a porosity that can vary from 20 to 95%.⁶⁷ For p⁺-type Si <001> wafer the pores are formed towards the 001 direction, perpendicularly to the wafer surface, with a branched “fir tree” configuration.

The anodization procedure used to fabricate porous silicon in this thesis (see Chapter 3 for the specific conditions) allows obtaining mesoporous layers on the top of the p-type crystalline wafers, with an average diameter of 10-30 nm. After the porosification process, pSi microparticles⁶⁸ can be obtained by sonication, that fractures and disaggregates the porous silicon layer formed on the top of the Si wafer.

The size distribution and the homogeneity of the produced microparticles depend on the method by which the porous silicon wafer is fractured and is strictly correlated to this top-down fabrication approach. The most used microparticles fabrication techniques are sonication⁶⁹ or ball milling⁷⁰ starting from porous silicon layers. This procedure affects the size distribution, which is characterized by a fragments

polydispersion with random size and shape. To solve this problem, a sieving procedure can be used, with the mesh dimension dependent on the application.⁷⁰ With a different approach, photolithography was employed as patterned microfabrication technique to precisely control size, shape and porosity of the microparticles, in order to obtain a monodisperse system reliable for biomedical application.⁶⁸ In fact, as it is better described in Chapter 6, the uptake and interaction with the cells depend upon size, shape and surface properties of the particles.⁷¹

In this thesis, the problem has been investigated and solved by means of an ultrasonic post-surface functionalization procedure, which reduces the particles average size and disaggregates the pSi-COOH microparticles, without compromising the other properties, specifically photoluminescence (see Chapter 4 for details).

2.3. Photoluminescence mechanisms

Porous silicon is a light-emitting material, due to the presence of nanostructures distribution (wires and/or dots) in the silicon matrix. It emits in the spectral range from the UV to the near-infrared and has been widely investigated in particular for its photoluminescence in the visible range at room temperature. Four bands are present in the emission spectrum of porous silicon:

- (i) **UV-band** (350 nm): it was observed in oxidized samples and was related to defective oxidized states
- (ii) **F-band** (fast, 480 nm): in the blue region, it is characterized by fast decay times (in the range of ns). It is mostly found in oxidized samples and is related to contaminated or defective silicon oxide
- (iii) **S-band** (slow, 500-1000 nm): in the visible range, it is the most investigated band, also due to its tunability as a function of the sample preparation conditions (the size of the nanocrystals). It is called “slow” band because of its radiative decay times in the order of μs . It is characterized by a broadening of the band that is related to the size distribution of the Si nanostructures created by the porosification process and the position is related to the average porosity of the sample. It was determined that the S-band appears after a certain porosity threshold. The visible emission is tunable as a function of

the dimension of the nanostructures and in particular, the energy is proportional to the inverse of d^2 which is the nominal spherical radius of the nanocrystal⁷²

- (iv) **IR-band** (1100-1500 nm): in the near-IR range, its intensity increases at lower temperatures and its presence was attributed to dangling bonds.

Concerning the mechanism of porous silicon S-band light emission, the first proposed model was quantum confinement effect, which briefly finds the cause in the reduction of the dimension (i.e. the transformation from crystalline silicon to a skeleton of nanocrystalline silicon).⁵⁸ Other explanations were investigated in the past as alternatives, based on the presence of hydrogenated amorphous silicon, surface hydrides, siloxane, surface state and defects (based on the emission coming from carriers present at extrinsic centres on the pSi surface in silicon or silicon oxides).⁷³

The quantum confinement (QC) was the first supposed model,⁵⁸ since it was already be proved to explain III-V materials emission (quantum dots - QDs). For the QC model, the visible PL is related to the increased bandgap of nanosized silicon structures and this is in agreement with the PL variation depending on the size. The main QC effects are the PL upshift and tunability, the high quantum efficiency, also at long radiative lifetimes, and the variation of the PL with the temperature.

Crystalline silicon is an indirect bandgap semiconductor, thus the radiative recombination probability, and therefore the emission, is very low and in the infrared region.⁷⁴ Due to the reduction in size, the bandgap of bulk silicon (1.17 eV) is increased to more than 1.5 eV and this improves the radiative transition rate.⁷⁵ The photoluminescence results from the recombination of electron and holes, which are quantum-confined inside the nanostructures and, related to the enlargement of the band, it is shifted towards lower wavelength (higher energy). Structural and morphological analyses have proved pSi to be crystalline and correct linearity between PL emission and nanostructured size was observed.

More in details, when the porosification causes a size reduction, the HOMO (highest occupied molecular orbital) and LUMO (lowest unoccupied molecular orbital) orbitals widens. This produces a “pseudo-direct bandgap”, meaning that the electron transition does not need to be phonon-assisted and the radiative recombination

probability increases.⁷⁶ For the indetermination principle of Heisenberg ($\Delta x \cdot \Delta p \geq h/4\pi$) and $\Delta E = \frac{\Delta p^2}{2m} = \frac{h^2}{32m\pi^2\Delta x^2}$, a reduction in the dimension is related to an increase in the energy of the electrons, which are spatially confined and can then be more easily excited to the conduction band, while it is more difficult to reach the non-radiative recombination centres.⁷⁷ Furthermore, also the lifetime in the excited state increases and hence, also the radiative relaxation.⁷⁶

The tunability of the pSi PL as a function of the size is evident in Figure 2.4.

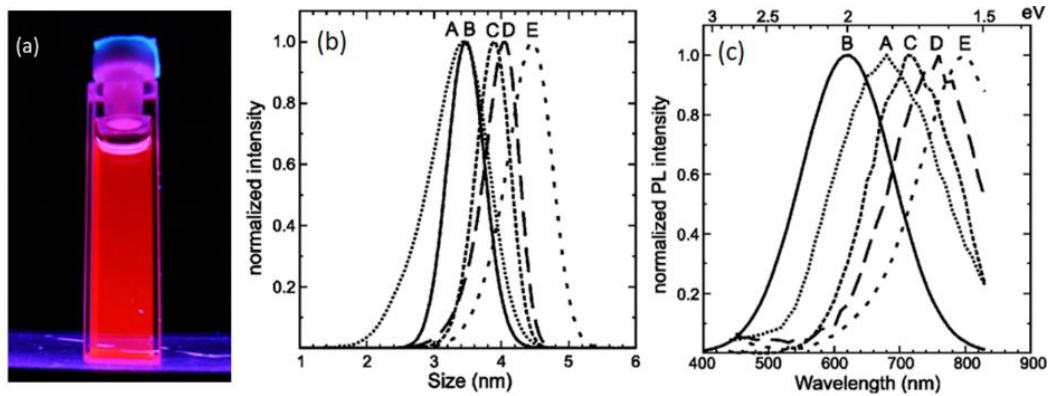


Figure 2.4 Visible PL emission of a porous silicon dispersion under UV excitation (panel a). The relation between size distribution of nanocrystals (panel b) and relative normalized photoluminescence spectra (panel c)⁷⁸

Panel a shows the photoluminescence of a porous silicon dispersion under UV excitation. The comparison between size (panel b) and PL bands (panel c) is shown: as the size increases, the emission shifts towards higher wavelength. Furthermore, the FWHM of the PL band is proportional to the width of the size distribution.

The QC effect, thus the shift of the PL towards the visible range, is true for nanostructures smaller than 5 nm and for an efficient light emission the porosity of the material should be higher than 80%, while nanostructures bigger than 10 nm do not contribute to the light emission, but absorb a lot of incident light, being the cross-section proportional to d^3 . Moreover, for bigger particles, the PL yield decreases, because it is more probable to find defects. Due to QC and since it is sufficient that $E > E_{\text{Bandgap}}$, an increase in the excitation value does not affect the PL emission wavelength, but only the intensity is reduced.

According to QC, the PL energy for pSi is shifted towards lower wavelength, with respect to bulk Si, depending on size. This behaviour is described by the formula:

[1]

$$E_{PL}(d) = E_0 + \frac{3.73}{d^{1.39}} + \frac{0.881}{d} - 0.241$$

Where, $E_0 = 1.17$ eV is the bandgap of bulk silicon, d is the size of the silicon nanocrystals and E_{PL} is bandgap of porous silicon, which corresponds to the position of the maximum value of the emission band (in eV). The terms take into account that the nanoparticles have a size distribution and the bigger ones absorb more light, without emission; the PL shifts towards the blue range as time passes; the model has to correlate the experimental results with theory and thus take into account that there could be a discrepancy between the measurements of the size and the actual value. As an example, a PL band centred at about 670 nm, corresponding to a nanocrystal size of 3.5 nm.

2.4. Surface chemistry

In 1965, Beckmann discovered for the first time slow oxidation, called “ageing”, of porous silicon.⁷⁹ In fact, as anodized samples present hydride species on the surface, which cause the material to be stable only in an inert atmosphere or in the air for a short time. When it is exposed to ambient air, certain organic solutions or aqueous media, its surface rapidly oxidizes, thus leading to degradation, corrosion and photoluminescence quenching.⁸⁰

To stabilize the optical properties a lot of treatments were investigated, and they involve the substitution of the reactive Si-H bonds, covering the pSi as anodized surface, with the more stable Si-O, Si-C, Si-N or metal surface bonds.⁸¹ This can be performed by surface oxidation, or chemical groups grafting on the oxidized or as-etched surface.

Oxidation can be thermal,⁸² performed by water, chemical,⁸³ or electrochemical.⁸⁴

- (i) The species created on the Si surface after thermal oxidation in the air or in presence of O₂ depends upon temperature and humidity. At room temperature, a lot of Si-H groups are present on the surface, but between 60 and 100

°C they are replaced by Si-O and Si-OH groups and at about 900 °C the surface is completely oxidized. After thermal oxidation, a hydrolytic condensation with organotrialkoxylane in ethanol gives the opportunity for other surface functionalization, such as PEGylation.⁸⁵ Among these procedures, rapid thermal oxidation (RTO) was found to be very efficient in preserving the nanostructures and thus the optical properties⁸²

- (ii) Water is a strong oxidant also at room temperatures and its activity is higher at basic pH, due to the Si-OH attack by the OH ions, while the stability increases at acid pH values
- (iii) ozone (O₃), DMSO (dimethyl sulfoxide), pyridine, ketones and aldehydes are able to create a thin oxide by chemical oxidation layer on the surface and allow also the further functionalization by grafting other organic molecules
- (iv) electrochemical oxidation is performed in acid solution (for example H₂SO₄) with the assistance of anodization etching to obtain an oxide layer that could be loaded by hydrophilic molecules. With this procedure, calcified porous silicon can be obtained due to Ca²⁺ ions.⁸⁶

Modification of the oxidized surface. In silanol-based chemistry, pSi is oxidized to have OH at the surface. Alkoxysilane molecules, such as APTES (3-aminopropyltriethoxysilane), are hydrolysed in water and the obtained reactive silanols interact with each other to form Si-O-Si chain on the surface (it is called the first condensation). The second condensation consists of the Si-OH interacting with the OH bond present at the surface and binding it covalently. In the case of APTES, NH₂ are introduced on the surface.⁸⁵

Modification of the as-etched surface. A possible strategy to stabilize the sample is to graft a Si-C (silicon carbide) on the as-etched Si surface by hydrosilylation, electrochemical grafting, or carbonization. Due to the low C electronegativity, Si-C is more stable than the Si-O group, thus preventing the surface oxidation.

- (i) The easiest reaction is a hydrosilylation, where a Si-H is added to a C-C (alkane), C=C (alkene) or C≡C (alkyne) and is catalysed by thermal heat,⁶⁹

- light (UV or white) irradiation, or molecules. It is effective to introduce organic functional groups on the surface, for example, carboxylic groups
- (ii) electrochemical grafting uses alkyl-based reagents with the assistance of anodization etching: the reagent is reduced in a C-based reactive molecule, to replace the Si-H with Si-CH₂R, where R varies depending on the alkyl-based molecule
 - (iii) one of the problems of the previous surface treatments is that some Si-H or reactive Si-Si is still present, thus reducing the stability against oxidation. On the contrary, Si-C is very stable and remains on the surface for years in water solutions. THCPSi (thermally hydrocarbonized porous silicon) can be produced by pyrolysis of acetylene at high temperatures, whose value determines the hydrophobicity/philicity of the sample.⁸⁷ The application of temperatures higher than 500 °C removes all the H on the surface, thus leading to TCPSi (thermally carbonized porous silicon).

Coming to the present work, two procedures were previously established to stabilize the pSi properties in ethanol for years, by introducing negatively charged (COOH) or positively charged (NH₂) groups.⁸⁸ It consists of two steps:

- (i) light-mediated hydrosilylation to introduce the COOH groups
- (ii) conjugation of amines by an amide bond between NH₂ and COOH groups.

The first step is performed on as-etched pSi with the addition of acrylic acid (an alkene chosen for its favoured entrance inside the pores) and sonication in toluene, to avoid its hydrolysis. The hydrosilylation reaction to functionalize the pSi surface is catalysed by white light, as shown in Figure 2.5: only the illuminated portion of the surface can be functionalized.

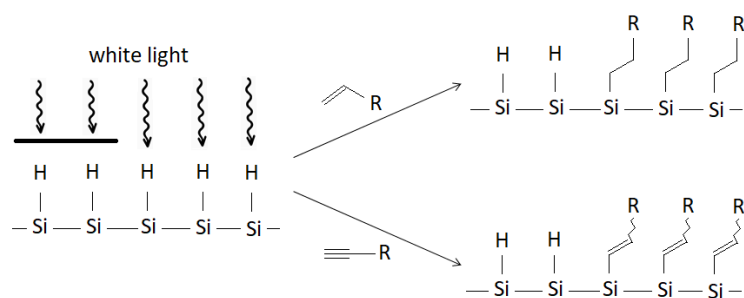


Figure 2.5 Hydrosilylation reaction to functionalize the pSi surface.

In the case of pSi-COOH sample preparation, acrylic acid is used and only the first step of the procedure is performed. To produce pSi-NH₂ microparticles, acrylic acid-NHS is used in the first step, then for the conjugation of amine groups a 4.7.10-Trioxa-1,13-tridecanediamine is used and the reaction is catalysed by DCC (Dicyclohexylcarbodiimide).

To prepare the samples investigated in this thesis work, I used the already established procedure to functionalize the surface with carboxylic groups (COOH), i.e. the first step described above, to stabilize the PL emission properties in ethanol (see Chapter 3 for more details about the reaction). Moreover, the problem of stabilization in aqueous media was previously solved by the research group by covalent attachment of organic coating (i.e. PEG and chitosan).⁸⁹ A new alternative approach is reported in Chapter 5, where the porous surface is coated with an inorganic layer of titanium dioxide by means of an innovative procedure of ALD (atomic layer deposition) in a rotary reactor. This allowed getting several months' stability, as it is presented in detail.

2.5. Main applications

Due to its unique properties, porous silicon was employed and studied in several fields. The possible application can be classified as a function of the physical form of porous silicon:

- **Powders:** for medical,⁹⁰⁻⁹² food and consumer care fields
- **Chip-based layers:** for electronics, optoelectronics, photonics,⁹³ and diagnostics
- **Powders, membranes and films:** as a catalyst,⁹⁴ energy conversion, filtration, as adsorbents, sensors and biosensors.^{95,96}

Table 2.1 shows the domains of application with some examples, whose level of activity in the academic or industrial level is qualitatively reported.⁹⁷

Table 2.1 Domains of pSi application with some examples and level of activity in the academic or industrial level.⁹⁷

Application domain	Product/function examples	Dominant physical form(s)	Academic activity level	Industrial activity level
Medical	<i>Brachytherapy, drug delivery, orthopedics, tissue engineering, imaging</i>	Microparticles	++++	++
		Nanoparticles		
		Chips		
<i>Food and nutrition</i>	<i>Nutrient protection, gum additive, functional foods</i>	Microparticles	+	+
<i>Cosmetics</i>	<i>Sunscreen, foundation excipient, drug delivery</i>	Microparticles	+	+
		Nanoparticles		
<i>Consumer care</i>	<i>Oral hygiene, shampoo, antibacterial surfaces</i>	Microparticles	+	+
Energy conversion	Batteries, solar cells, fuel cells, <i>thermoelectrics, acoustics</i> , explosives, photoelectrodes	Microparticles	+++++	+++
		Nanoparticles		
		Chips		
Catalysis	Organic pollutant removal, noble metal salt reduction	Membranes	+	
		Powders		
<i>Filtration</i>	<i>Biomolecule separation</i>	Membranes	+	+
		Chips		
Adsorbent	Microfluidic preconcentrator, toxin removal, heavy metal remediation	Membranes	+	
		Powders		
		Chips		
Electronics	RF isolation, thermal isolation, micromachining, <i>gettering</i>	Chips	++	+
Optoelectronics	LEDs, lasers, waveguides, modulators	Chips	++	+
Micro-optics	Photonic crystals, mirrors, <i>diffraction gratings</i>	Chips	+++	
Diagnostics	<i>Gas sensing, mass spectrometry</i> , biosensors, chemical sensors	Chips	++++	++

Concerning optic and optoelectronic applications, after the discovery of the PL of porous silicon at room temperature, a lot of attention has been paid to this material, to produce light-emitting devices in the UV, visible and IR regions. Furthermore, pSi LEDs were integrated with electronic components, with the aim of realizing silicon-based optoelectronic integrated circuits. The alternation of low and high porosity Si structures allows producing optical components, such as waveguides. Low porosity layers, characterized by higher refractive index, are surrounded by high porosity layers (low refracting index) and thus trap inside the light that propagates due to total reflection. By varying porosity and thickness, several numbers of propagating modes can be supported in the device.⁹⁸

In electronics, pSi can be used as gas sensor, for lithium-ion batteries, and to produce antireflection coatings for solar cells, due to the tunability of the pSi reflective index. Due to its high surface area, porous silicon is promising for gas sensing applications; by varying the electrical and optical properties, or the surface functionalization, this material was found to be effectively sensing a lot of chemical species. In fact, a variation of gas concentration can be detected indirectly by measuring the variation of PL, optical power, current and resistance.⁹⁹

Porous silicon was also investigated to be used in food, cosmetic and hygiene applications. The potentiality of pSi as functional food (i.e. nutrients with a positive effect on health) is related to the prove that its biodegradation product, orthosilicic acid, affect the bone cells health.¹⁰⁰ Furthermore, silica microparticles are already used as food additive and preliminary studies show that also pSi is chemically stable and in many stored food products. Being pSi used for drug delivery, also in food applications, it is promising for microencapsulation, protection and controlled release of ingredients (e.g. vitamins).¹⁰¹

Medical application and nanomedicine are recently very investigated fields, for the employment of porous silicon in bioimaging, bio-sensing, drug delivery, cancer therapy and tissue engineering. For therapy and diagnostic applications, both chip-based and free-standing porous silicon can be employed.

In Figure 2.6 an example of porous silicon nanoparticles applicability in nanomedicine is sketched.

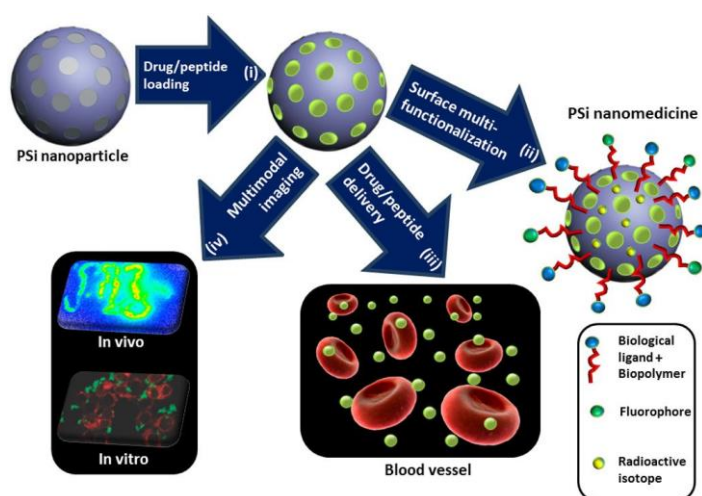


Figure 2.6 Schematic representation,¹⁰² showing pSi nanoparticles for drug loading and surface functionalization for targeted drug release and imaging in-vitro and in-vivo.

In bioimaging application, pSi can be traced by imaging techniques in real-time,^{103,104} due to its intrinsic photoluminescence in the red-NIR region. The coupling of other imaging agents allows to trace the pSi-based materials by several techniques: fluorescence imaging by conjugation of other dyes, MRI by magnetic nanoparticles loading,¹⁰⁵ SPECT or PET imaging by radiolabelling, for example with ¹⁸F,¹⁰⁶ and photoacoustic imaging by encapsulation of indocyanine green (ICG).¹⁰⁷

A biosensor is a device that includes biological elements, such as enzymes, antibodies, antigens, or nucleic acids and a physiochemical transducer. Its role is to convert the biological recognition into a measurable signal that could be optical, electrochemical and mass-sensitive.¹⁰⁸ pSi-based biosensors were investigated to detect proteins, enzymes, antibodies, or antigens specific for diagnosing cancer: the first pSi-based biosensor was used to detect penicillin by potentiometric measurements.¹⁰⁹ A quenching of porous silicon PL was proved to be related to the binding of a molecule and this effect was used to recognize DNA oligonucleotides.¹¹⁰

The porosity, with a large surface-to-volume ratio, up to 800 m²/cm³, allows the loading of a large number of molecules and hence very suitable for drug delivery.¹¹¹⁻¹¹³ Its tuneable pore volume and surface functionalization allow carrying the drug to the target, where it is released in a controlled way for any specific treatment. It has also to be marked that the pore dimension of mesoporous silicon is particularly ideal for this application.¹¹⁴ Oral, subcutaneous, intravenous, and intravitreal delivery are explored. Oral delivery was investigated for 5 model drugs,⁷⁰ finding a correlation between the dissolution properties of the drug and the release rate: pSi carriers protect the drugs and allow to increase the solubility of poorly soluble drugs.

Among cancer therapies, brachytherapy is a technique that inserts a radioisotope directly into a target tissue for in-situ treatment. pSi can be used to encapsulate the radioisotopes: clinical trials were performed on *BrachySil*TM that was injected, guided by US or CT to the target tissue having a total cancer regression in the most of the cases.¹¹⁵ Another cancer treatment is immunotherapy, where the immune system is helped and stimulated to fight against cancer, by antigen presentation.^{116,117}

For this purpose, the porosity of pSi offers a lot of volumes to load antigens; it was proved that CD40mAb (a monoclonal antibody against CD40) bound to pSi nanoparticles increased the anti-tumour activity, as compared to the antibodies on their own.¹¹⁸ Other types of cancer treatment are PTT (photothermal therapy) and PDT (photodynamic therapy). pSi can be used respectively as photothermal agent, due to the absorption of NIR light and low thermal conductivity, and it was proved to be effective, with no cytotoxic effect in controls (i.e. separate application of NIR light or pSi incubation);^{119,120} or photosensitizer, due to the ability to generate reactive oxygen species when illuminated and more favourable in the case of mesoporous silicon.¹²¹

It is also promising for regenerative medicine, where a temporary implanted 3D scaffold assists the surrounding tissue to heal itself and then is dissolved. The three-dimensional structure should act as a substrate for cell attachment and growth and a porous scaffold is very suitable for vasculature and neural growing. The incorporation of polymers (i.e. PLC, PLLA, PLGA) into pSi scaffold provides a more compatible material, with more tuneable 3D structure. One of the most investigated application is the bone regeneration, due to silicic acid produced when pSi degrades, which stimulates the calcification and the osteogenic differentiation (i.e. the differentiation into bone cells).

2.6. Light-emitting pSi microparticles for theranostics

As previously described in Chapter 1, theranostics is the integration of therapy and diagnostic in a multimodal system. As above reported, pSi structures are characterized by peculiar properties, which make them promising in the biomedical field and in nanomedicine.

Moreover, the porous layer fracture allows obtaining microparticles, that if properly tailored, are a promising multimodal system with several ranges of applications.

To summarize, porous silicon microparticles are suitable for:

- (i) being traced by imaging techniques, such as optical imaging and magnetic resonance imaging, in real-time. It is to be noted that pSi microparticles are

luminescent upon excitation in the UV range, which is not transparent in biological tissues and could make it difficult to trace them in “living matter”. This problem can be solved by using TPA (two-photon absorption) experiments; in this technique, by the simultaneous absorption of two IR photons, it is possible to excite the pSi microparticles at 700 nm instead of 350 nm and observe the photoluminescence of the microparticles

- (ii) loading a large amount of molecules with controlled-release as a function of the surface functionalization, thus being used for drug delivery and also immunotherapy applications
- (iii) being employed as photothermal agent for PTT and photosensitizer for PDT.

Last but not least, this material is biocompatible,^{122,123} biodegradable, not immunogenic and the degradation products (silicic acid) can be easily removed by the kidneys.

In this thesis, the exploitability of porous silicon microparticles as a theranostic agent has been addressed. Figure 2.7 outlines the multimodal applicability of this system as both imaging and therapeutic agent, as the final target of the research project of my thesis work.

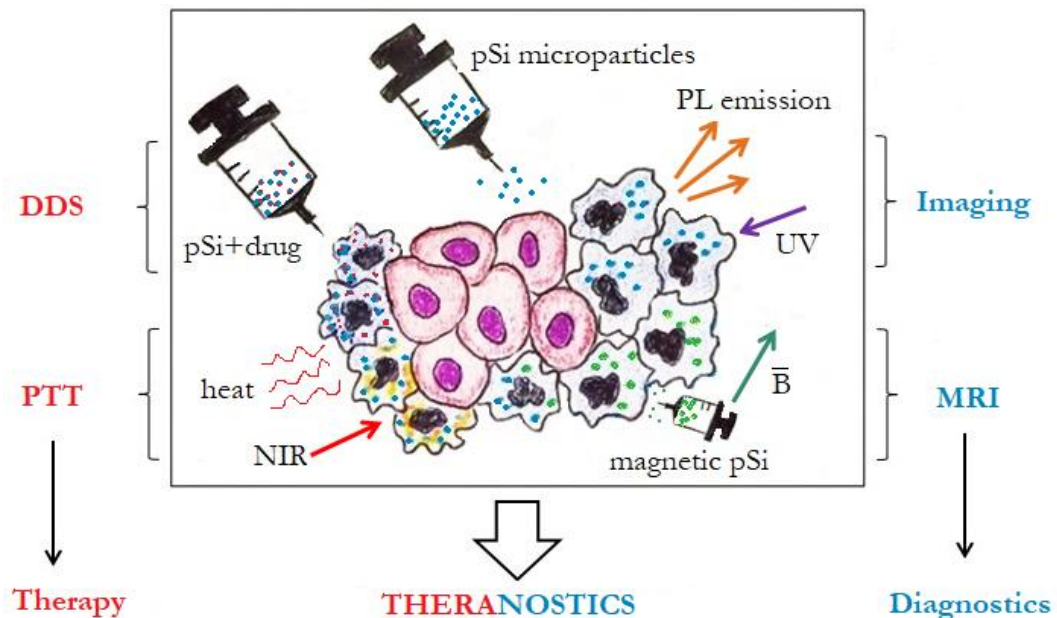


Figure 2.7 Theranostic application of pSi microparticles: as drug delivery carrier (DDS), photothermal agent (PTT), fluorescence and magnetic resonance imaging (MRI) tracer.

The scheme shows the required implementation to create a comprehensive and unique tool for theranostics:

- (i) two imaging techniques: fluorescence and magnetic resonance imaging*
- (ii) two therapeutic arms: DDS (immunotherapy) and PTT.*

Hereafter, I report the main steps that have been achieved during my thesis work, to obtain a reliable multimodal imaging and therapeutic agent, as demonstrated and deepened in the next chapters:

- after a full characterization of structural, optical and chemical properties of the fabricated pSi microparticles samples (see **Chapter 3**), ultrasonic treatment is validated in **Chapter 4** to homogenize the microparticles and to reduce the average size. This is fundamental for biological purposes since it is known that size and shape are very important parameters affecting the cellular internalization*
- the preservation of photoluminescence and structural properties in biological media (such as PBS) has been studied by surface coating with an inorganic layer in **Chapter 5**. The conservation of the photoluminescence inside human cells is evaluated by TPA (see Figure 6.7 in **Chapter 6**)*
- the assessment of biocompatibility and immune response activation is essential for the reliability of materials for theranostic applications. In **Chapter 6**, the toxicity is evaluated by viability assays, after human dendritic cells stimulation with coated and uncoated pSi microparticles, and the cell activation is evaluated by quantifying the released cytokines*
- concerning DDS applications, preliminary encouraging results have been obtained in-vitro, showing a tuneable release as a function of the surface functionalization. In **Chapter 7**, the drug loading and release capacity of the pSi microparticles is used to deliver an immune adjuvant, in perspective of immunotherapy, and the possible enhancement of the immune response is evaluated*

- *in the attempt to add magnetic properties to the microparticles and obtain a contrast agent for magnetic resonance imaging, the infiltration of magnetite nanospheres in the silicon pores is realized (see **Chapter 8**).*

The perspective of this research project is to create a unique multimodal system with all the above-listed properties. The objective is to produce pSi microparticles that can be visible in-vitro and in-vivo by fluorescence and magnetic resonance imaging, used for drug loading and controlled release of molecules (e.g. agonist of toll-like receptors, in perspective of immunotherapies). Further experiments will evaluate the feasibility to use this material as a PTT agent for cancer treatment, due to the high absorption in the NIR region, to complete the project. Moreover, next work is directed towards the applicability of pSi microparticles for in-vivo experiments, thus evaluating the bio-distribution and the behaviour of such material in more complex environment respect to the cell culture.

CHAPTER 3

POROUS SILICON MICROPARTICLES FABRICATION AND FUNCTIONALIZATION

This chapter focuses on the fabrication and the functionalization of porous silicon microparticles obtained by electrochemical etching in anodization cell and light-driven carboxyl-functionalization. The experimental procedure implemented in the fabrication process and the successive functionalization protocols to passivate the surface are described in details.

The fabricated samples are characterized by analysis of the surface, and the study of optical and structural properties by means of FTIR (Fourier transform Infrared) spectroscopy, fluorescence spectroscopy, DLS (Dynamic light scattering), electron microscopy and optical microscopy.

3.1. Fabrication and functionalization procedures

Porous silicon was obtained starting from boron-doped p-type Si wafers (<100> oriented, 10–20 Ω/cm^2 resistivity, purchased from University wafers, Boston MA). The porous structure was induced on the wafer surface by electrochemical etching in PTFE anodization cell with a platinum cathode at a constant current (80 mA/cm^2) in an ethanol solution containing 16% HF v/v for 15 min. The layer was removed from the wafer surface by scratching it and stored in toluene. This procedure was repeated about 5 times and then, the obtained pSi powder, in 5 mL toluene, was fragmented into microparticles by 20 min sonication in a thermal bath.

The scheme of the experimental setup used for the porosification of Si wafer is shown in Figure 3.1 (a), where the cylindrical cell is made of PTFE to resist the HF corrosion; the Si wafer is placed on a metal disk with the only upper face in contact with the acid solution and the cathode of the anodization cell is a platinum grid immersed into the solution.

The light-emitting pSi microparticles properties were stabilized by a light-driven hydrosilylation. A scheme of the experimental setup used for the functionalization is shown in Figure 3.1 (b).

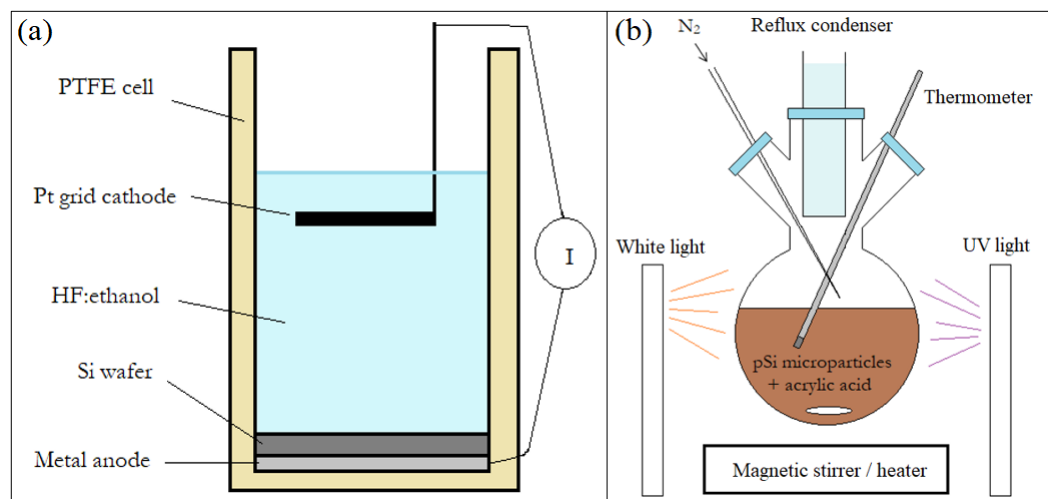


Figure 3.1 Scheme of single electrochemical cell used for pSi porosification in HF:ethanol solution (panel a) and experimental setup used for the carboxyl-functionalization of porous silicon microparticles (panel b).

The functionalization setup is composed of a flask fitted with a reflux condenser, where the flowing of cold water lets the solvent (toluene) not to evaporate, a thermometer and N₂ mild flow. 50 mM acrylic acid is added to the pSi microparticles powder in toluene and the reaction goes at 50 °C, under mild stirring and nitrogen flow for two hours. This functionalization is needed to introduce carboxyl groups on the microparticles' surface. Then, the solution (pSi-COOH microparticles in toluene) was washed several times by centrifuging, removing the supernatant and rinsing with ethanol (the sample is labelled as pSi-COOH). The sample is then stored in ethanol at room temperature.

It is important to note that, the electrochemical etching used to produce the pSi microparticles allow to obtain just some milligrams of powder and this fact is a central point in the experiments reported in the next chapters.

I prepared several samples, whose fabrication procedure has been settled and is now well established,⁸⁸ at the Nanoscience Laboratory in the Physics Department of the University of Trento, in collaboration with Prof. Marina Scarpa. Here, I report the

most significant ones (labelled as pSi-COOH_1, pSi-COOH_2, pSi-COOH_3 and pSi-COOH_4), which were used for further experiments, reported in the next chapters, and are prepared and functionalized under the same experimental conditions. The chemical, optical and structural properties were investigated.

3.2. Characterization techniques

Chemical, optical and structural properties of the samples (pSi-COOH_1,2,3,4) were accurately investigated before moving to further steps either in post-fabrication microparticles preparation (i.e. specific surface coating, ultrasonic treatment) or in testing them in in-vitro experiments.

In Table 3.1, the instrumentation used to characterize the samples and the information that can be obtained are reported.

Table 3.1. Characterization techniques and related information.

Characterization	Technique	Measurement information
Surface	FTIR Spectroscopy	Surface chemical groups
	DLS	ζ -potential
Optical	Fluorescence spectroscopy	Photoluminescence, PLE, Lifetimes, Quantum yield
	DLS	Average dimension
Structural	TEM/EDS	Morphology, dimension and porosity
	SEM	Surface morphology

The surface properties were investigated by FTIR spectroscopy, to determine the surface chemical groups, by DLS to obtain the ζ -potential (i.e. the surface charge) and by EDS to determine the elemental composition. The elemental analysis is reported in the structural characterization paragraph (3.3.3) for the sake of convenience since the EDS instrument is coupled to the TEM.

The photoluminescence was investigated by spectrofluorometer, to determine photoluminescence, lifetime and to perform PLE experiments. The light efficiency of the samples was evaluated by quantum yield (QY) measurements by means of the comparative method.¹²⁴

The structural properties were studied by DLS, to determine the size distribution of the samples; by SEM and TEM to investigate the morphology, the average size and the porosity.

DLS is usually used for the size evaluation of nano- and micro-particles in simple solvents or biological buffers, because it is a fast and cheap technique, with good statistical significance with respect to TEM and SEM,¹²⁵ for which samples has to be dried before the observation. Differently, the electron microscopies allow investigating the particle morphology, porosity and agglomeration. A comparison between these techniques and also optical imaging is shown in section 3.3.3.

The details of the instrumentation and of the measurement procedure are reported in Appendix A1. I performed the characterization at the University of Verona, with the instrumentation of CPT (Centro Piattaforme Tecnologiche), except for FTIR spectroscopy, which was used at the Nanoscience Laboratory (Department of Physics) of the University of Trento, and electron microscopy observations, that were done in collaboration with dr. Gloria Ischia at the Department of Industrial Engineering of the University of Trento.

3.3. Samples characterization

Here, I report the study and comparison of the properties of the samples, divided by the type of characterization.

3.3.1. Surface properties

The surface chemistry of the COOH-functionalized pSi microparticles, produced according to the protocol reported in the previous section, was analysed by FTIR spectroscopy. This analysis is fundamental to determine the stability of the material and for further possible drug loading.

The absorption spectra of the pSi-COOH microparticles are reported in Figure 3.2. The presence of the C=O peak means that the functionalization was successful.

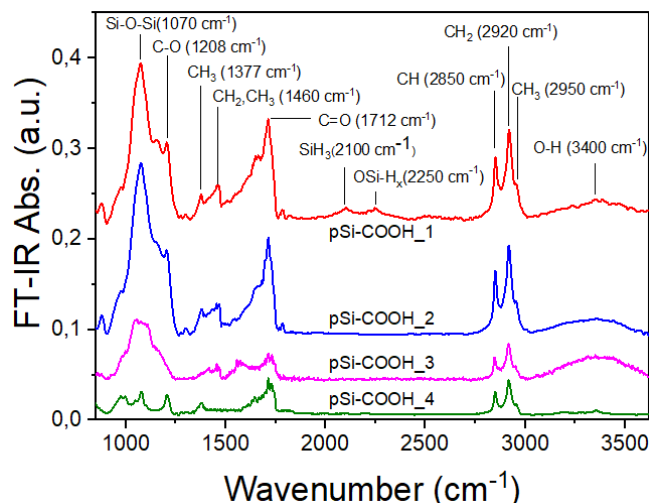


Figure 3.2 FTIR absorption spectra of pSi-COOH microparticles. The spectra are vertically shifted for better visualization. The main absorption peaks are pointed out.

The presence of a peak at 1070 cm^{-1} and related to the Si-O-Si group,¹²⁶ means that the samples are partially oxidized and this is confirmed by the broad OH band at 3300 cm^{-1} . The peak at $2100\text{-}2300\text{ cm}^{-1}$ in pSi-COOH_1, is related to the S-H stretching vibrations.¹²⁷ To verify if the carboxyl-functionalization was effective, we should look for a peak at 1712 cm^{-1} , related to the C=O bond, which is clearly visible in all spectra. The presence of the stretching modes of the alkyl-CH peaks between 2850 and 2950 cm^{-1} supports the presence of the organic functionalization.¹²⁸ Moreover, we can observe that some carboxylic groups are hydrogen-bonded,¹²⁹ as proved by the broadness of the peak and by the absorbance range. The band at 1620 cm^{-1} could be attributed to the non-reacted C=C bonds of the acrylic acid used during the functionalization reaction, nonetheless, also a band at $960\text{-}990\text{ cm}^{-1}$ related to the out-of-plane vibration of acrylates should be therefore present,¹²⁸ but it is scarcely visible. Figure 3.2 shows the same chemical groups present on all the pSi microparticles samples, meaning that they are similar from the chemical point of view, as expected. In particular, for sample pSi-COOH_3 and pSi-COOH_4 we can also observe that the peaks related to the organic passivation are less intense with respect to the peaks introduced after the oxidation.

3.3.2. Optical analysis

The optical emission properties investigated by spectrofluorometer are reported. In particular, photoluminescence, PLE experiments, lifetime and QY (quantum yield) were compared among the samples.

Photoluminescence. Figure 3.3 shows the PL spectra of pSi-COOH micro-particles dispersed in ethanol by excitation at 350nm (panel a) and the normalized spectra (panel b). The values of λ_{\max} and FWHM of the samples PL spectra are reported in Table 3.2.

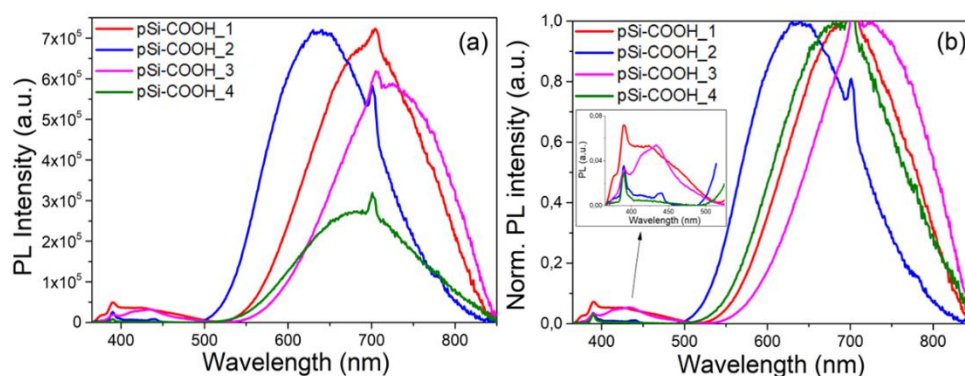


Figure 3.3 PL of pSi-COOH samples (a) and PL normalized with respect to the peak maximum value (b), by excitation at 350nm. Inset: zoom on the blue band.

Table 3.2. λ_{\max} and FWHM of the PL bands are reported.

Sample	λ_{\max} [nm]	FWHM [nm]
pSi-COOH_1	690	165
pSi-COOH_2	640	155
pSi-COOH_3	730	160
pSi-COOH_4	680	165

The PL orange-red band of the samples is centred between 600 and 700 nm and a small blue band at 420 nm is present for all the samples. As discussed in Chapter 2, the pSi microparticles were functionalized, in previous work, with carboxylic (COOH) and amine (NH₂) groups to stabilize the PL emission properties in ethanol and their optical properties were investigated.⁸⁸ In the case of the amine-functionalization, the photoluminescence, beyond the orange-red band, was characterized by a blue band centred at about 420 nm, whose appearance was ascribed to the impurities introduced at the silicon interface. A similar peak is shown also in these pSi-COOH samples, but much less intense with respect to the orange-red band.

(Further investigation are shown in the next paragraphs). The sharp peak at 390 nm is related to the Raman effect of water¹³⁰ and the peak at 700 nm is the second order of the excitation wavelength (i.e. 350 nm). The difference in PL intensity of the first three samples differs just for 10%, while the intensity of sample pSi-COOH_4 is reduced by 50% with respect to the others. Since the concentration of this sample is comparable with pSi-COOH_3, we could deduce that not all the fourth sample is light-emitting, caused by an issue during the synthesis and functionalization procedure. The difference in λ_{\max} depends on the nanocrystal size produced during the porosification: for example, sample pSi-COOH_3 shows a photoluminescence red-shift meaning that the porous walls of the microparticles are formed by larger nanostructures.

Although the preparation procedure was the same for all the samples, a variation in the optical properties is observed. This could be attributable to the differences in the starting c-Si wafers (nominally equal) used to fabricate the microparticles. In fact, the differences among the porous silicon characteristics could be caused by small differences in wafer resistivity.¹³¹ The effects to small changes in resistivity (ρ) are an important issue of the fabrication approach; in fact, the ρ value of the wafer (inversely proportional to the concentration of dopant in the Si crystalline structure) is one of the primary feature affecting the porosification process and the photoluminescence of the material. Unfortunately, it is difficult to purchase wafers with a ρ value constant on the whole surface and equal to the nominal one. On the contrary, the wafer resistivity varies radially on the surface and this adds to the fact that, in order to obtain enough pSi powder, the same portion of the wafer ($\Phi = 3.5$ cm) is re-etched some times. Thus, the decreasing of the wafer width results in a variation of the resistivity. These differences, even if small, have significant effects on the resulting properties of the pSi microparticles. Moreover, we can observe a slight inhomogeneity of the as-etched surface colour, which is related to the variation in current density near to the O-ring delimiting the etching area. All of these considerations contribute to the explanation of the differences among the pSi samples characteristics.

Quantum Yields (QY). The quantum yields were obtained by a comparative method with the formula $QY_s = QY_r \frac{I_s}{I_r} \frac{A_r}{A_s} \left(\frac{n_s}{n_r}\right)^2$, using a previously prepared sample as a reference, whose QY_r (0.8%) was determined by comparison with fluorescein. The results are of the order of 1%, value compatible with previous findings.¹³²

PLE Experiments. Furthermore, we investigated the behaviour of the photoluminescence as a function of the excitation wavelength. In particular, λ_{ex} was varied from 325 nm to 450nm, with a step of 25 nm, and λ_{max} value, FWHM and the integrated area of the whole orange-red PL band were determined. The results are reported in Figure 3.4 (panel a, b and c), for all the pSi-COOH samples, where no significant difference is found as a function of the excitation wavelength according to the quantum confinement model. The PL spectrum is independent on the excitation wavelength since it is enough for the electron to have the energy necessary to go to the excited state.

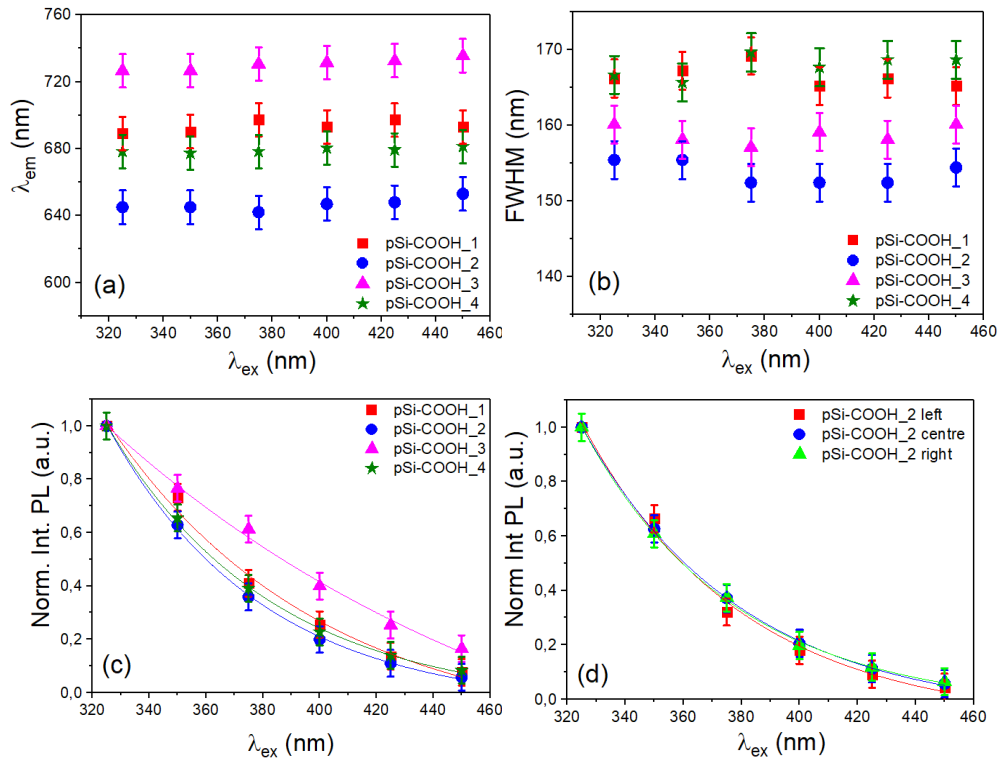


Figure 3.4 λ_{max} (panel a), FWHM value (panel b), PL band integrated area, normalized by the maximum value, for all the samples (panel c) and for three different regions of the PL band, for sample pSi-COOH_2 (panel d) excited at different λ_{ex} .

Then, we compared the contribution of three different portions of the emission curve (10 nm width, centred at 550 nm, 650 nm, 750 nm and labelled as left, centre

and right) in order to see if there were different contributions related to the different portion of the PL band and to validate the quantum confinement effect explanation. As it was performed before for the whole PL band (Figure 3.4, panel c), the integrated area values relative to the marked portions of the PL band are reported in Figure 3.4 (panel d), as a function of the excitation wavelength, for a representative sample (pSi-COOH_2).

As it can be observed in panel a and b of Figure 3.4, the FWHM and λ_{max} values are constant as the λ_{ex} is varied, while the integrated PL area decreases exponentially as the excitation wavelength increases. Furthermore, the order of the exponential fit is in agreement with the emission wavelength of the samples, as expected. For this representative sample, we observed no dependence on the different regions of the emission band. In fact, the normalized integrated PL regions are compatible within the error bar.

Lifetimes. The obtained decay curves are reported in Figure 3.5 (panel a), while the dependence on the emission wavelength is reported in the panel b and c for a representative sample (pSi-COOH_2).

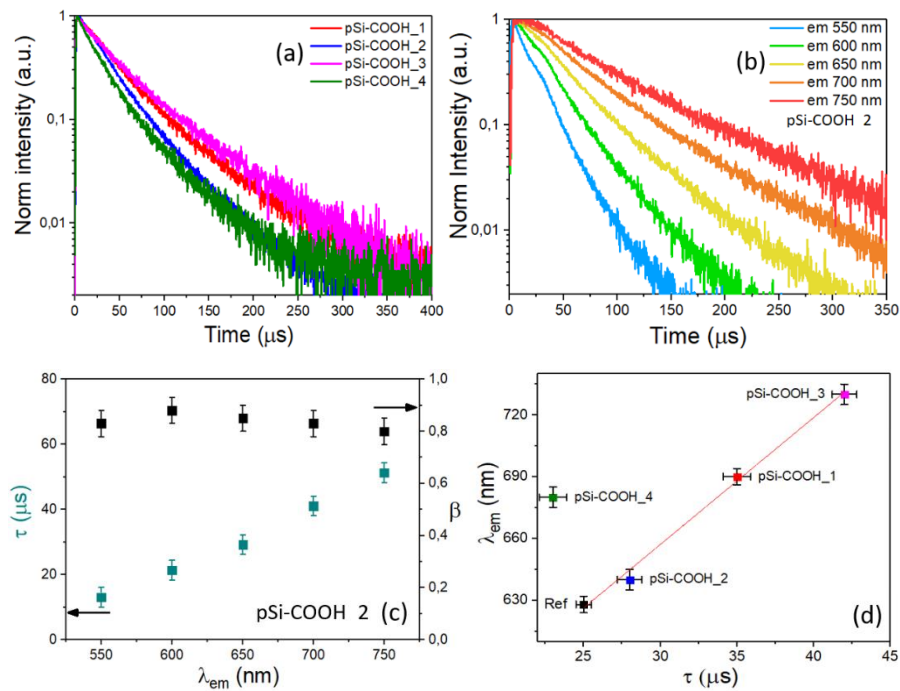


Figure 3.5 Decay curve of the PL of pSi-COOH microparticles by excitation at 325nm and emission at λ_{max} for each sample (panel a); varying λ_{em} (panel b) and results of the decay curve fitting (τ and β) as a function of the λ_{em} (panel c) for a representative sample (pSi-COOH_2). The linear relation between λ_{em} and t , for each sample (panel d).

For each sample, the PL decay curve of the orange-red band (in the μs range) and of the small blue band (in the ns range), whose presence was firstly found in the case of NH_2 functionalized pSi microparticles were investigated by a pulsed lamp and by nanoLED excitation, respectively. Concerning the orange-red lifetime, the excitation was fixed at 325 nm and the emission wavelength at the λ_{max} of each sample. The exponential decay fit of the decay curves allows obtaining the lifetime τ .

An example of the PL dynamic (obtained with pSi-COOH_2) is shown in Figure 3.5 (panel c) while the lifetime and β values of the prepared samples are reported in Table 3.3. The obtained data in Figure 3.5 (panel a and b) were fitted by a stretched exponential curve $I = I_0 e^{-(t/\tau)^\beta}$, τ is lifetime and β the stretched parameter.

Table 3.3. Lifetime τ and stretched exponential β , determined from Figure 4.3 (panel a) are reported, for all the samples.

Sample	τ (μs)	β
pSi-COOH_1	35.3 \pm 0.9	0.79 \pm 0.05
pSi-COOH_2	28.0 \pm 0.8	0.81 \pm 0.05
pSi-COOH_3	41.8 \pm 0.9	0.79 \pm 0.05
pSi-COOH_4	23 \pm 1	0.75 \pm 0.05

For all the sample, a radiative lifetime of few tens of μs and β values of 0.8 were found, as expected.⁷⁷ Panel c shows the linear dependence between the lifetime and the emission wavelength, and the absence of correlation between β values and λ_{max} (for pSi-COOH_2 as representative sample). Furthermore, it is clear for sample pSi-COOH_1, 2, 3 that the lifetime increases linearly as the maximum of PL increases, as expected and shown in panel d. These outcomes, plus the typical lifetime values, demonstrate quantum confinement effect as the light emission mechanism.^{88,133} In this explanation, sample pSi-COOH_4 is an outlier data, as clearly shown in Figure 3.5, panel d, and this could be explained by the fact that it is a less homogeneous sample and just a part of the sample contributes to the photoluminescence. This assumption can be justified by two facts: the first, is the heterogeneity of the sample,

as confirmed by the TEM images in the following, together with the nanoscale structure, that shows smaller pores with respect to the other samples. The second is the reduced quantum yield with respect to samples pSi-COOH_1,2,3; in fact, PL intensity normalized to the absorbance of sample pSi-COOH_4 is halved with respect to the others, thus obtaining a QY of about 0.5 % with respect to the 1.2% obtained for pSi-COOH_1.

The decay time of the small “blue” PL band at about 420 nm (see inset of Figure 3.3, panel b) was investigated for all the pSi microparticles. In this case, the decay times are much shorter (nanoseconds range), thus the samples were excited with a nanoLED (335 nm excitation wavelength and pulse width < 1 ns).

In order to be sure of the physical explanation of the PL signal (i.e., quantum confinement effect for the orange-red band and surface defects for the blue band), in Figure 3.6 we investigated the PL decay curve of both orange-red and blue bands, in ns (panel a) and μ s (panel b) ranges. This was evaluated for pSi-COOH_2, as a representative sample.

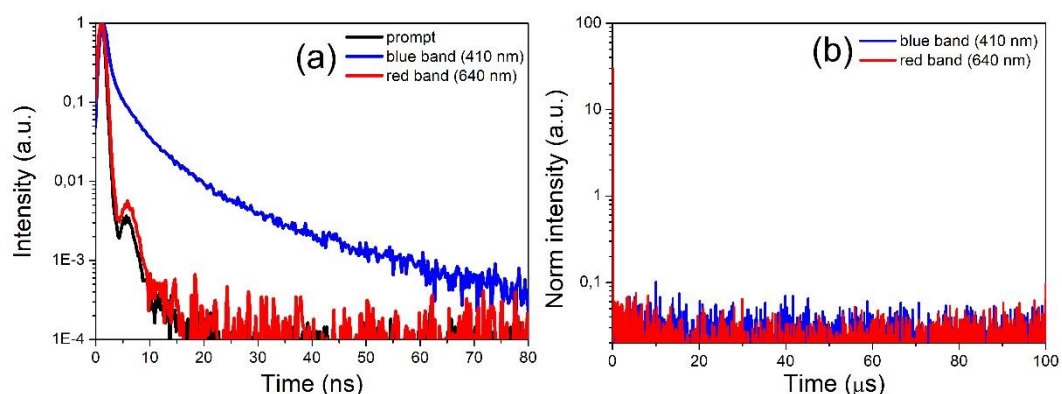


Figure 3.6 Decay curve of the PL of pSi-COOH microparticles by short-pulsed excitation at 335 nm and emission in the blue and red band of the PL: measurement in the ns range (left panel) and in the μ s range (right panel).

As it can be seen from Figure 3.5, we detected a signal only in the case of the blue band in the ns range, meaning that the origin of the blue band PL signal is related to recombination at the surface.

The presence of the blue band in the PL spectra was previously observed and investigated by Veinot et al.¹³⁴ In a colloidal system of Si nanocrystals (BES) and compared to similarly dodecene-capped ones emitting in the red (RES). Since the

incoming photon induces an exciting, where Bohr radius is larger than the Si core, it is clear that the surface properties play an important role in the emission mechanisms. In their study, Veinot et al. ascribed the difference in the emission wavelengths to the presence of low-density traps (B and R for blue and red emission, respectively). While the red emission is size-dependent and explained by the QC effect, the blue emission is to be attributed to the presence of low-density N impurities, introduced during the NCs synthesis. When R and B traps are completely filled, the excursions are localized in T traps, which have an origin in the presence of oxygen impurities. Similarly, the samples investigated in this chapter show a PL blue band, but very weak in intensity, whose presence was confirmed by the time-resolved fluorescence spectroscopy. Hence, the presence of this band could be ascribed to the introduction of low-density oxygen and nitrogen impurities during fabrication and functionalization of the samples.

Thus, we studied the PL dynamics of the pSi-COOH samples by nanoLED excitation and reported the results in Figure 3.7 (panel a). Panel b shows the PL decay by varying the emission wavelength (400 nm to 440 nm) and in particular no dependence on λ_{em} .

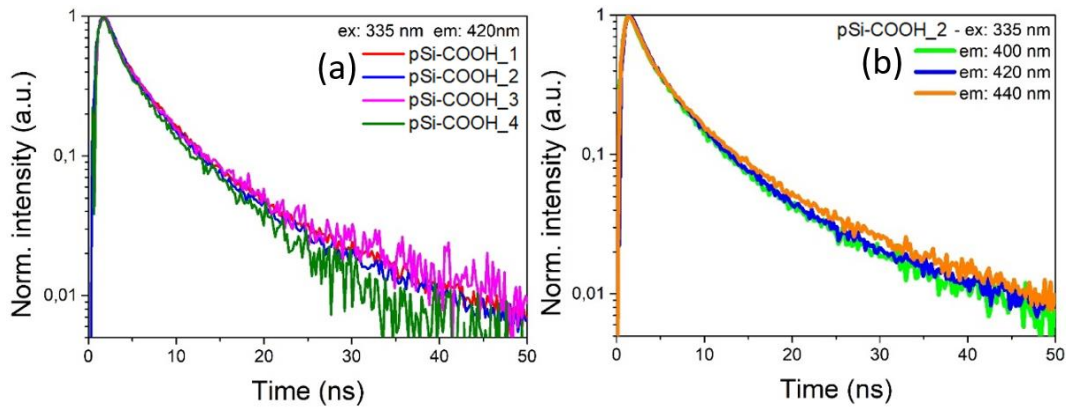


Figure 3.7 PL Decay curve by nanoLED excitation at 335 nm and emission at 420 nm, for all the samples (panel a) and by varying emission (400 nm, 420 nm, and 440 nm) for sample pSi-COOH_2 (panel b).

To obtain the lifetime τ , the data were fitted with a single decay (i.e. not stretched) exponential function $I = I_0 e^{-t/\tau}$, according to the previous findings for NH₂ functionalized samples, and the results are reported in Table 3.4.

Table 3.4 Lifetime values τ , determined by fitting the data of Figure 3.7 by a single decay exponential function $I = I_0 e^{-t/\tau}$.

Sample	τ (ns)
pSi-COOH_1	4.6±0.5
pSi-COOH_2	4.4±0.3
pSi-COOH_3	4.7±0.6
pSi-COOH_4	4.3±0.7

The obtained lifetime values are about 5 ns for all the samples, in agreement with previous findings, as discussed in the previous paragraph for the steady-state photoluminescence. They are not compatible with quantum confinement effect, but attributable to non-radiative recombination at the surface of pSi.^{88,135}

3.3.3. Structural characterization

The microstructural characterization of the samples was performed by TEM/EDS and SEM analysis, to evaluate the morphology of the samples, estimate the porosity and determine the average dimension, by means of the sample interaction with an electron beam probe. While TEM analysis gives information on the structural inner part of the sample since the electron beam passes through the sample, SEM is used to analyse the sample surface and composition: the backscattered electrons give information on the surface morphology; the secondary electrons are emitted from the atoms of the sample, therefore giving information on its composition. The coupling of the instrument with an EDS spectrometer allows investigating the elemental composition of the sample.

The elemental analysis was performed for all the samples by EDS and the spectrum for a representative sample, pSi-COOH_1, is reported in Figure 3.8. In the inset, the area on which the measurement was performed is shown.

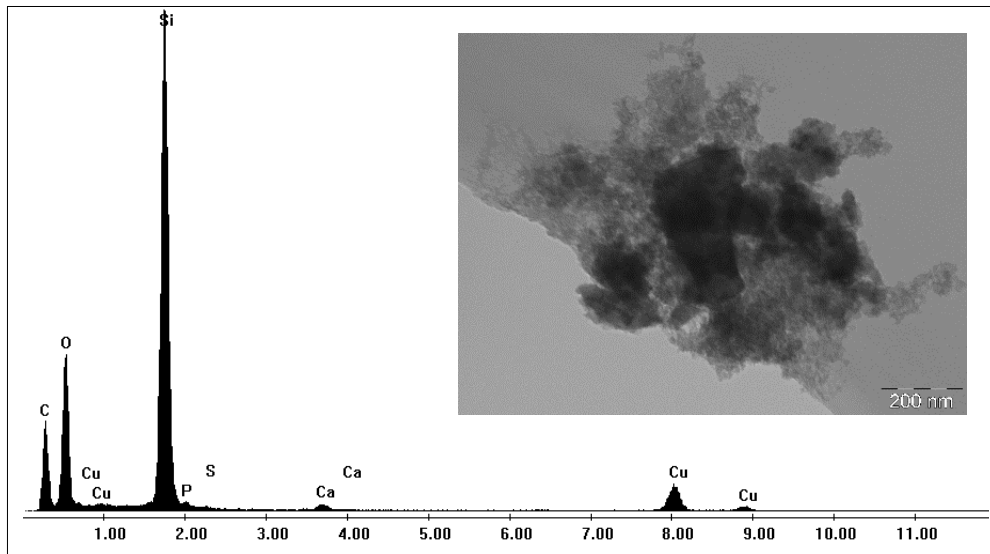


Figure 3.8 Elemental analysis performed on the region shown in the inset, for a representative sample, pSi-COOH_1.

In the EDS spectrum the peaks relative to the pSi-COOH microparticles are present, i.e., Si, O and C, beside them, the Cu peaks are due to the sample holder.

TEM observations are reported in Figure 3.9, where, for all the samples, agglomerates of microparticles of few μm and less than $1 \mu\text{m}$ can be seen.

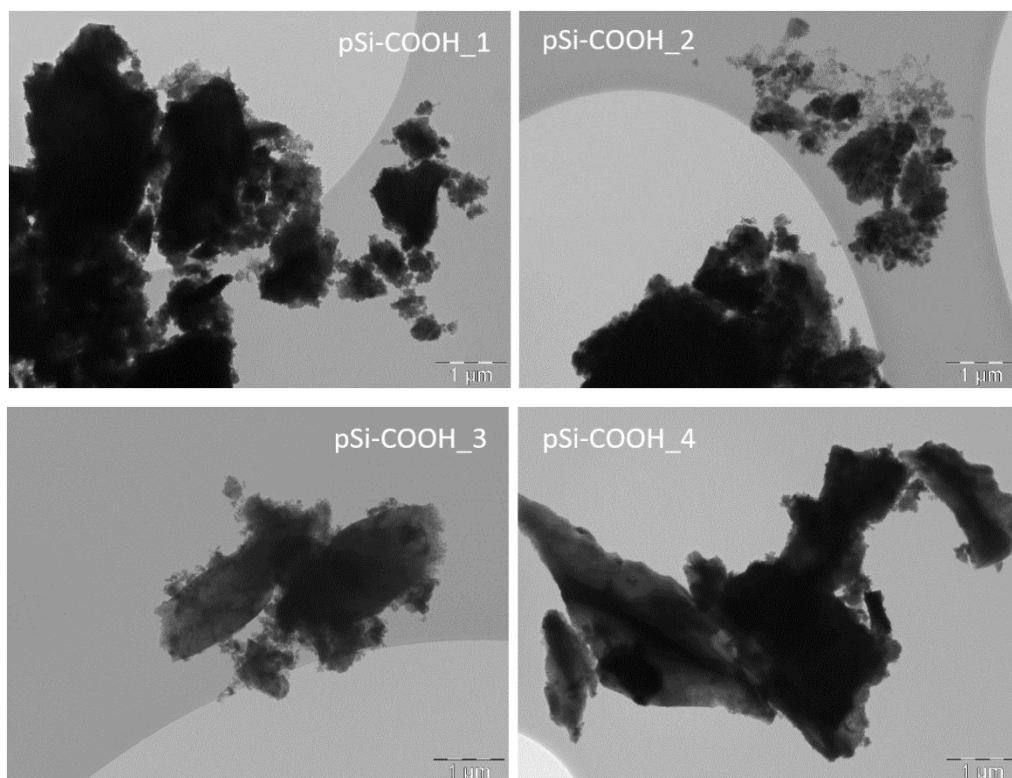


Figure 3.9 TEM images of the samples at $1 \mu\text{m}$ range, the name of the sample is reported.

Figure 3.10 shows an SEM image for the morphological characterization (panel a) and a TEM image for the pore size determination (panel b), for a representative sample, pSi-COOH_1.

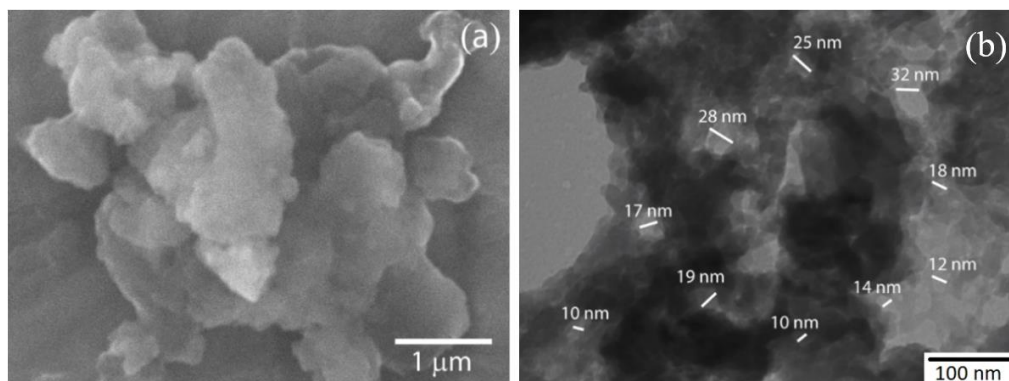


Figure 3.10 Morphological characterization of pSi-COOH_1 by SEM (a) and microstructural characterization by TEM (b) for the pore size determination.

The TEM images were analysed by *ImageJ* software to determine the average microparticles dimension and the pore size: the values were obtained measuring by hands hundreds of samplings, in different portions of the sample and the results are reported in Table 3.5.

DLS technique was used to estimate the surface charge and size distribution of pSi-COOH microparticles. In particular, the ζ -potential is an important parameter to be assessed towards biomedical applications and cells interaction. Thus, we had to re-suspend the microparticles in PBS for in-vitro studies and measure the ζ -potential in this buffer. The average size and surface charge of the samples are reported in Table 3.5.

Table 3.5 Average size and porosity obtained by the TEM images analysis and DLS and ζ -potential values of the prepared samples.

Sample	TEM		DLS	
	Pore size (nm)	Particle size (nm)	Particle size (nm)	ζ -potential (mV)
pSi-COOH_1	16±6	900±470	1200 ± 220	-41 ± 3
pSi-COOH_2	16±5	820±510	1100 ± 250	-35 ± 1
pSi-COOH_3	17±3	730±650	1300 ± 260	-29 ± 2
pSi-COOH_4	5±1	780±630	1500 ± 480	-25 ± 1

It can be seen that all the microparticles have a negative surface charge of a few tens of mV and this is compatible with previous findings for similarly functionalized pSi microparticles.¹³² To better evaluate the dimension of the pSi microparticles, we considered optical image analysis and a comparison between the size distribution obtained by DLS, TEM and optical imaging is reported in Figure 3.11.

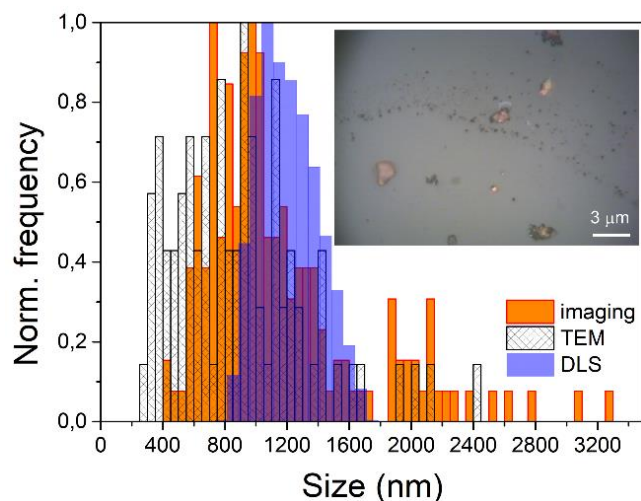


Figure 3.11 Comparison of the microparticles size distribution for pSi-COOH₂ obtained by optical image analysis, TEM and DLS. An example of an optical image is shown in the inset.

To compare the obtained results, it has to be considered that the size distributions estimated by TEM and optical images are based on the number of particles in a studied area and size class; on the other hand, the size distribution obtained by DLS is based on the light intensity scattered by the microparticles and this includes an overestimation. Furthermore, TEM analysis shows a smaller average size of the microparticles, because this technique is much more sensitive to a smaller dimension. Differently, DLS is a better technique to detect also bigger microparticles and the obtained distribution is affected by shape inhomogeneity. Moreover, the techniques differ for the fact that DLS is performed in solution, thus measuring the hydrodynamic dimension of the microparticle, while for the imaging techniques the sample has to be deposited and dried on a substrate. In conclusion, we could observe that DLS, in this case, is a good compromise for obtaining correct and reproducible results with a cheap and quick measurement.

3.4. Conclusions

The pSi-COOH microparticles samples under investigation were prepared with the well-established protocol of anodization etching in HF:ethanol solution. The different optical and structural properties observed in the investigated samples was caused mainly by the slight variation in the starting wafers resistivity, which affect the porosification process.

From a chemical and microstructural viewpoint, we obtained a good reproducibility among the fabricated samples, as shown by FTIR spectra and SEM images. However, the pSi microparticles resulted in different nanostructured sizes, which caused slightly different photoluminescence: pSi-COOH_3 sample has a PL emission at a longer wavelength and longer lifetime values according to larger light-emitting nanostructures.

Concerning the structural properties and the average size of the microparticles, the results obtained by optical imaging and TEM images analysis are consistent with the results of DLS technique, despite the difference in sensitivity, the field of view and the limitation in the statistical significance of the analysed images.

CHAPTER 4

POST-FUNCTIONALIZATION ULTRASONIC TREATMENT

The fabrication and functionalization procedures described in the previous chapter produce light-emitting microparticles with a simple and cheap top-down fabrication process. This approach allows to obtain surface coatings of several chemical nature and charge, but the microparticles average size and size distribution are difficult to be controlled. However, this is an important parameter to be considered and to play with, in order to have a material as a viable platform for biomedical applications. In fact, it is to be reminded here that the size and, in general, the structure and the shape of the microparticles, as well as their surface functionalization, strongly affect the response of the cell and the possibility of internalization.^{136,137}

<i>Problem</i>		<i>Solution</i>
<i>Broad size distribution</i>	→	<i>Ultrasonic treatment</i>

In this chapter, we report a simple post-functionalization procedure based on ultrasounds (US) to better control these features: to reduce the average size, narrow the size distribution and avoid the microparticles agglomeration. When ultrasounds (waves at frequency > 20 kHz) pass through a medium, they create inside bubbles, which grow and, after reaching a certain dimension and because of the induced pressure variation, collapse. The technique based on the US is able to release a lot of energy¹³⁸ and therefore, the US probe type is usually employed for the fracture and the homogenization of powders.¹³⁹

Specifically, we investigated the effect of the US treatment in terms of duration and power density, on photoluminescence and structural properties of the microparticles.

4.1. Experimental procedures and techniques

The samples (labelled as pSi-COOH_1, pSi-COOH_2, pSi-COOH_3 and pSi-COOH_4 – see Chapter 3 for details) were prepared to test and validate a post-fabrication process based on an ultrasonic treatment to get homogeneous and narrower size distributions and to reduce the average dimension of the pSi microparticles. The procedure, based on ultrasounds (US), is reported in Figure 4.1.

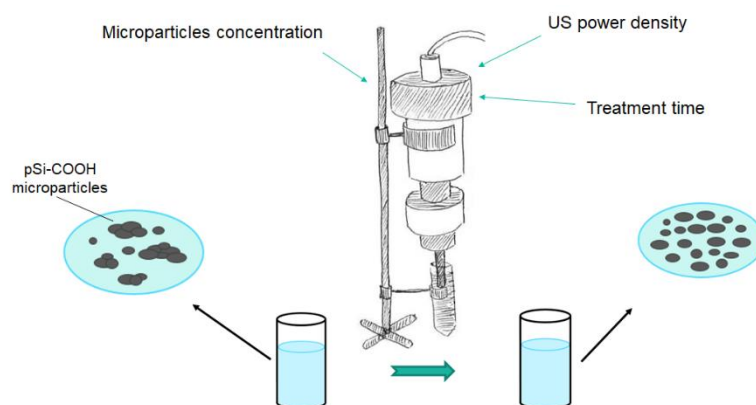


Figure 4.1 Scheme of the procedure based on ultrasounds used to homogenize the samples.

To investigate the ultrasonication (US) effect, post COOH functionalization, pSi-COOH microparticles were treated by *Bandelin Sonopuls Ultrasonic Homogenizer HD 2070*, with a 2 mm diameter probe working at an amplitude of $200 \mu\text{m}_{\text{ss}}$, at a constant frequency of 20 kHz and power of 70 W; during the treatment the probe was immersed into half of the test tube, containing 1 mL of the sample. We studied the ultrasonication effect on the pSi microparticles structural and optical properties of one sample, by varying the concentration of the solution and the treatment parameters, which are the time of treatment and the power density. Then, we chose the most efficient set of parameters to perform the treatment on all the other samples.

The effect of the post-functionalization treatment was evaluated, by investigating the optical (both photoluminescence and lifetime) and the structural properties of the samples. I performed the characterization at the University of Verona, with the instrumentation of CPT (Centro Piattaforme Tecnologiche). The electron microscopy observations for the structural analysis was done in collaboration with dr. Gloria Ischia at the Department of Industrial Engineering of the University of Trento.

The instrumentation used and the relative obtained information are reported in Table 4.1. The details of instrumentation and measurement procedure, used for structural and optical characterization, are reported in Appendix A1.

Table 4.1. Characterization techniques and related information

Characterization	Technique	Measurement information
Optical	Fluorescence spectroscopy	Photoluminescence, Lifetimes
Structural	DLS	Average dimension
	TEM/EDS	Morphology, dimension, porosity
	SEM	Surface morphology

4.2. Optimization of the ultrasonic treatment

The ultrasonic treatment was primarily investigated by the DLS technique to have evidence about the effectivity in reducing the average microparticle size and in narrowing the size distribution. The US treatment has been performed as a function of the main process parameters thus investigating the effect of:

- (i) treatment duration (5 to 20 minutes),
- (ii) power density (42 W/cm^3 or 21 W/cm^3),
- (iii) microparticles concentration in solution (10 mg/mL or 2 mg/mL).

The results of this preliminary study are reported in Figure 4.2 for a representative sample, where the distribution size (panel a) and the relative average value (panel b) are reported, as a function of treatment time, power density and sample concentration.

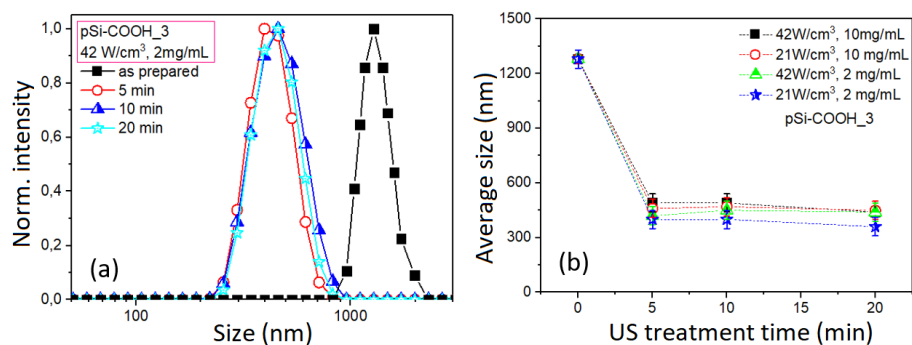


Figure 4.2 DLS results for a representative sample, pSi-COOH₃: size distribution as a function of sonication time for a concentration of 2 mg/mL and 42 W/cm^3 power density (panel a); average size as a function of sonication time obtained for different sample concentrations and US power densities (panel b).

The particle average size reduction is evident. It is furthermore clear that the average size reduction does not depend on the US treatment time: the as-prepared sample is characterized by an average size of about 1300 nm and after undergoing the treatment is reduced to about 500 nm, for any treatment duration. Panel b shows the average size obtained from the DLS size distribution. For any combination of the US parameters, overall decreasing and homogenizing of the average microparticles' size up to about 500 nm can be observed after a few minutes. Although DLS can overestimate the real size, it is more than sufficient for this purpose, since in this preliminary step of optimization we were only interested in evidence of the treatment effectiveness, before proceeding with further experiments.

On the base of the previous results, all the samples have been treated for 10 minutes at 42 W/cm^3 and the obtained size distribution before and after the ultrasonication are reported in Figure 4.3 (The samples after the ultrasonic treatment are labelled as pSi-COOH_1,2,3,4-US) and in Table 4.2.

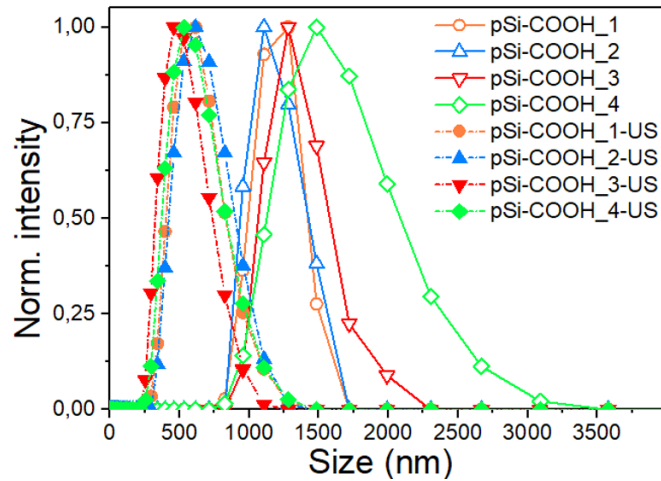


Figure 4.3 Size distribution of different pSi-COOH microparticles by DLS analysis: as-prepared samples (solid lines) and after 10 min sonication at 42 W/cm^3 (dotted lines).

Table 4.2 Average size from DLS analysis, before and after the ultrasonication process (the error is the FWHM of the distribution).

Sample	diameter [nm]	
	As-prepared	After-US
pSi-COOH_1	1200 ± 230	580 ± 210
pSi-COOH_2	1100 ± 250	620 ± 220
pSi-COOH_3	1300 ± 260	480 ± 220
pSi-COOH_4	1500 ± 480	540 ± 230

Figure 4.3 gives evidence of the effectiveness of the treatment of all the samples since the distribution of sonicated samples (dashed lines) shifts towards lower values. For all the samples, the distribution shape with an elongated tail towards the higher dimension is visible and it is typical for samples prepared by a fracturing mechanism, such as sonication. From table 4.2, we can observe an overall reduction of the average size value to about one-half after the treatment (one third for sample pSi-COOH_4). The broadness of the size distribution (parameter which is related to the FWHM) is quite unchanged, except for sample pSi-COOH_4, whose FWHM value halves and becomes comparable with the others. It is to remark, that this procedure also avoids agglomeration of the microparticles, with the main effect of homogenizing the sample.

After having optimized the ultrasonic procedure in terms of sonication time and power density, it is fundamental to check the photoluminescence and morphological properties of the pSi-COOH microparticles to verify if they were affected by the US treatment.

4.3. Optical properties

Steady-state and time-resolved photoluminescence have been employed to evaluate if the optical properties were affected by the US treatment.

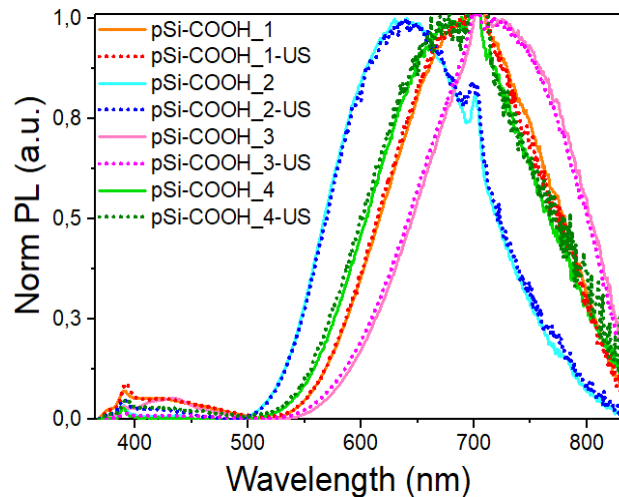


Figure 4.4 US treatment effect on the PL properties: normalized emission spectra (excitation wavelength at 350 nm) of different samples before (solid line) and after 10 min sonication at 42 W/cm^3 (dotted line).

As shown in Figure 4.4, almost no effect on the PL band (and also QY) after the sonication treatment can be found for all the samples (see continuous lines with respect to dotted ones). This is because the sonication treatment does not act on the nanostructures responsible for the optical properties, but has an effect only on the microparticle dimension. Moreover, it has to be highlighted that this treatment is very useful to reduce the dimension of the bigger agglomerated microparticles, having, therefore, a disaggregation effect.

PL decay curves relative to the orange-red band were analysed before and after the US treatment and fitted by an exponential curve to determine the lifetime values. The decay curves relative to the representative sample pSi-COOH_2 are shown in Figure 4.5, before (solid line) and after the treatment (dotted line). The data were recorded by excitation with a pulsed lamp at 325 nm and emission was varied from 600 to 700 nm.

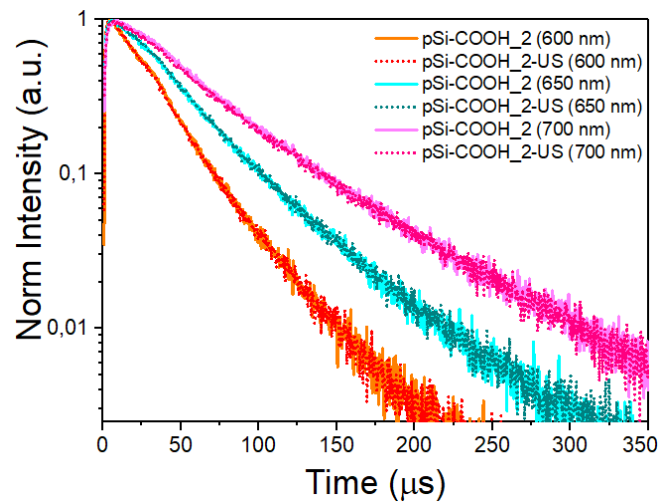


Figure 4.5 PL decay curves of sample pSi-COOH_2 by excitation at 325 nm and emission at 600 nm, λ_{max} (650 nm) and 700 nm, before (solid lines) and after the ultrasonication (dotted lines).

We observe that the decay curves are not affected at all by the US treatment and, as expected, the slope of the curves, which is related to the lifetime value, increases with the emission wavelength (i.e. 600 nm, 650 nm, 700 nm). The lifetime and β values are reported in Table 4.3.

Table 4.3 Lifetime and stretched exponential values are reported to show the dependence on the emission wavelength for sample pSi-COOH_2 as an example.

λ_{em}	As prepared		US-treated	
	τ (μ s)	β	τ (μ s)	β
600 nm	21 ± 1	0.88 ± 0.05	20 ± 1	0.85 ± 0.05
650 nm	29 ± 1	0.85 ± 0.05	30 ± 1	0.86 ± 0.05
700 nm	40 ± 1	0.83 ± 0.05	39 ± 1	0.81 ± 0.05

We verified also that the lifetime relative to the small blue band, whose presence was discussed in Chapter 3, are not affected by the US treatment and are in agreement with the previous findings. This means that the surface of the sample has not been modified, as expected.

4.4. Structural and morphological characterization

The ultrasonicated samples were observed by SEM and TEM for the morphological and structural characterization and compared to the images relative to the as-prepared ones. Here I report few representative images of the observations, that were performed at different magnifications, to obtain hundreds of pSi microparticles samplings for a reliable statistical result (see in the following). Figure 4.6 shows some representative SEM images of the as-prepared and treated pSi-COOH_2 sample, where it is shown that the surface morphology of the material is not affected by the treatment, but an increased number of smaller microparticles in the treated sample can be observed.

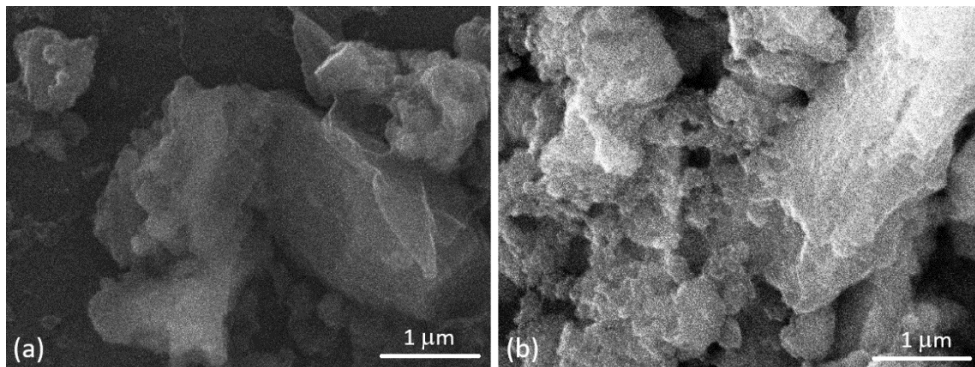


Figure 4.6 SEM images of pSi-COOH_2 (panel a), pSi-COOH_2-US (panel b).

All the samples were also observed by TEM (Figure 4.7), to perform statistical analysis on the microparticles dimension and to compare the results with the ones obtained by DLS analysis.

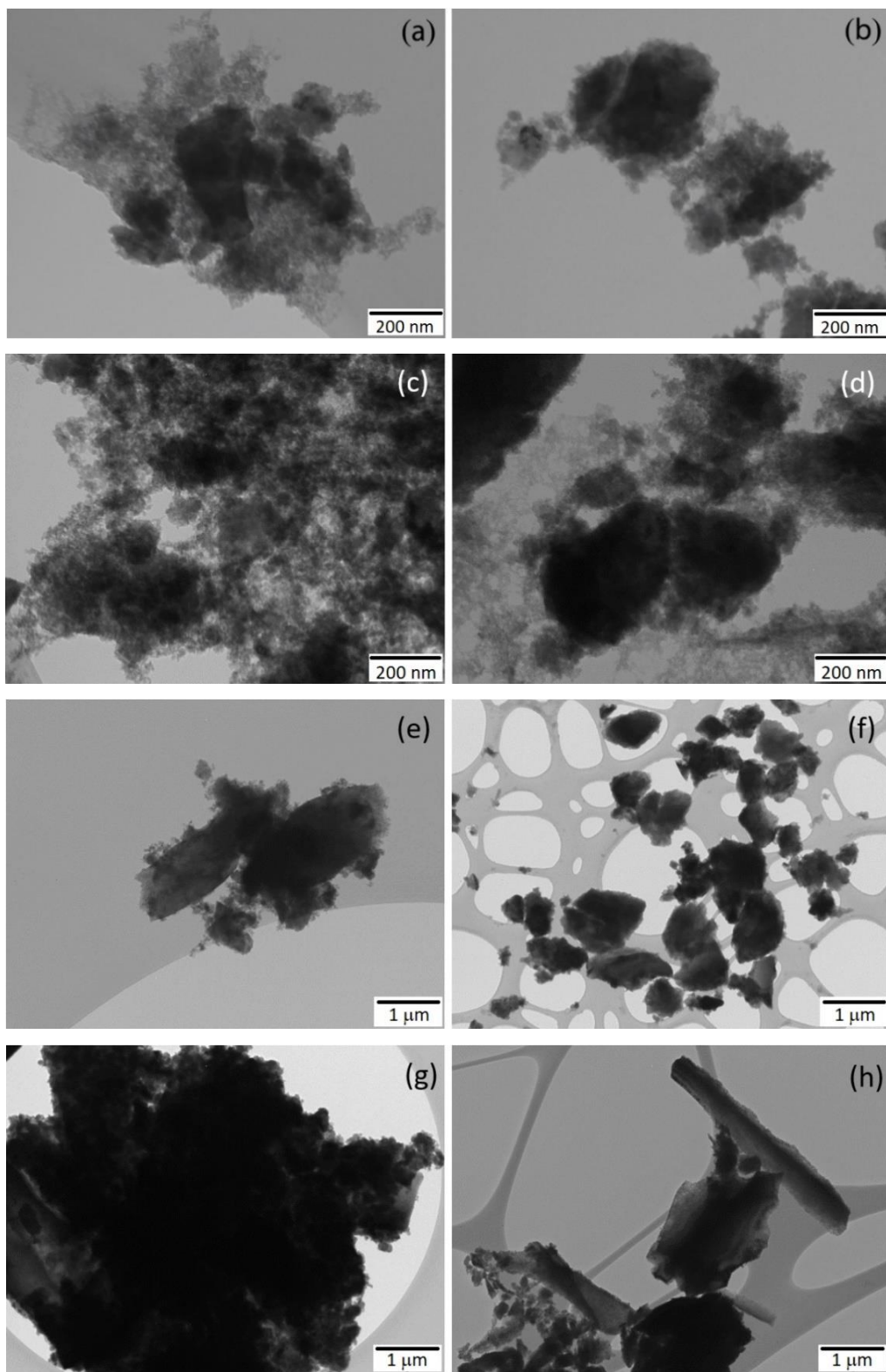


Figure 4.7 TEM images of as-prepared pSi-COOH_{1,2,3,4} (panel a, c, e, g, respectively) and the 10 minutes treated pSi-COOH_{1,2,3,4}-US (panel b, d, f, h, respectively).

In the representative images of Figure 4.7, the morphological structure of the as-prepared samples (panel a, c, e, g) and US-treated samples (panel b, d, f, h) can be seen. The general morphology is not affected by US treatment, whereas the average dimension decreases. In fact, the right panels display smaller microparticles and better distributed in space, if compared to the panels on the left where larger and more agglomerated microparticles can be observed, meaning that the treatment was effecting also in disaggregating the larger microparticles. This can be clearly observed for sample pSi-COOH_3 in panel e and f.

Also, the porosity of the microparticles is not modified by the US treatment. Figure 4.8 shows some representative TEM images where the porosity of sample pSi-COOH_2 can be appreciated before (panel a) and after US treatment (panel b).

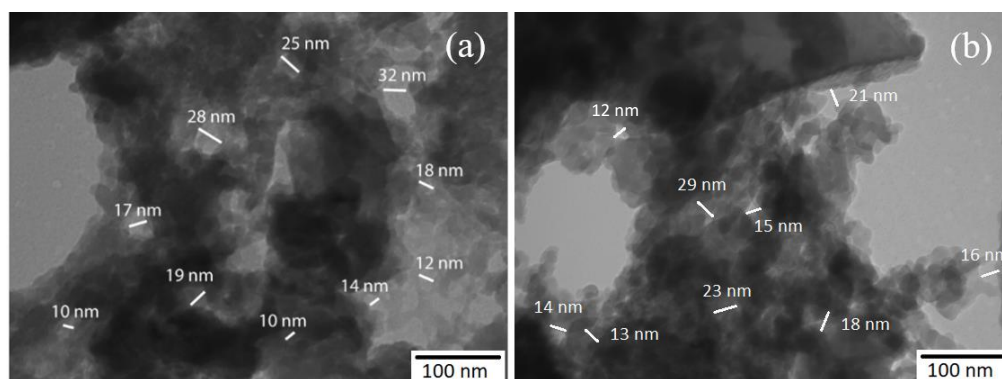


Figure 4.8 TEM images: insight about the porosity of sample pSi-COOH_2-US before (panel a) and after the treatment (panel b), where some pore sizes are pointed out.

For sake of completeness, we performed also EDS analysis (not shown data) and observed that, as obviously clear, the treatment did not affect the material chemical composition and no contamination caused by the US tip is observed.

Even if no quantitative data can be obtained from such a technique, we could do some considerations on the relative “Si” and “O” peak intensities. If the US post-functionalization were effective in fracturing the microparticles, part of the not-COOH-grafted surface should be exposed, leading to an increase of the oxidation and, therefore, of the “O” peak with respect to the “Si” one. Concerning this aspect, and comparing some EDX spectra before and after the US-treatment, no substantial differences can be observed. This indicates that few non-functionalized surfaces are

exposed and therefore, it is probable that this treatment is able to disaggregate the particles rather than fracturing them. This aspect is to be better investigated, for example by means of FTIR spectroscopy and looking for a variation in the Si-O-Si or COOH peaks. On the other hand, we monitored the surface charge after the US treatment, observing no substantial difference in the shape and position of the ζ -potential distribution, which is broad and centred at the same value measured before the treatment. Moreover, we observed no variation in the aspect of the sample after the sonication.

The representative TEM images were analysed to determine the average pSi-micro-particles dimension before and after the ultrasonication and their average pore size. In Figure 4.9, the comparison of pSi microparticles size distribution before and after the ultrasonic treatment is reported while the average sizes for all the samples are reported in Table 4.4 together with an estimation of the average pore size. These values were obtained from TEM images with *ImageJ* software, measuring by hands hundreds of samplings, in a different portion of the sample, deposited on the grid.

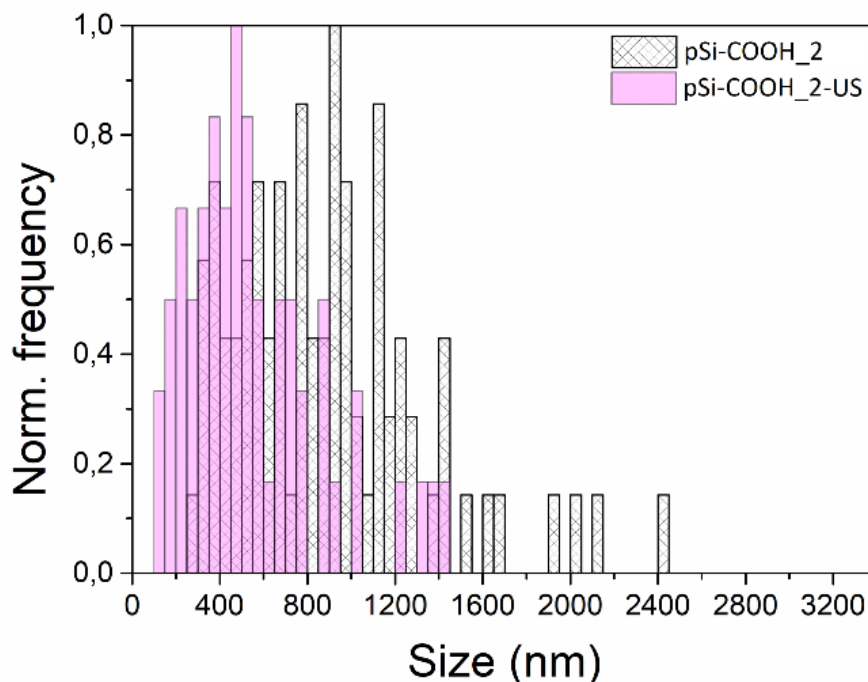


Figure 4.9 Comparison of pSi microparticles size distribution, before and after the ultrasonic treatment determined by TEM, for a representative sample, pSi-COOH₂.

Table 4.4 Pore average sizes of the as-prepared pSi microparticles and after the US treatment obtained by TEM images. The error is the HWHM of the distribution.

Sample	Pore size* [nm]	Microparticles size [nm] as prepared	Microparticles size [nm] sonicated
pSi-COOH_1	16±6	900±470	500±290
pSi-COOH_2	16±5	890±510	550±310
pSi-COOH_3	17±3	730±650	530±280
pSi-COOH_4	5±1	780±630	480±260

* the pore size values before and after sonication were comparable

By comparing the results, it is evident that:

- (i) the pSi microparticles average dimension is considerably reduced after the US treatment, for all the samples
- (ii) the HWHM of the size distribution (related to its wideness) is shrunk by about one-half
- (iii) the pore dimensions are unchanged.

By comparing the results of DLS and TEM, we can observe that the latter analysis leads to smaller values with respect to DLS, as reported in Table 4.4. This difference is observed both before and after the US treatment and it is ascribed to the different sensitivity of the techniques (see Chapter 3). This is added to the fact that DLS is not able to evaluate the agglomeration of microparticles, while by TEM it is possible to distinguish agglomeration or large particles.

The difference in sensitivity of the techniques is also the reason why we are not able to see a shrinking of the size distribution by DLS, differently from TEM.

It is however clear that the microparticles average size is reduced, the results obtained by DLS and TEM for the treated microparticles are very similar and the sample results homogenized in both data analyses.

Therefore, both DLS and TEM results attest that the ultrasonication is an easy and rapid way to reduce the size from a few microns to hundreds of nm.

4.5. Conclusions

Here, we developed a post-functionalization dispersing technology, based on sonochemical effects:

- This treatment is excellent in homogenizing the size of the microparticles and in decreasing the average dimension by fracturing the large microparticles and by, most probably, disaggregating the grouped ones. With respect to other methods of size homogenization, e.g. filtration, the advantage of this procedure is to avoid wasting material, since all the produced microparticles are treated with the US to reduce the average size. This is particularly important since the electrochemical etching used to produce the pSi microparticles allow to obtain just some milligrams and therefore, it is important to save the more material as possible
- We found that the ultrasonic treatment affects neither the porosity nor the surface carboxyl-functionalization, which was indirectly proved by the conservation of the optical properties
- We reported that this US treatment is effective for samples with different size distributions.

In conclusion, we reported that an easy post-functionalization procedure of US treatment for a few minutes could solve the problem related to the top-down fabrication approach, i.e. is the heterogeneity of the sample size. This is a small achieved step that is fundamental to consolidate the possibility to apply this material in the biomedical field.

CHAPTER 5

INORGANIC COATING OF pSi MICROPARTICLES

As reviewed in Chapters 1 and 2, porous silicon holds good chances to be used as theranostic agent, due to its peculiar properties, i.e. porosity and intrinsic photoluminescence, thus being a drug carrier traceable in-vitro and in-vivo. One of the main limits is the PL quenching and also the structural degradation of the pSi microparticles in an aqueous or biological environment.

In this chapter, we report about a new solution to this issue: the pSi microparticles inorganic (titanium dioxide) coating by ALD (Atomic Layer Deposition), which allows obtaining a complete and uniform thin coating with fine-tuning of the layer thickness. The optimization of the ALD parameters is performed and the optical emission properties of pSi-TiO₂ microparticles are stabilized for several months without affecting the other structural properties, giving good chances to this material to be a promising tool for theranostics.

The topic of this chapter is briefly summarized in the table:

<i>Problem</i>		<i>State of the art solution</i>		<i>New solution</i>
<i>PL stabilization in biological media</i>	→	<i>Organic coating (PEG and chitosan)</i>	→	<i>Inorganic coating (TiO₂ by ALD)</i>

As previously anticipated, one of the main issues to use the light-emitting pSi microparticles for biomedical imaging is the fast quenching of photoluminescence in aqueous environments. In fact, the PL is maintained for years in ethanol, but the material has to be resuspended in a biological medium (i.e. phosphate-buffered saline – PBS, pH 7.4) before in-vitro tests.

When the microparticles are stored in aqueous solution, the PL quenching is caused by oxidation of the surface of the microparticles and thus, the characteristic orange-red band shifts towards lower wavelengths and decreases in intensity, until it disappears,¹⁰³ with a PL half-life time of about 5 h at pH 7.4.¹⁴⁰

Several attempts to solve the PL degradation issue have been proposed essentially

following two different approaches:

- (i) **controlled surface oxidation**
- (ii) **organic coatings**

In the first approach, the pSi microparticles are treated with thermal oxidation or with SiO₂ coating, leading to an optical stabilization in aqueous solutions of the pSi microparticles for hours.¹⁴¹ The pSi was further made reacted with borax and thus the photoluminescence was stabilized for a longer time¹⁴² and then up to five days by rapid thermal oxidation.¹⁴³

In the latter approach, the protection of the material surface with polymers preserve also the luminescence properties. For this reason, several solutions have been proposed in the literature¹⁴⁴ a PEGylation, i.e. the attachment of PEG (polyethylene glycol) onto the pSi surface, was firstly performed in order to better tune the pSi kinetics of degradation of pSi to be used as DDS (drug delivery system).¹⁴⁵ In the biomedical field, PEG is one of the most used polymers, because it is biodegradable and reduces opsonization effect in-vivo, but other natural polymers are investigated,¹⁴⁶ for instance proteins (silk,¹⁴⁷ collagen,¹⁴⁸ albumin¹⁴⁹) and polysaccharides (chitosan,¹⁵⁰ alginate¹⁵¹) to produce biocompatible polymer-based nanoparticles. Our attempt to solve the degradation of pSi microparticles in aqueous media consisted of both organic and inorganic coating

State of the art solution: organic coating (PEG and chitosan)

Along the direction of PEGylation, we already proved the possibility to coat our pSi microparticles by covalent attachment of organic coating, i.e. PEG and chitosan, bearing carboxyl groups (negatively charged) and amine groups (positively charged) on the external surface, respectively.⁸⁹ The coating protocol has been developed in collaboration with the group of Prof. M. Comes Franchini (Dept. of Industrial Chemistry, University of Bologna). Both PEG and chitosan allowed to stabilize the PL till three months: pSi-PEG PL showed a small blue shift that increased as a function of the coating thickness; pSi-chitosan degraded faster than pSi-PEG and showed a more intense shift of the orange-red band and the appearance of the blue band, whose intensity increased with time.

PEG and chitosan-coated samples were tested as a drug delivery carrier with cobalamin (Cbi – vitamin B2 precursor) as a test drug. Firstly, the chemistry and structure of the drug were proved not to be modified by the interaction with porous silicon, secondly, it was found that Cbi could be loaded into the pores, a higher amount for negatively charged microparticles, for which the release happened with a very slow rate.⁸⁹ The possibility to use pSi microparticles as carriers is also evaluated in Chapter 7, where the delivery of immune agonists is investigated, in perspective of immunotherapy. However, this coating procedure caused an increase in the average size of the microparticles and/or a filling of the pores, because of the polymer thickness. Then, the space available for drug loading is strongly affected, thus limiting the use of pSi microparticles as carriers in biomedical applications.

Second solution: inorganic coating (TiO₂ deposition by ALD)

A further attempt was performed to stabilize the PL properties of the pSi microparticles, minimize the reduction of the pore volume. We explored a method to cover the porous surface of the microparticles with a thin layer of titanium dioxide. In Figure 5.1, the different approaches used to coat the pSi microparticles and preserve the PL emission properties are reported.

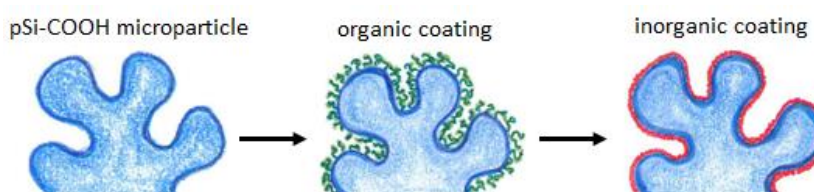


Figure 5.1 Sketch of the different coating approaches to preserve the PL emission properties of the pSi microparticles.

5.1. Atomic Layer Deposition of TiO₂

The deposition technique explored is an innovative method to coat the pSi-COOH microparticles with a thin layer of titanium dioxide by means of ALD (atomic layer deposition) in a rotary reactor,^{152,153} thus producing pSi-TiO₂ microparticles. ALD is composed of several steps as sketched in Figure 5.2, where a figurative pore is considered. During the procedure, both a precursor and vapour or reactant gases are pumped into the chamber.¹⁵⁴ The first precursor in the vapour phase is pumped inside the chamber, where it reacts with the heated material surface in a self-limited

way. The molecules that have not reacted with the surface, or the by-products of the reaction, are purged out by pumping an inert gas. This procedure is repeated analogously with the reactant gas to obtain the first layer. The repetition of this cycle several times allows to obtain a uniform coating and to increase its thickness, until the desired value.¹⁵⁵ In this particular case, to obtain a TiO₂ layer, we used the precursor TDMAT (Tetrakis – dimethylamino – titanium) and H₂O as the reactant gas.

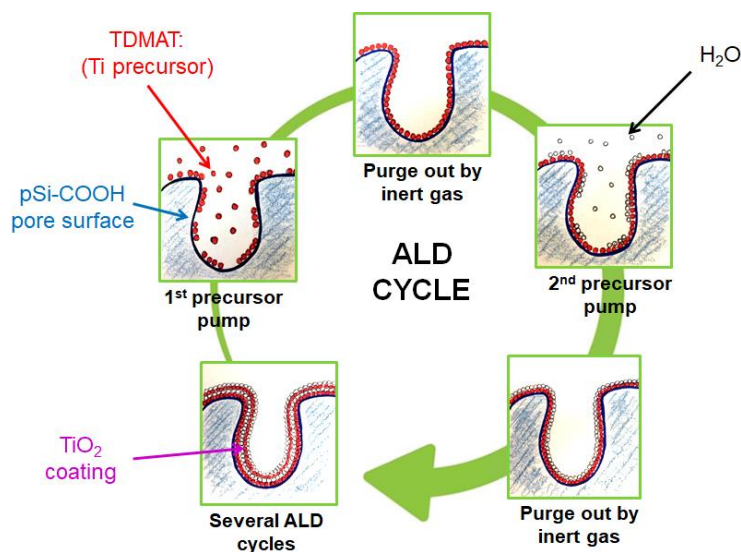


Figure 5.2 Sketch of the steps composing the ALD cycles of TiO₂ on a figurative silicon pore.

This technique was previously used to microencapsulate the moisture-sensitive CaS:Eu⁺ microparticles.¹⁵⁶ In the case of porous silicon, it was not already applied to microparticles, but to a flat substrate,¹⁵⁷ while the rotary reactor allows reaching every portion of the porous microparticle.

In this chapter, the effect on the PL stability as a function of the deposition parameters is reported and discussed. The main ALD parameters are the time of the precursors (TDMAT and water) pumping, the time of removal by inert gas and the number of deposition cycles, which is related to the final thickness of the deposited layer.

TiO₂ coating was performed on pSi-COOH microparticles fabricated by electrochemical etching of boron-doped p-type Si wafers and functionalized with acrylic acid, as described in Chapter 3. The sample coating was performed and optimized by the group of Prof. C. Detavernier (Department of Solid State Sciences, CoCooN

Group, Ghent University). The deposition was done with a rotary pump-type reactor operating at a base 10^{-5} mbar pressure. The temperature during the process was 100° C and the partial pressures of the precursors were 5×10^{-4} mbar, for TDMAT and 2×10^{-3} mbar, for water.

The coating procedure was optimized, by varying the deposition parameters. The produced samples, with the relative ALD process times and the number of cycles, are reported in Table 5.1.

Table 5.1 ALD process times for pSi-COOH sample coating.

Sample	TDMAT (s) ^{a)}	Pump (s) ^{b)}	H₂O (s) ^{c)}	Pump (s) ^{b)}	n° cycles ^{d)}
A1 (pSi-TiO ₂)	120	80	120	80	30
A2 (pSi-TiO ₂)	300	600	300	600	30
B1 (pSi-TiO ₂)	120	80	60	60	30
B2 (pSi-TiO ₂)	120	80	120	100	20

^{a)} Exposure time of Ti precursor (TDMAT) into the chamber; ^{b)} time to remove excess precursors and by-products; ^{c)} H₂O exposure time; ^{d)} number of ALD cycles.

The optimization of the deposition procedure was performed by focusing on the effect of the precursor's exposure times to preserve the PL emission properties. Firstly, samples A1 and A2 were prepared under short (120 s) and long (300 s) exposure times, respectively. Only the short treatment (sample A1) allows keeping the photoluminescence of the sample, while under long treatment (sample A2) the PL band quickly disappears, as it reported in the following. Then, TDMAT parameters were fixed and we explored the effect of water in samples B1 and B2, by varying the exposure time to water (60 s and 120 s, respectively).

The produced powders were dispersed at a concentration of 1 mg/mL in PBS (phosphate-buffered saline), which simulates the biological fluids, and is stored at room temperature.

5.2. TiO₂ coated luminescent pSi microparticles

To find the optimal deposition parameters set, the pSi-TiO₂ samples were investigated to study their effect on structural, chemical and optical properties.

Structure, morphology and chemical analysis were investigated by TEM/EDS, for the morphological and elemental composition characterization, by DLS to determine the average size and the surface charge, by FTIR spectroscopy to determine the surface chemical groups. The presence of crystalline phases was evaluated by XRD and Raman spectroscopy and the optical characterization was performed by fluorescence spectroscopy.

The instrumentation used and the relative obtained information are reported in Table 5.2. The details of instrumentation and measurement procedure, used for structural and optical characterization, are reported in Appendix A1.

Table 5.2 Characterization techniques and related information

Characterization	Technique	Measurement information
Surface	FTIR Spectroscopy	Surface chemical groups
	DLS	ζ -potential
Optical	Fluorescence spectroscopy	Photoluminescence, Lifetimes, Quantum Yield
Structural	DLS	Average dimension
	TEM/EDS	Morphology, dimension, porosity

5.2.1. Structural, surface and chemical characterization

The optimized B1 and B2 pSi-TiO₂ samples were investigated by EDS to analyse their elemental composition. The spectra are reported in Figure 5.3.

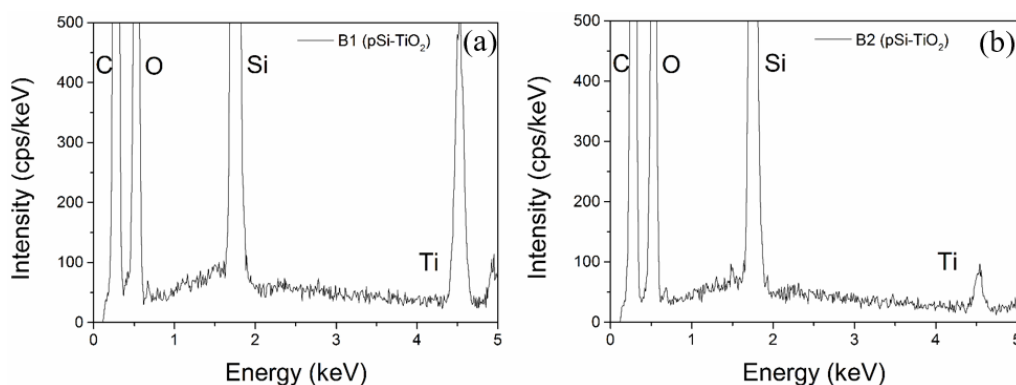


Figure 5.3 EDS spectra of pSi-TiO₂ microparticles: samples B1 (panel a) and B2 (panel b).

In both EDS spectra, the peaks relative to Si, C, O and Ti can be clearly observed. While the formers are relative to pSi microparticles functionalized with acrylic acid, (see EDS spectra of Figure 3.8 in Chapter 3 the presence of the Ti peak in both the samples shows that the titanium dioxide deposition was successful. Although EDS technique is not appropriate for quantitative analysis of thickness and homogeneity of the deposited inorganic layer, we can presume that the lower intensity of Ti peak in sample B2 (panel b) indicates a thinner deposited layer, in agreement to the lower deposition cycles number.

The morphology of the pSi-TiO₂ samples after the deposition was investigated by TEM: images are reported in Figure 5.4 for a representative sample on different scales.

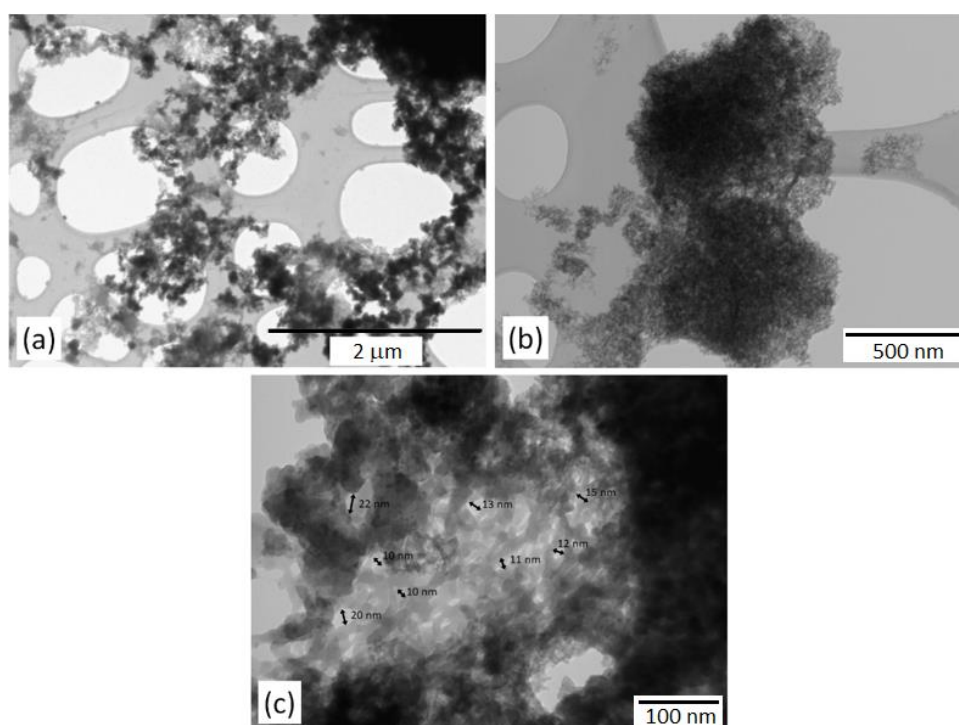


Figure 5.4 TEM images of sample B2 (pSi-TiO₂ microparticles) in PBS at different scales: 2 μ m (panel a), 500 nm (panel b) and 100 nm (panel c), where some pore sizes are pointed out.

From the image analysis and the comparison with the TEM images of the uncoated sample in Chapter 3 and 4, we can conclude that the microparticles size and the porous structure are not modified by the ALD process. In Figure 5.4 (panel a and b) we can observe coated microparticles with a dimension varying from few microns to hundreds of nm and Figure 5.4 (c) shows that the porosity is maintained

with a pore size of about 10–20 nm. Other groups reported a gradual and then complete filling of the porous structure after several ALD cycles.^{158,159} Differently, we did not observe any substantial shrinking of the pores (13% or 25% of reduction in the case of a 22 nm or 12 nm pore, respectively), probably thanks to the ALD optimization performed in terms of precursor times that allowed to achieve a TiO₂ coating with a small number of deposition cycles. This is also due to the fact that based on previous studies,¹⁶⁰ the expected thickness of the TiO₂ coating is about 1.5 nm, which is much smaller with respect to the dimension of the pores.

The surface chemistry of the coated pSi microparticles was investigated by FTIR spectroscopy (Figure 5.5).

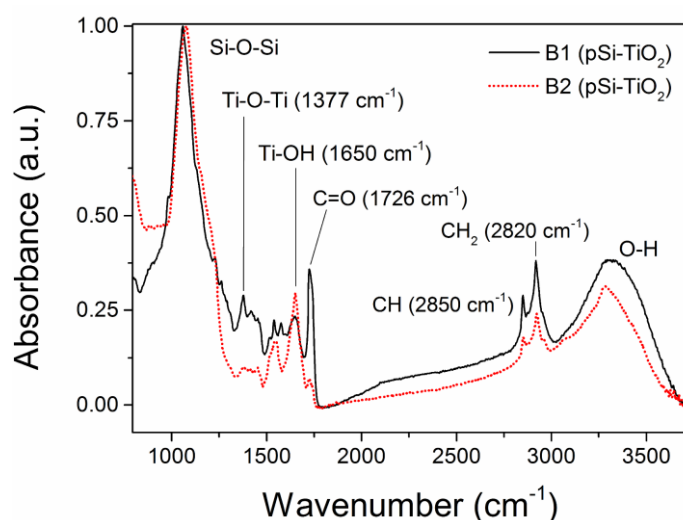


Figure 5.5 FTIR spectra of pSi–TiO₂ microparticles: samples B1 (straight line) and B2 (dotted line).

The characteristic pSi-COOH peaks can be observed: the O-H stretching band relative to water at about 3300 cm⁻¹, the CH and CH₂ stretching peaks at 2850 cm⁻¹ and 2920 cm⁻¹; the Si–O–Si band, at 1060 cm⁻¹ for sample B1 and at 1080 cm⁻¹ for sample B2. The 20 cm⁻¹ difference of the peak position between the two samples could be related to the higher oxidation of sample B2, which was exposed to water for a longer time inducing a shift of the peak towards larger wavenumbers. This is in agreement with the results on SiO_x films produced by plasma-enhanced chemical vapour deposition.¹⁶¹

The presence of the TiO₂ deposited layer is demonstrated by the Ti-O-Ti peak at 1377 cm⁻¹ and the peak at 1650 cm⁻¹ related to the bending of Ti–OH group.¹⁶²

Furthermore, we can observe that the relative peaks intensity is qualitatively consistent with the amount of deposited layer, related to the number of deposition cycles, and with the previous results of the EDS analysis. The Ti-OH peak of sample B2 is higher than Ti-O-Ti peak because it has a higher amount of water due to the longer exposure during the ALD process.

Moreover, we can observe that the peak relative to the COOH group at 1726 cm^{-1} is still present after the TiO_2 deposition, meaning that the process was not affecting the microparticles functionalization, as confirmed by ζ -potential measurements. It could be surprising to observe the presence of COOH groups after the inorganic coating. From one side, the carboxyl groups signal can be detected by FT-IR spectroscopy, since this technique allows to obtain information not only from the surface but also under the TiO_2 coating. On the other side, DLS should only measure the surface of the material, but we can still detect a negative charge. We are not able to explain well the variation in surface charge after the TiO_2 deposition, yet. Anyway, a first plausible explanation is that the organic nanolayer is not uniformly deposited on the porous Si surface, considering its very thin thickness (1 to 2 nm). In this way, some of the COOH groups could be exposed to water also after the inorganic coating. Secondly, it may be considered that the laser used to perform DLS measurements (633 nm) could penetrate the thin inorganic layer, thus being able to detect the negative charges under the coating. Last, we think to be possible that some of the TiO_x bound to the COOH groups are present with $x < 2$, thus having a partial negative charge. The results of DLS measurements are reported in Table 5.3, where the average size and the surface charge (i.e. the ζ -potential) of the pSi microparticles are shown. As discussed in the previous chapter, microparticles surface charge and dimension have a fundamental role in the interaction with the cells and could affect their uptake. The ζ -potential passes from -30 mV before the coating (result in agreement with the previous for pSi-COOH microparticles)¹⁴⁰ to about -20 mV after the TiO_2 deposition, at pH 7.4, meaning that the carboxylic groups are still present on the porous surface, but without affecting the optical properties, see in the next paragraph. Furthermore, the presence of the COOH groups gives the possibility to further conjugations, such as folic acid, for the application of this material as

targeted drug delivery carrier, as it was demonstrated with Cbi (cobinamide – the precursor of B2 vitamin) as a test drug.¹⁴⁰

Table 5.3 DLS characterization of pSi microparticles. Size and ζ -potential values of pSi-TiO₂ microparticles (sample B1 and B2) and pSi-COOH microparticles (sample Ref) suspended in PBS (pH 7.4).

Sample	Size (nm)	ζ -potential (mV)
Ref (pSi-COOH)	200±50	-29±2
B1 (pSi-TiO ₂)	300±50	-19±1
B2 (pSi-TiO ₂)	250±50	-19±4

The values obtained by DLS show a quite broad size distribution for all the samples, with an FWHM of about 100 nm. The average size passes from 200 nm of the Ref sample to 300 nm for sample B1 and 250 nm for sample B2. This difference could be due to the different oxidation between samples B1 and B2 and related to the different water exposures times.

The presence of crystalline phases related to deposition mechanism was investigated by XRD and Raman spectroscopy since this could affect the properties of the material and its biocompatibility.¹⁶³ Both the techniques are, in fact, sensitive to the presence of the TiO₂ phases, which are anatase, rutile and brookite. Differently from XRD, which measures the orientation and the order of the atoms, Raman spectroscopy gives indirect information related to the vibrational properties of the sample under investigation.

pSi-TiO₂ samples were investigated and XRD (panel a) and Raman (panel b) spectra are reported in Figure 5.6 for sample B1, as a representative sample.

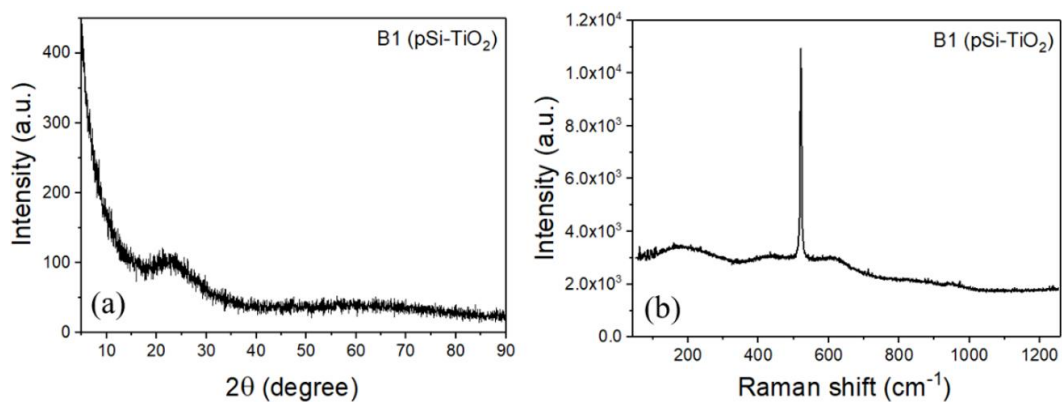


Figure 5.6 XRD spectrum (panel a) and Raman spectrum by 514 nm excitation (panel b) of sample B1.

No peaks ascribable to the crystalline phase of titanium dioxide can be observed in the XRD and spectra relative to B1 sample, if compared to the reference spectra JCPDS number 21-1272 (anatase) and 21-1276 (rutile), and similar results were obtained for sample B2. Only a broad band at about 22° can be related to amorphous structure.

In Figure 5.6(a), the peak at 520 cm^{-1} and the broad band around 200 cm^{-1} are related to the silicon core, but no peaks are ascribable to any TiO_2 crystalline phase.¹⁶⁴ It is also to be noted that the TiO_2 layer is very thin and therefore very difficult to be detected, particularly for Raman spectroscopy.

From the absence of any peaks related to crystalline structure and that the deposition was performed without aiming at crystalline structure formation, we could conclude that the deposited TiO_2 is amorphous.

5.2.2. Optical properties

Photoluminescence. The optical properties were investigated by a spectrofluorometer and the PL spectra of the pSi-TiO₂ samples dispersed in PBS are reported in Figure 5.7.

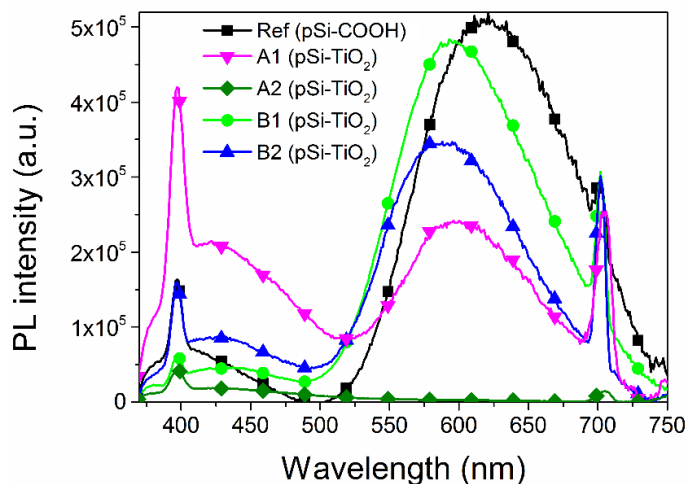


Figure 5.7 PL spectra under 350 nm excitation of pSi-TiO₂ microparticles after the resuspension in PBS. The PL of the reference sample (pSi-COOH) is reported.

Apart from sample A2, all the samples maintain the photoluminescence after the ALD process. It is worth noting that the sharp peak at 390 nm, present for all the spectra, is due to the Raman effect of the aqueous solution.¹³⁰ All the samples are

characterized by a blue shift of the orange-red band with respect to the uncoated pSi-COOH samples, with a maximum value of 30 nm for sample B2.

The determined maximum emission wavelengths are reported in Table 5.4 together with the optical quantum yields.

Table 5.4 Optical quantum yields (obtained by comparative method) and maximum emission wavelength.

Sample	QY (%)	λ_{\max} (nm)
Ref (pSi-COOH)	0.8	620
A1 (pSi-TiO ₂)	0.7	597
A2 (pSi-TiO ₂)	-	-
B1 (pSi-TiO ₂)	0.9	595
B2 (pSi-TiO ₂)	0.5	590

The blue shift with respect to the Ref sample could be related to water exposure and the relative sample oxidation, which causes a reduction in the size of the light-emitting nanostructures. The PL is totally quenched for sample A2, which was exposed to H₂O for the longest time (300 s) suggesting that complete oxidation of the light-emitting Si nanostructures occurred.¹⁰³ Concerning sample B1 and B2, we can observe that the small PL shift towards shorter wavelengths (from 620 nm to about 595 nm) is well consistent with the water exposure times.

Quantum yield (QY). The QY reported in Table 5.4 were determined by comparative method, with pSi-COOH microparticles (Ref sample in ethanol) as the reference sample. The slopes in Figure 5.8 were obtained by linear fitting of the data, i.e. the integrated PL as a function of the absorbance (i.e. the concentration of the sample), and were used to calculate the quantum yields.

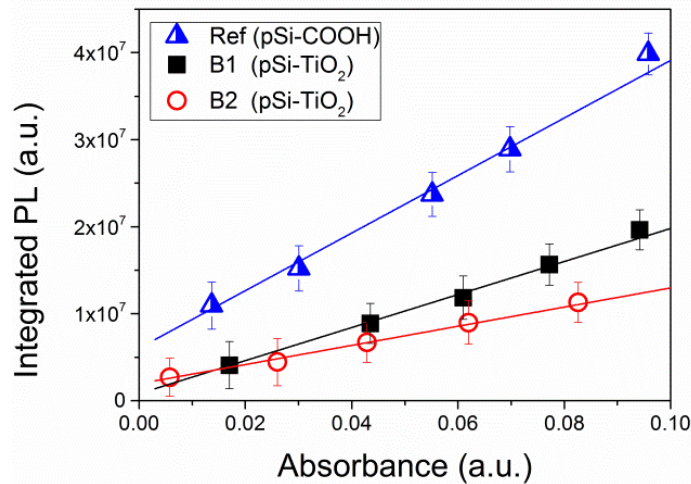


Figure 5.8 Comparative method for QY determination. Integrated PL of the reference sample (pSi-COOH) in ethanol and pSi-TiO₂ microparticles (sample B1 and B2) in PBS as a function of the optical absorbance.

pSi-COOH microparticles, whose QY (1.7%) was previously determined in ethanol with respect to Rhodamine 101 and Fluorescein,⁸⁸ were used as standard.

The QY values obtained after the coating are reduced (0.7%, 0.9% and 0.5%, for sample A1, B1 and B2), this reduction is compatible with a partial oxidation that the material could undergo during the deposition process, but it is not a dramatic variation and similar values were previously obtained for pSi microparticles coated with organic PEG and chitosan (0.9 % and 0.7%, respectively).⁸⁹

Lifetime. Time-resolved PL has been performed to verify if the coating deposition was affecting the recombination mechanism and the lifetime of the pSi microparticles. The decay curves of pSi microparticles (sample B1 and B2) are reported in Figure 5.9, compared to the uncoated sample and fitted by a stretching exponential to determine the emission lifetime τ and the stretching parameter β (Table 5.7).

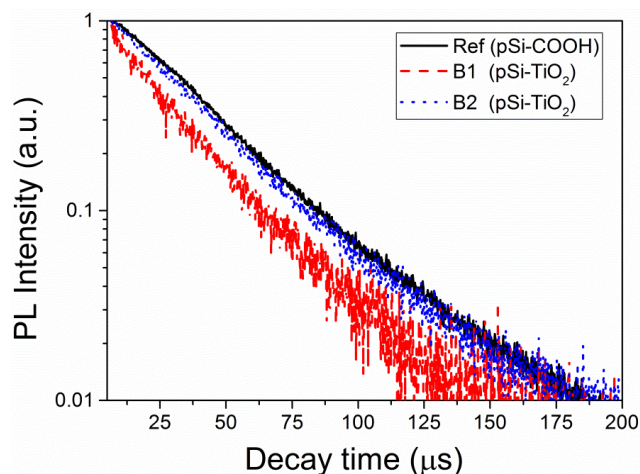


Figure 5.9 PL decay curve of pSi-COOH (Ref sample) and pSi-TiO₂ microparticles (B1 and B2 samples) by excitation at 350 nm and looking at λ_{max} .

Table 5.5 Lifetime τ and stretched parameter β of pSi-COOH microparticles (Ref sample) and pSi-TiO₂ microparticles (B1 and B2 samples) by excitation at 350 nm and emission at λ_{max} of the PL emission spectrum.

Sample	Lifetime (μ s)	β
Ref (pSi-COOH)	20 \pm 3	0.74 \pm 0.05
B1 (pSi-TiO ₂)	25 \pm 2	0.83 \pm 0.05
B2 (pSi-TiO ₂)	26 \pm 2	0.88 \pm 0.05

The obtained lifetime values (about 25 μ s) and the stretching parameter (about 0.8) are compatible with previous findings for pSi-COOH microparticles, suggesting that the coating doesn't influence at all the optical emission characteristics of the pSi microparticles.

The efficacy of the TiO₂ coating in stabilizing the luminescence properties of the light-emitting pSi in aqueous media was assessed by monitoring the PL band as a function of time (three months reported). The normalized PL intensity of B1 and B2 samples shown in Figure 5.10 indicates that the PL band is constant as the time increases.

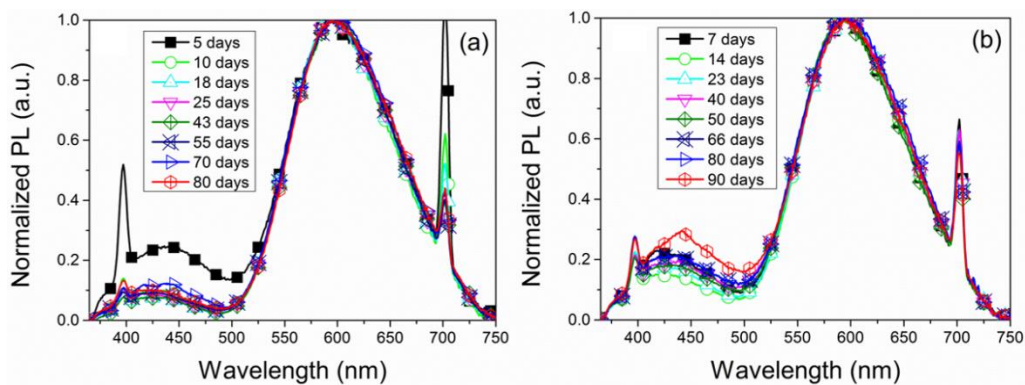


Figure 5.10 Monitoring of the PL band of pSi-TiO₂ microparticles (B1(a) and B2 (b) samples) in PBS as a function of time (i.e. ageing), normalized with respect to the maximum.

Figure 5.11 reports the integrated PL band of sample B1 and B2 as a function of the ageing of the sample compared to the Reference sample fast quenching.

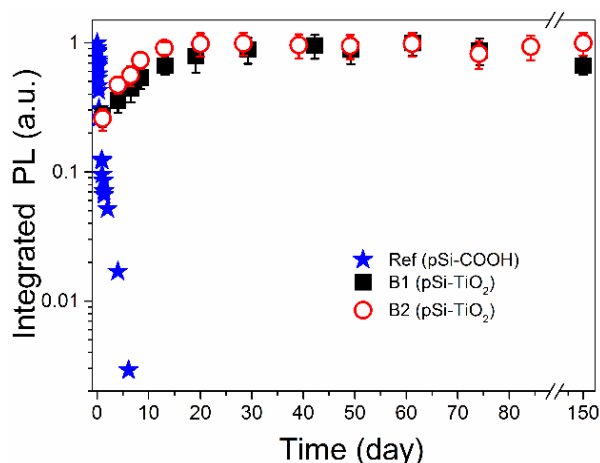


Figure 5.11 Monitoring the integrated normalized orange-red band of pSi-TiO₂ microparticles (B1 and B2) as a function of time, in PBS, compared with pSi-COOH.

The values are normalized with respect to the optical absorbance at 350 nm and ‘day 0’ refers to the moment in which the powder sample was resuspended in aqueous media (i.e. PBS). For the uncoated sample, a fast decreasing of the photoluminescence is observed, which disappears after a few days. For the TiO₂ coated samples, we can observe a little increase in the integrated PL in the first days for both samples reaching stability in optical emission for more than five months

The initial PL increase was similarly found from another group,¹⁶⁵ studying the coating with bio-resorbable polymers of light-emitting nanoparticles, whose PL increased in the first two weeks and then reached a stabilization. The initial increase

was ascribed to the passivation of the dangling bonds by gas-phase water molecules. This could be in principle what happened to our material after the TiO₂ deposition.

5.3. Conclusions

In this chapter, we reported for the first time the possibility to obtain pSi-COOH microparticles PL stability in biological media by means of inorganic TiO₂ coating. We used an innovative method (ALD) of deposition that allows a uniform thin layer formation with tuneable thickness, which was effective in prolonging the luminescence stability in aqueous media up to several months, with results similar to organic coatings (e.g. PEG and Chitosan), which represent the state of the art. Moreover, we proved the ALD technique to be able to produce a tailored inorganic coating of pSi microparticles with an easy and tuneable process.

In particular, we observed and proved:

- no structural or morphological change, i.e. no modification of the average size and porosity
- still negative surface charge
- a small blue shift of the PL band, already observed for organic coating, due to a partial oxidation
- no variation in lifetime
- a reduction of the QY from 1.5 to about 1%, already observed for organic coating
- a PL stabilization for 5 months.

This opens the way for further developments, to coat the pSi microparticles with a thin layer of different oxides, such as iron (magnetic properties), rare earth metals (magnetic and optical properties) and zinc (antibacterial properties), for the addition of other functionalities to pSi microparticles.

These encouraging results are another fundamental step achieved to consider pSi-TiO₂ microparticles as a promising material for theranostics.

CHAPTER 6

IN-VITRO STUDY: INTERACTION WITH HUMAN IMMUNE CELLS

In previous chapters, we proved that a simple post-functionalization procedure is sufficient to reduce the average size of pSi microparticles, to homogenize the sample (Chapter 4) and to stabilize the optical emission and structural properties also in aqueous environment by an inorganic coating (Chapter 5). Here, we present a further needed step for the exploitability of the fabricated pSi in theranostics that is the evaluation of cytotoxicity and immunogenicity. In this perspective, the interaction of the pSi microparticles, with and without the inorganic coating, with the cells of the immune system is evaluated. A limitation of the use of inorganic materials for biomedical application is their possible capacity to stimulate immune cells, such as dendritic cells, having the role of presenting the pathogen antigens to the lymphocytes and triggering the immune response by release of molecules, called cytokines. Thus, it is fundamental that nanomaterials do not exert toxic effects on DCs and do not activate these cells, as well as other cells belonging to the immune system activation. Besides these aspects, we investigate the ability of the inorganic coating to stabilize the PL emission properties also inside the cells to evaluate the applicability of this system for optical imaging.

6.1. Immune system and dendritic cells

The immune system is a complex network of cells, biological structures and molecules that are devoted to defending the organism from pathogens. It is composed of innate immunity (quick and aspecific response) and adaptive immunity (slower but specific response). The immune cells (lymphocytes and antigen-presenting cells, APC) are involved in the coordination of inflammatory and immune responses.¹⁶⁶ They react by releasing the cytokines, which are crucial molecules in regulating the inflammatory and immune response and which induce immune cells to produce oxygen free radicals (O_2^+) that can cause oxidative damages to the cells. Among the

APCs, monocytes and macrophages have the role of engulfing, lysing cancer or infected cells.¹⁶⁷ Dendritic cells (DCs) are messengers between innate and adaptive immune systems, since they monitor the environment, detect the antigens (molecules recognized as foreign or dangerous) and trigger lymphocytes proliferation and activation. The name derives from their morphology: they have long and spiky arms, the dendrites (visible around the cells in Figure 6.1 (a)), to move and to capture the antigens. In the immature state, DCs have high capacity to bind and engulf the antigens and to release cytokines for the communication with the other immune cells. After their maturation, caused by several external stimuli and molecules (i.e. inflammatory mediators), they change in shape (elongation and increase of the dendrites, see Figure 6.1 (b)) and are able to activate the lymphocytes.¹⁶⁸

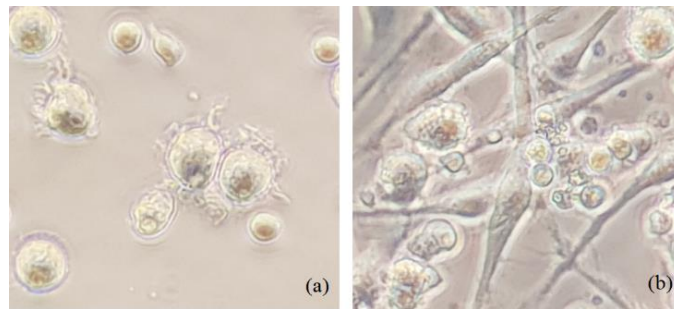


Figure 6.1 Optical image of Dendritic cells (DCs) before (panel a) and after the stimulation and maturation (panel b).

In general, the foreign materials internalization by cells is regulated by endocytosis: receptor-mediated endocytosis, phagocytosis and aspecific pinocytosis (engulfment of liquids), which are schematized in Figure 6.2.

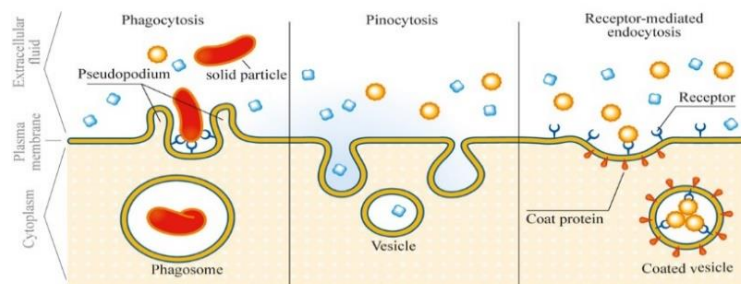


Figure 6.2 Foreign materials internalization by cells is regulated by endocytosis: receptor-mediated endocytosis, phagocytosis and aspecific pinocytosis.¹⁶⁹

In particular, DCs can internalize foreign antigens, both soluble or solids, by phagocytosis, which is stimulated by the binding of specific receptors present on the DC membrane, such Toll-like receptors (TLRs). Both of them induce up-regulation of co-stimulatory molecules and inflammation responses.

Due to the scarce presence and the difficulty to isolate blood DCs, some protocols were established to generate DCs from precursor cells. The most used protocol involves the stimulation of human blood monocytes with specific cytokines (in particular IL-4 (interleukin 4), to induce their differentiation into DCs.¹⁷⁰ For the in-vitro tests reported in the following paragraphs, to evaluate biocompatibility and immunogenicity of porous silicon microparticles, we used monocytes-derived DC. They are produced in 5 days, by stimulating human blood monocytes with GM-CSF growth factor and IL-4.

6.1.1. Interaction of DCs with nanoparticles

As it was reported in Chapter 1, nanoparticles are characterized by at least one nm dimension and show different properties with respect to the bulk material. Since DCs are antigen-presenting cells, their interaction with NPs, used to carry and protect antigens, could be very interesting in perspective of immune response improvement, for example in vaccines, cancer or immune therapies. The use of antigen-loaded NPs can also be useful to reduce the side effects of vaccination or cancer treatments. The antigens can be encapsulated in NPs or conjugated to their surface to be presented to the DCs. Labelled NPs can also be tracked inside the cells to verify their uptake by the cells. Figure 6.3 shows the ways NPs could interact with dendritic cells and the related application.

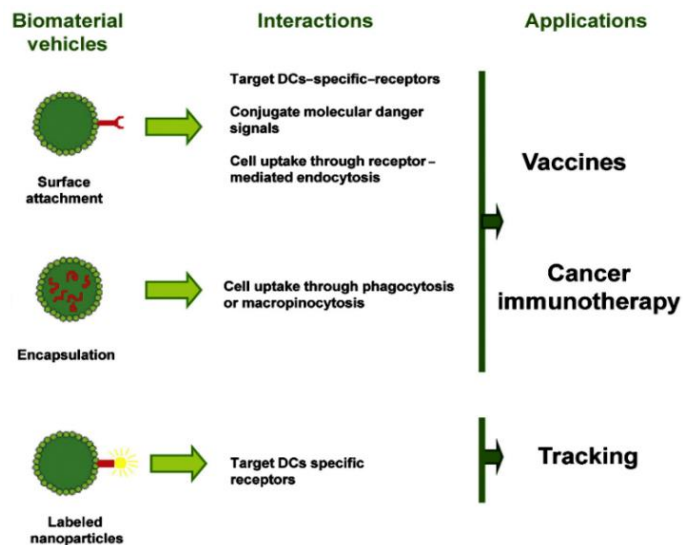


Figure 6.3. Possible interaction between NPs and dendritic cells. The antigen attached to NP surface or encapsulated can be targeted to the DCs for vaccines or cancer/immunotherapy and tracing if labelled¹⁷¹

When the immune cells interact with nano/micro-structured materials, inflammatory or allergic reactions can be induced, because the immune cell role is to recognize and eliminate potentially dangerous foreign structures. Thus, in the case of medical purposes, nanomaterials can produce side effects on the patients, for instance, fever, nausea, emesis, headache, and even shock.^{172,173} For this reason, it is fundamental to understand if the interaction with nanoparticles could have toxic effects to the human immune cells, or if it could cause the release of cytokines or the generation of oxygen free radicals. The cytokine release can be evaluated by the enzyme-linked immunosorbent assay (ELISA), which is a technique used for the quantification of macromolecules (peptides, proteins, antibodies) in the supernatant of cell cultures: capture antibodies are immobilized on a solid surface and, when the supernatant containing the antigens is added, they capture the specific antigen; a detection antibody specific for the antigen (the cytokines for example) is added and, after binding the immobilized cytokine, it produces a measurable signal, such as fluorescence with an intensity proportional to the cytokine concentration. In particular, it is important to evaluate the release of cytokines IL-6 and TNF- α , which are pro-inflammatory and immune-stimulatory molecules involved in the systemic acute phase, characterized by fever, headache, anorexia, nausea, emesis, and changes in the sleep-wake cycle^{174,175} and of the cytokine IL-12, which has the role of stimulating the natural killer cells and the T lymphocytes.¹⁷⁶

Also, the size of the nanoparticles is to be controlled, since it affects the cell internalization process, being it or not receptor-mediated. Furthermore, NPs can be engineered to expose specific ligands to activate receptors such as TLRs (toll-like receptors), which can recognize typical features present on pathogens and microbes and activate an inflammatory response.

A limitation of the use of inorganic materials for biomedical application is their possible ability to stimulate or to damage immune cells, such as dendritic cells, having the role of presenting the pathogens to the lymphocytes and triggering the immune response by release of cytokines. Thus it is really fundamental the absence of NP toxicity toward this cellular line and of immune system activation.

A biocompatible material can be inert or bioactive and is not able to induce toxic, nor immunogenicity effect into the host. This is the case of pSi, which can be both

inert, or bioactive as a scaffold for bone tissue growth.¹⁷⁷ The effects of both pSi layers and particles on cytotoxicity and immune response were investigated by several research groups. In the former case, it was demonstrated for numerous cell lines, that the surface modification strongly affects cell growth and attachment.^{178–180} The cytotoxicity depends on the degradation products of pSi, i.e. silicic acid, which is relatively harmful, and ROS (reactive oxygen species), which are molecules that regulate the cell life and whose production strongly depends on the pSi surface chemistry.¹⁸¹ The cytotoxicity also depends on the size of the microparticles and on the cell line. In fact, some studies reported that particles smaller than 3 μm were non-toxic to monocytes;¹⁸² particles smaller than 500 nm were non-toxic to lymphoma cells¹⁸³ and particles smaller than 1 μm were non-toxic to macrophages and endothelial cells.¹⁸⁴ The toxic effects of the surface stabilization treatments (oxidation, carbonization or hydrosilylation) were compared for different cell lines, such as lens epithelial cells¹⁸⁵ and Chinese hamster ovary cell.¹⁸⁶ From these studies it was clear that the viability and the morphology of the cells mainly depend on the surface functionalization. Among the several applications, pSi was investigated as a promising platform for controlled release of drugs, thanks to the high surface-to-volume ratio. Due to its stability at low pH, it is suitable for delivering in the small intestine¹⁸⁷ and the delivery of small siRNA was effective in silencing the target gene of an oncoprotein in-vivo.¹⁸⁸ pSi is also suitable for vaccination if antigen-loaded and the consequent DCs activation leads to stimulate the immune system and the T-cell activation, but without activating by its own the immune system.¹⁸⁹

6.2. Porous silicon microparticles interaction with human DCs

The goal of the study presented in this chapter is the assessment of the effect induced by TiO_2 coated microparticles (see Chapter 5) on human dendritic cells and its comparison with the effects of uncoated pSi-COOH microparticles and bacterial molecule LPS (lipopolysaccharide), which is usually used as standard to activate the cells of the immune system.¹⁹⁰ In particular, we were interested in cell viability, cytokines and O_2^+ released by the immune cells.

The pSi-COOH microparticles were prepared by electrochemical etching of crystalline silicon wafer in HF solution and functionalized with acrylic acid, as described in Chapter 3. Then, the inorganic coating was deposited, as described in Chapter 5, by ALD technique in a rotary reactor. pSi-TiO₂ microparticles (samples B1 and B2) were taken into account, to study the immune cell viability and the activation of the immune response upon pSi incubation.

The evaluation of biocompatibility and immunogenicity of the pSi microparticles was done in strict collaboration with Marta Donini and Prof. Stefano Dusi at the Department of Medicine, Division of General Pathology, University of Verona.

Upon approval of the Ethical Committee for the “Sperimentazione Clinica delle province di Verona e Rovigo (Prot. no. 46134, October 4th, 2016)” and after written informed consent, buffy coats from the venous blood of normal healthy volunteers were obtained from the Blood Transfusion Centre at the University Hospital of Verona upon approval of the Ethical Committee of “Azienda Ospedaliera Universitaria Integrata di Verona” (Prot. no. 5626, February 2nd, 2012). Peripheral blood mononuclear cells were isolated using Ficoll Hypaque and Percoll (GE Healthcare Life Science) density gradients. To generate dendritic cells (DCs), monocytes were incubated at 37 °C in 5% CO₂ for 5–6 days at 106 mL in 6-well tissue culture plates (Greiner, Nurtigen, Germany) in RPMI 1640 medium, supplemented with heat-inactivated 10% low endotoxin FBS, 2 mM L-glutamine, 50 ng/mL GM-CSF, and 20 ng/mL IL-4. The final DC population was 98% CD1a+, as measured by FACS analysis.

The monocytes, dendritic cell and lymphocytes viability was evaluated using an alamarBlue® assay, the superoxide anion production was evaluated by Cytochrome C reduction and the immune response activation was evaluated by ELISA assay basing on the release of the cytokines (TNF- α , IL-6 and IL-12).

The evaluation of the microparticles uptaken by the DCs was performed by optical microscopy, TEM analysis and the luminescence of the microparticles inside the cell was studied by two-photon absorption (2PA) experiment.

The instrumentation used and the relative obtained information are reported in Table 6.1 and the experimental steps are reported in the following Figure 6.4. All the detailed experimental techniques are reported in Appendix A2.

Table 6.1 Characterization techniques and related information

Characterization	Technique	Measurement information
In-vitro test	alamarBlue® assay	Cell viability
	ELISA assay	Immune response
	Cytochrome C reduction	Superoxide anion production
Imaging	TEM	Internalization, single cell
	Optical imaging	Internalization
	2PA	Internalization and photoluminescence

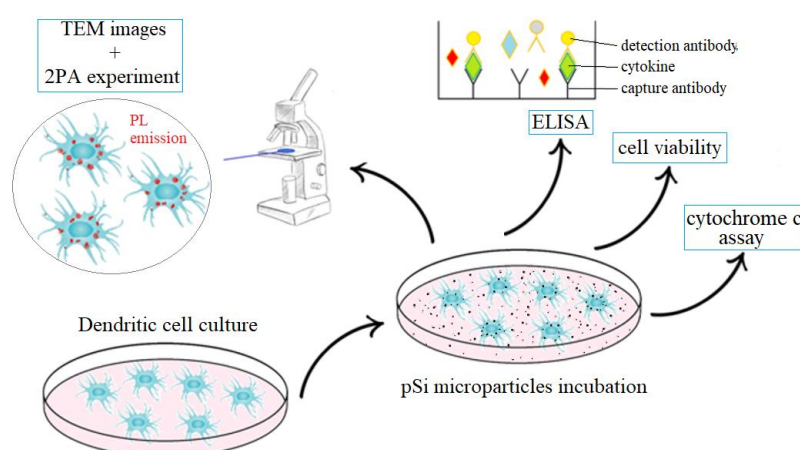


Figure 6.4 Experimental steps to perform cell viability tests, immune assays and cell imaging.

6.3. Imaging of the human DCs and the microparticles

Due to the small dimension of animal cells, that mainly range from 10 to 20 μm , depending on the type of cell, microscopes are useful to visualize their shape and internal structures, to understand their state of health, or as in this case to verify the internalization of particles. The principal methods used to visualize the cells are optical examination, fluorescence and electron microscopy. Specifically, a lot of stains procedures were developed to image the features of the cells, in a more detailed way by optical microscopes; the labelling of cell components with fluorescent probes allows to visualize them by fluorescence microscope and much smaller structures can be distinguished by electron microscopy.¹⁹¹

The internalization of the pSi microparticles was investigated by optical microscopy, electron microscopy and two-photon absorption experiments. By optical microscopy, we assessed whether the pSi-TiO₂ microparticles were ingested by human

DCs and if they affected the viability of the cells (see Figure 6.5, for pSi-TiO₂ microparticles B1, as a representative sample).

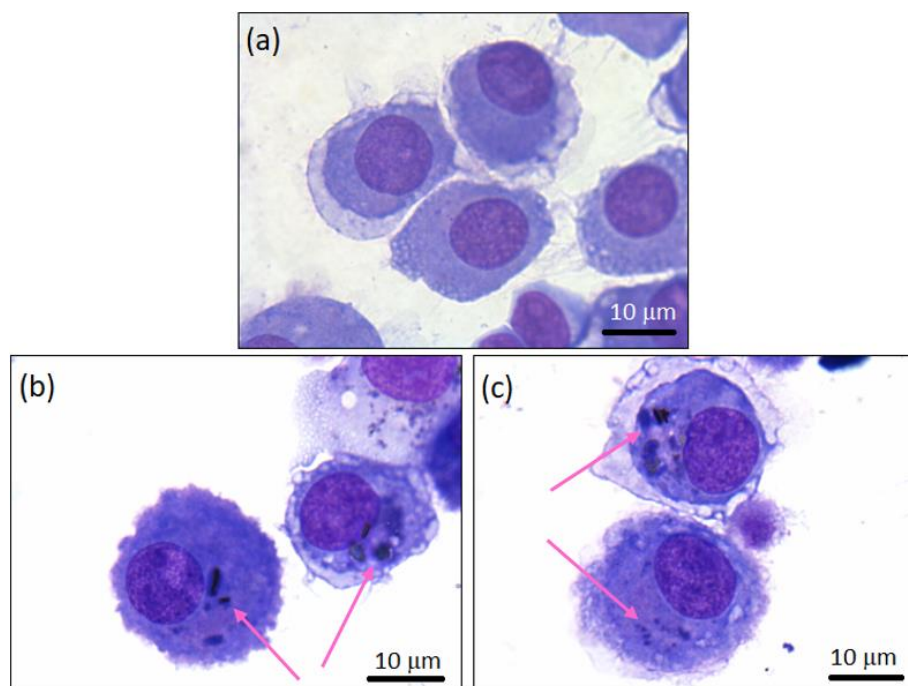


Figure 6.5 Light microscopy of May-Grunwald-Giemsa-stained DCs: cells cultured in the absence (panel a), or presence of 50 µg/mL pSi-TiO₂ microparticles (sample B1). Ingested particles are indicated by arrows (panel b and c).

To visualize the cell structures illustrated in Figure 6.5, the May-Grunwald-Giemsa stain was employed. This stain is composed of two colourants that interact preferentially with different cellular components, thus allowing to distinguish the nucleus (pink coloured) with respect to the other structures of the cell, such as the cytoplasm (blue-violet coloured). In Figure 6.5(a) an image of cells cultured without microparticles (i.e. the control) is reported for comparison; in panel b and c, microparticles internalized by the cells (indicated by arrows) can be observed. All of the images show healthy cells, that are characterized by an entire and well-defined nucleus and by homogeneous shapes. The presence of the microparticles inside the cytoplasm do not induce any apoptotic (cell death) effect: in fact, DCs appear to be viable upon incubation with different microparticles concentrations.

To better investigate the pSi microparticles uptake by the DCs, TEM analysis on single cell has been performed after the incubation with pSi-TiO₂ (sample B2) as a representative sample: some images are reported in Figure 6.6.

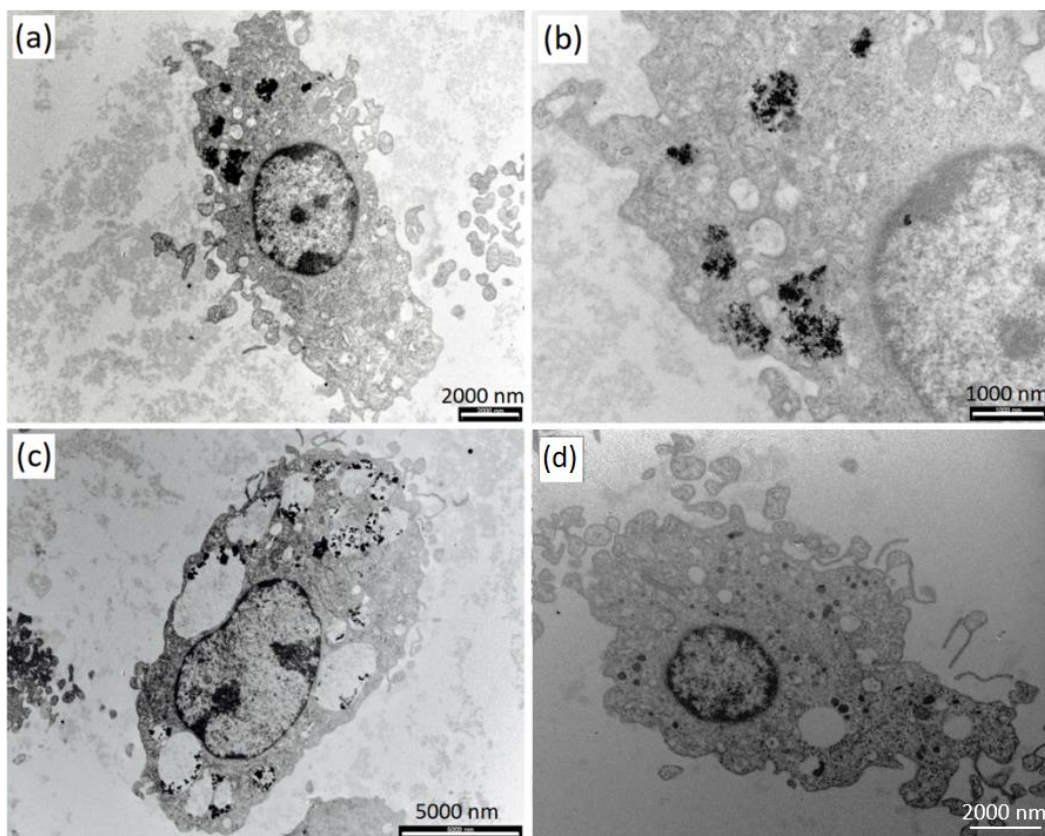


Figure 6.6 TEM of a single cell showing $pSi-TiO_2$ microparticles (sample B2) internalized by DCs.

This technique, having a much higher resolution with respect to optical microscopy, allows to obtain information also on the subcellular structures, but a complex preparation is required for such organic samples.

Figure 6.6 (panel a, b, d) shows some representative dendritic cells and panel b shows a zoomed portion of the cell in panel a, to better appreciate the microparticles internalization. All the cells look healthy, with a well-defined and unique nucleus and the small excrescences at the border of the cell, which are the dendrites, partially visible by optical images. Some of the dendrites seem to be detached from the cell, but this is due to the sample preparation: the cells are pelleted, embedded in a resin and then cut in ultrathin layers, to be imaged by TEM. It is possible that this procedure cuts also some dendrites. Moreover, this procedure confirms that the microparticles are effectively internalized and not deposited on the membrane.

The dark areas inside the cells represent the microparticles, that in panel c, look internalized in vacuoles (i.e. the void bubbles inside the cells). In contrast, particles do not enter the nucleus, where the darker areas represent the chromatin, which is

the complex of DNA and proteins. Concerning the mechanism of pSi microparticles ingestion by the cells, it has been demonstrated that they are ingested by endocytosis mechanisms.¹⁴⁰ The interaction mechanism of pSi-TiO₂ microparticles is not mediated by receptors, as previously reported by Serda et al. for discoidal pSi microparticles uptaken by endothelial cells.¹⁹² In this study, the internalization was shown to be initiated by actin-based pseudopodia, that engulf the microparticles to store them in vesicles. Similarly, we observed the presence of the pSi-TiO₂ microparticles in vesicles inside the dendritic cells, but no clear evidence of internalization by means of pseudopodia was verified. Further investigations are necessary to understand completely the mechanism of cell uptaken.

Two-photon absorption experiments (2PA) are necessary to verify if the pSi microparticles photoluminescence is conserved after particles uptake by DCs and if the inorganic coating (described in Chapter 5) is efficient to stabilize the optical emission properties of the pSi microparticles in biological media. 2PA technique is necessary for the investigation of such microparticles because they are luminescent upon excitation in the UV range, whose wavelength is not transparent in the biological tissues. To solve this problem, 2PA technique is based on the simultaneous absorption of two IR photons: it is possible to excite the pSi microparticles at 700 nm instead of 350 nm (i.e. in the UV) and observe the photoluminescence of the microparticles inside the cell.

The DCs incubated with pSi microparticles were washed with PBS (to remove the microparticles which were not internalized) and deposited on a microscope slide for the observation. 2PA images of DCs incubated with pSi microparticles (sample B2) are reported in Figure 6.7. The fluorescence images are obtained upon 700 nm excitation (perfectly matching the 350 nm excitation of standard pSi PL measurements) and the image of the cells is acquired by 488 nm laser in total reflection modality. Z-stack images were merged to obtain a maximum projection image, shown in panel (a) and the highlighted regions in panel (b) and (c).

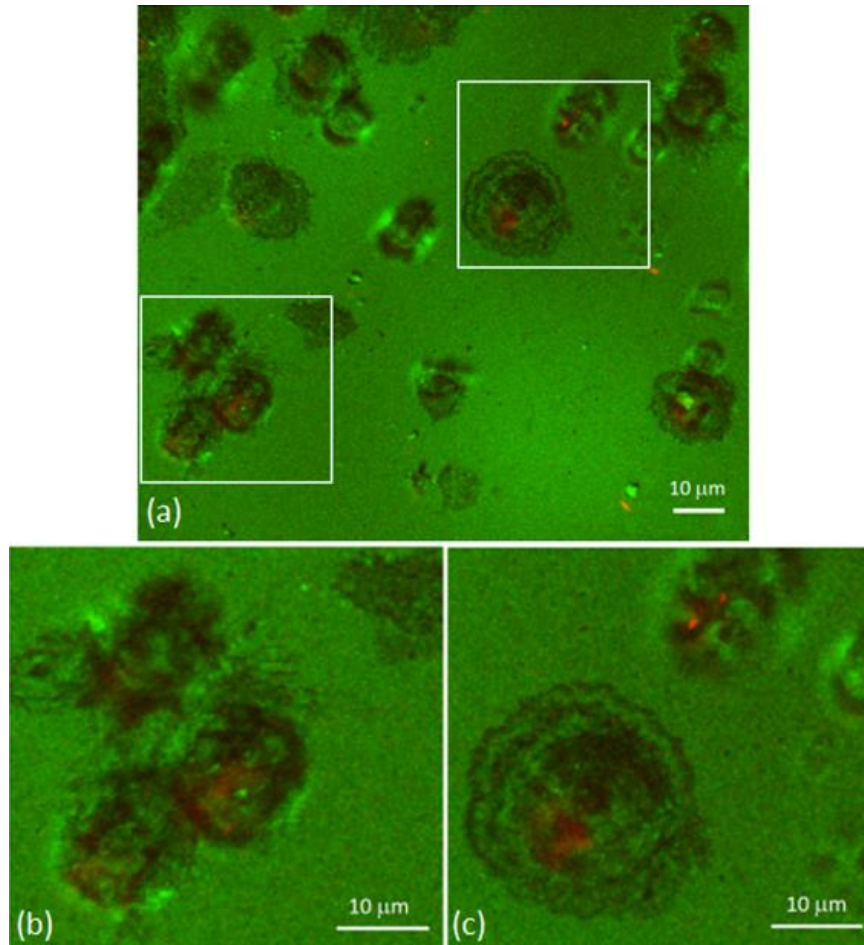


Figure 6.7 Two-photon absorption image of pSi-TiO₂ microparticles (sample B2) internalized in DCs. The cells are represented in green colour scale, while the PL of the microparticles in the red colour scale (panel a). Zoom of the highlighted areas (panel b and c).

The 2PA images clearly show that the microparticles (in red-colour scale) are internalized by the cells (in green-colour scale), which do not present apoptotic signals. Moreover, Figure 6.7 shows that microparticles are still light-emitting. The lack of perfect superposition between the features of the total reflection image, in green, and the two-photon image, in red, (see the dots at the right bottom of the image) is related to the fact that the images cannot be taken at the same time and hence a shift of the sample could occur since the cells are not fixed, but just deposited on the microscope slide.

The prove that microparticles are indeed internalized by the cells is given by the fact that they remain visible after washing with PBS to remove the excess of microparticles. Moreover, microparticles are visible in every stacked scan, at different

depths, reported in Figure 6.8 for a single cell (see Figure 6.7 c). For each scan, the image relative to the morphology and to the photoluminescence are merged.

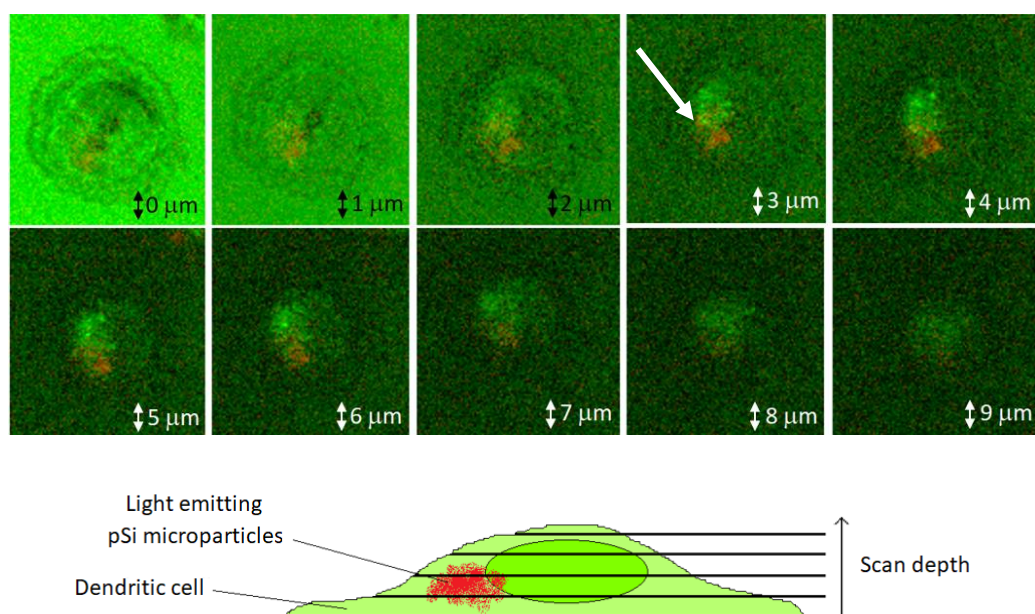


Figure 6.8 2PA stacked scan at different depth (reported in each image) of a single DC containing pSi light-emitting microparticles (red colour). A schematic representation of the stacking images is reported, to demonstrate the possibility to verify if the light-emitting microparticles (indicated by an arrow) are inside the cells.

A schematic representation of the stacking images is reported in the bottom part of Figure 6.8, in which a single dendritic cell is illustrated: the ellipse in the centre represents the nucleus, the red spots are the light-emitting microparticles and the horizontal lines are the stacked image planes; Such stacking demonstrates the possibility to verify if the light-emitting microparticles are located inside the cell or on the cell surface. In our case, we can state that the microparticles are inside the cell since the red emission (indicated by an arrow) is observed only for the central images.

6.4. Cytotoxicity evaluation

Viability assays are indispensable to assess the toxicity of substances that are added to the cells. Toxic molecules can induce various cell damages, such as loss of membrane integrity, cell swelling, and cell lysis, that can lead to apoptosis (controlled cell death) and/or necrosis. Depending on the type of cell culture,

different viability assays can be performed, which study physiological functions (deformability, motility), adhesion, division ability and membrane rupture. Some assays evaluate cell proliferation, such as the alamarBlue assay used in our experiments. This assay is based on the measurement of metabolic activity of the cell: resazurin is a dye that undergoes reduction upon metabolization, and the reduced dye is highly fluorescent. Thus a decrease of fluorescence is related to a decrease of dye metabolization and therefore of cell viability.

The tests concerning the ability of pSi-TiO₂ microparticles to affect cell viability were performed on human immune cells (monocytes, lymphocytes and dendritic cells) with the results summarized in Figure 6.9.

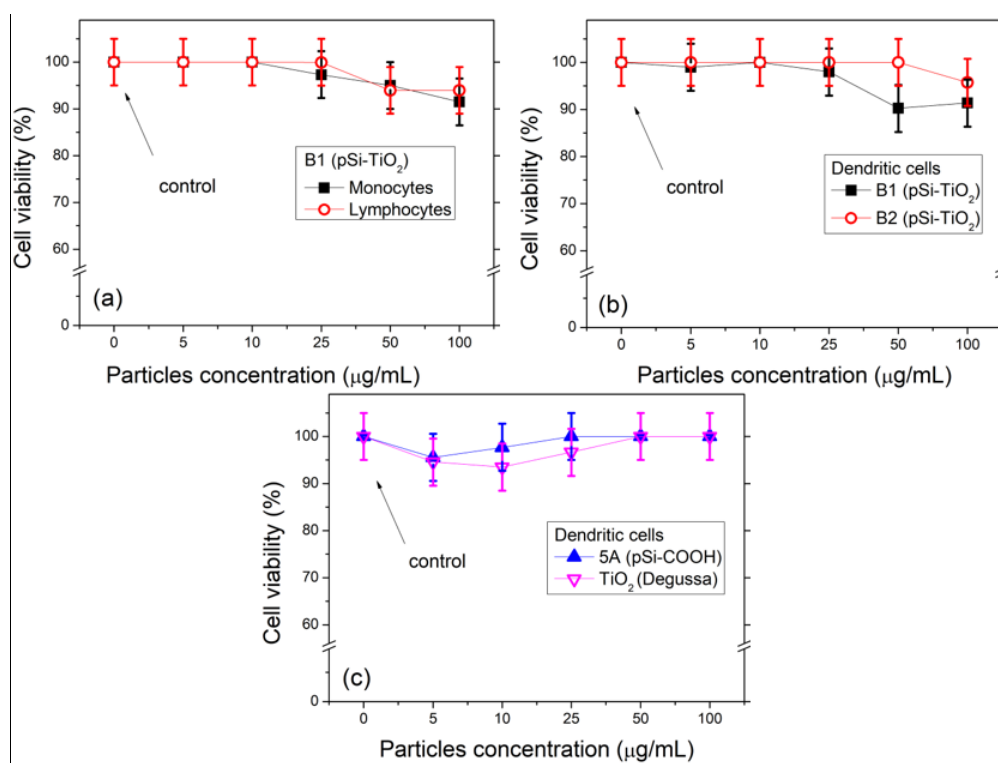


Figure 6.9 Viability of human immune cells as a function of the microparticles concentration: monocytes and lymphocytes incubated with sample B1 (panel a), DCs incubated with sample B1, B2 (panel b), Ref(5A) and TiO₂ powder (panel c).

With this aim, the human immune cells were incubated with different pSi microparticles concentrations and the cell viability was evaluated by alamarBlue assay, which measures the presence of molecules produced by healthy cells, as previously described. It is to note that the use of assays, such as Alamar Blue, was found to be

unreliable in some cases. Low et al.¹⁸⁰ evaluated the use of two types of assays. One (Alamar Blue) is colourimetric and is based on the reduction of resazurin by cellular enzymatic reactions, meaning that the more the cells are alive, the more resazurin is reduced. In this study, they observed that resazurin was reduced by pSi, even in the absence of the cells, due to the oxidation of this material in an aqueous environment. They proved that porous silicon dissolved (or turned from Si to SiO₂) proportionally with the reduction of resazurin. A different assay used was based on the neutral red dye incorporation, which is possible only in alive cells. Also, in this case, the assay was falsified by the trapping of the dye into the pores of the material. Additionally, Korhonen et al.¹⁸¹ investigated the use of thermal oxidized/carbonized microparticles for the controlled release of drugs, to treat chronic retinal eye diseases. They evaluated the cell viability by two different colourimetric assays (CellTiter-Blue and CellTiter-Fluor to measure metabolic and protease activity, respectively). As for the previous work, they observed no compatibility with the Blue assay and the oxidized pSi microparticles since a signal of metabolic activity was present even in the absence of cells. The Fluor assay was instead more reliable than the others. Concerning our results, by coating the pSi surface with a TiO₂ nanolayer, we avoid both oxidation and degradation of pSi in an aqueous environment, as reported in Chapter 5 and as proved by the PL emission inside the cells (Section 6.3). Therefore, caution should be employed, even if the stability of coated pSi microparticles should avoid the more as possible the resazurin reduction and we observed alive cells by microscopy analysis. In future studies, we should think about comparing the results with different viability assays.

We previously proved that pSi-COOH microparticles (i.e. the uncoated sample) did not induce any toxic effect on the human immune cells¹⁴⁰ and accordingly, in Figure 6.9(a) we can observe that the pSi-TiO₂ microparticles (sample B1), do not affect the vitality of lymphocytes and monocytes after 24 hours incubation. In fact, the cell viability was 90 % even at high microparticles concentration (100 µg/mL). Similar experiments were performed with human dendritic cells for both sample B1 and B2 and Figure 6.9 (b) shows that none of the samples induced the cell apoptosis or necrosis, up to 100 mg/mL concentration. We can observe that the viability was higher than 90% for any microparticles concentration. For the sake of completeness,

the cytotoxic effect was evaluated also for un-coated pSi microparticles and TiO₂ powder, that was employed in the inorganic layer deposition (Chapter 5). Also in these cases, we observed no variation in the cell viability, thus meaning that pSi microparticles and titanium dioxide are not toxic, as taken separately. In conclusion, pSi microparticles, before or after being coated, do not induce any cytotoxic effect in the cells of the immune system and this is important to be explored since these cells are the first ones that come in contact with foreign materials, such as the microparticles.

Activated human DCs were proved to release a lot of oxygen free radicals (reactive oxygen species - ROS),¹⁹³ such as superoxide anion (*O₂⁻), hydrogen peroxide (H₂O₂), hydroxyl radical (OH⁻), singlet oxygen, and lipid hydroperoxides, that are able to affect the cell causing the so-called oxidative stress. Thus, we investigated if pSi-TiO₂ microparticles could stimulate the DCs in this sense. The ROS production can be evaluated by several methods, one of which is the cytochrome c reduction assay. In fact, the superoxide anion reduces the cytochrome c (a molecule isolated by horse heart and added to the cells in the assay). We found that both coated or uncoated pSi microparticles were not able to induce O₂⁻ release, neither alone nor in combination with LPS. This means that pSi microparticles do not induce the production of toxic oxygen radicals.

6.5. Immune response evaluation

After proving the absence of toxicity towards the immune cells, it is important to evaluate the immunogenicity of the microparticles, that is their ability to induce the immune and the inflammatory response. Dendritic cells release cytokines to stimulate the other cells of the immune system, the lymphocytes, to trigger a response aimed to eliminate the foreign material. It is very important that a biomedical material is neither immunogenic nor removed from the organism by immune cells.

To evaluate whether pSi microparticles could activate the immune response, we performed ELISA assays to quantify the production of cytokines able to activate the immune cells by DC. First of all, in Figure 6.10 we can visualize the response

of DCs upon microparticles (panel b) and LPS (panel c) incubation, in optical microscope images, and compare it to the control (i.e. no foreign material incubation, panel a). LPS (lipopolysaccharide) is an endotoxin that can cause a very intense cytokine release and so we used it as a positive control.

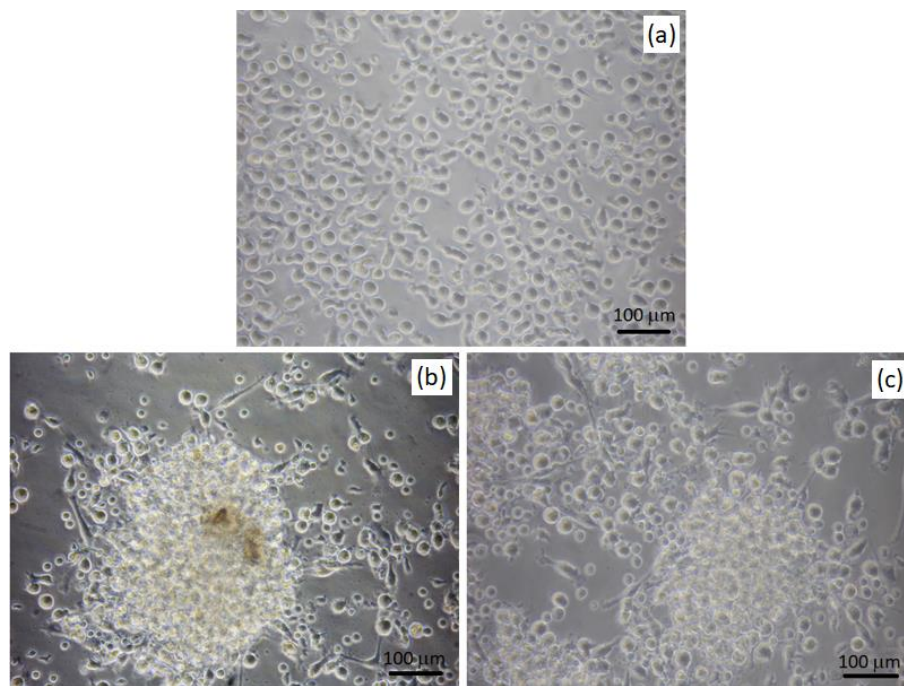


Figure 6.10 Optical microscope images of DCs cultured without microparticles (panel a), with 50 µg/mL pSi-TiO₂ (sample B1) microparticles (panel b) or with LPS (panel c).

Figure 6.10 (a) shows that control DCs are well distributed because no foreign material is added. Differently, upon addition of microparticles or 100 ng/mL LPS, the cells are activated and aggregated. The ability of pSi-TiO₂ microparticles to stimulate DCs activity was then quantitatively evaluated by ELISA assays on culture supernatants, by detecting the number of released cytokines by the DCs after the incubation with pSi-TiO₂ microparticles (samples B1 and B2). The cytokine production due to the coated pSi microparticles was compared to the one obtained upon stimulation with LPS alone (used as positive control) as well as to the one observed upon co-stimulation with pSi microparticles plus LPS (Figure 6.11). In particular, we monitored the presence of TNF- α (tumour necrosis factor- α), which is a multifunctional cytokine involved in the acute phase reaction, IL-12 (interleukin-12), that stimulates lymphocytes and NK cells, and IL-6 (interleukin-6), that is a pro-

inflammatory cytokine. Figure 6.11 shows no or weak release of IL-12, IL-6, and TNF- α cytokines after DC incubation with B1 and B2 samples at concentrations up to 50 $\mu\text{g/mL}$.

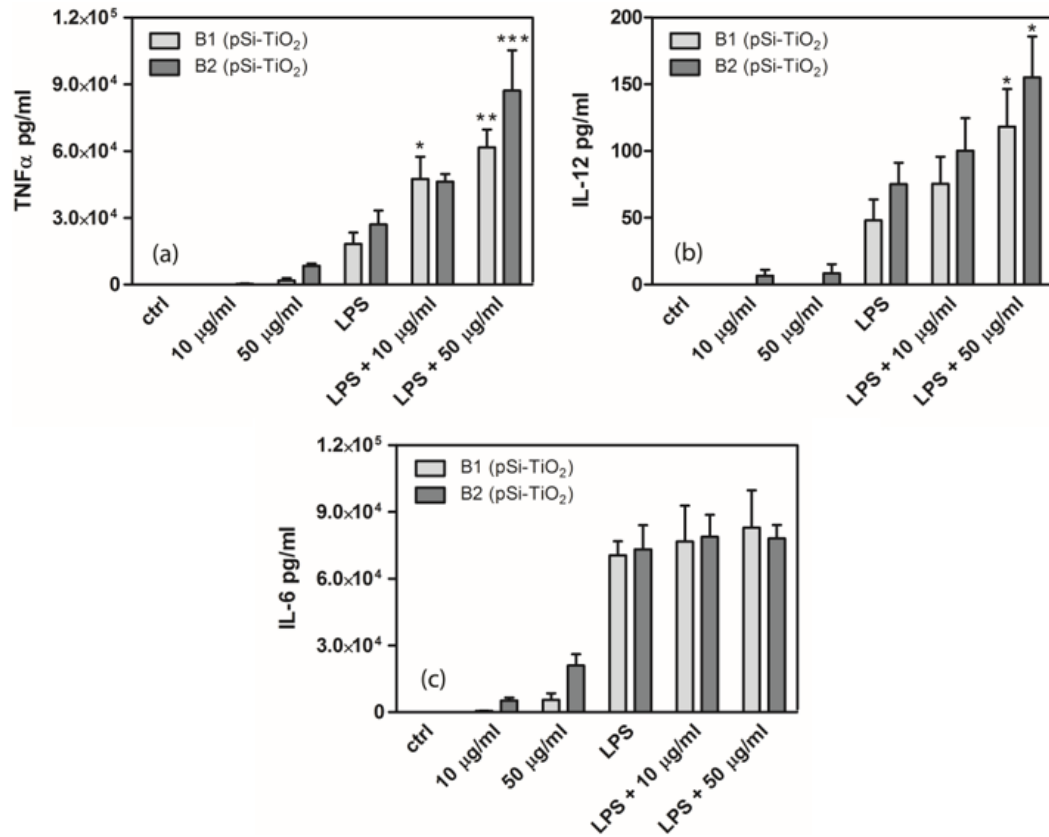


Figure 6.11 Evaluation of cytokine secretion by DCs upon challenge with different pSi-TiO₂ microparticles sample (B1 and B2) with and without the addition of 100 ng/mL LPS: TNF- α (panel a), IL-12 (panel b) and IL-6 (panel c). The results are expressed as the mean value and standard deviation of five independent experiments. Statistical analysis: DCs treated with LPS plus pSi-TiO₂ microparticles versus DCs stimulated with LPS alone; * $P < 0.05$, ** $P < 0.01$, *** $P < 0.001$.

Conversely, LPS induced a high release of all the investigated cytokines. Interestingly, when DCs were co-stimulated with LPS plus microparticles we observed a dose-dependent increase of the released cytokines as compared with DC stimulated with LPS alone, a so-called “priming effect”.

Priming effect

Priming effect represents enhanced responsiveness, taking place when a pre-stimulated cell is subsequently treated with a second stimulus.¹⁹⁰ Knowing that LPS

is involved in priming effect, we wondered whether also the cooperation of pSi-TiO₂ microparticles and LPS could lead to increased cytokine release by DCs. In fact, we considered being important to assess whether nano/micro-structured material or other agonists could potentiate the immune-activating effect of bacterial components (such as LPS) present in the biological environment, leading to unwanted side effects, such as allergy or autoimmunity. The possibility of a priming effect is rarely taken into account by authors who investigate the biocompatibility of nanostructures to be used in biomedical applications.

Figure 6.11 shows a “cell priming” effect in the release of cytokines TNF- α (panel a) and IL-12 (panel b) upon co-stimulation with microparticles plus LPS, while for IL-6 cytokine this behaviour is not observed. Hence, we can state that there is a cooperative effect between LPS and pSi-TiO₂ microparticles, which enhances the release of IL-12 and TNF- α cytokines. Therefore, to properly evaluate the immune-activating and pro-inflammatory potentials of materials to be used in nanomedicine, attention has to be paid. In fact, there is the possibility that an apparently inert material could cooperate with other molecules becoming able to activate the immune response. So, the administration of an apparently innocuous nanomaterial to a patient could cause unwanted effects if it collaborates with substances present in his body, for instance, bacterial components or products.

It is not clear the reason why the synergistic triggering of cytokines release happened just for IL-12 and TNF- α , while no priming effect was found for IL-6 and oxygen-free radical production. This behaviour has to be better investigated in future research studies.

Moreover, the same experiments of co-stimulation with LPS performed with coated microparticles were also carried out with uncoated pSi-COOH microparticles. The amount of IL-12, IL-6, and TNF- α cytokine released upon microparticles stimulation is reported in Figure 6.12.

Fig. 6.12 shows that the incubation with pSi-COOH microparticles, up to 50 $\mu\text{g/mL}$, induced no or a very small release of cytokines by DCs. Upon co-stimulation with LPS, we did not observe the above described “priming effect”, for none of the investigated cytokines. Since the only difference of the two microparticles is the presence or not of the coating, we could attribute the appearance of the priming effect

to the titanium dioxide coating, or maybe to the fact that the titanium coating renders the microparticles more stable and their degradation slower.

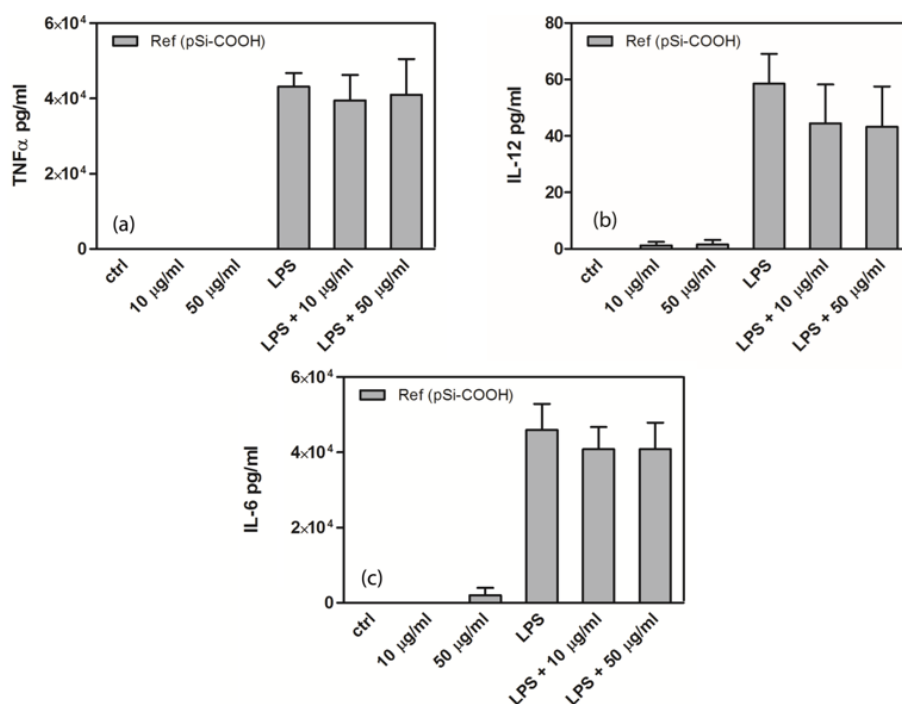


Figure 6.12 Evaluation of cytokine secretion by DCs upon incubation with different pSi-COOH microparticles with and without the addition of 100 ng/mL LPS: TNF- α (panel a), IL-12 (panel b) and IL-6 (panel c). The results are expressed as the mean value and standard deviation of five independent experiments.

Anyway, the priming effect has to be better investigated in future research studies, for example by incubating the dendritic cells with commercial TiO₂ particles and LPS. The comparison with the results obtained for pSi-TiO₂ microparticles could explain if the priming effect is due to the TiO₂ or to its combination with the pSi microparticles.

6.6. Conclusions

We investigated the cytotoxicity and the immunogenicity of the porous silicon microparticles, which is a needed step for the exploitability of this material in theranostics. In particular, we proved that:

- The pSi microparticles are ingested by the dendritic cells, via a non-receptor mediated mechanism. Optical and TEM images show that the viability of the cells is not affected by the interaction with the microparticles, which in

some cases are internalized inside vacuoles. Furthermore, two-photon microscopy shows that the photoluminescence of the microparticles is maintained inside the cells (proving the effective inorganic coating, studied in Chapter 5)

- The viability of the cell was evaluated: dendritic cells, monocytes and lymphocytes were incubated with different concentrations of pSi microparticles, both with and without the inorganic coating. No signal of cell death was found even at high microparticles concentration (up to 50 $\mu\text{g}/\text{mL}$). This confirms the well-known absence of the pSi microparticles toxicity for the immune cells
- pSi microparticles were not able to induce ROS release, neither alone nor in combination with LPS, meaning that the presence of pSi microparticles do not induce oxidative damage performed by dendritic cells
- Immune response was investigated by evaluating the release of the cytokines by the DCs upon stimulation of coated and uncoated microparticles: a negligible number of cytokines are released, for concentrations up to 50 $\mu\text{g}/\text{mL}$.

Nonetheless, we found that this material could be bioactive, in the sense that it can potentiate the cytokine production by LPS-stimulated DCs. Therefore, microparticles injected in a patient could excite DCs in the presence of bacterial molecules, such as LPS, that could be generated by already present pathogens or host tissue. Our contribution is mainly related to the concept that it is possible to have a scarcely estimated pro-inflammatory potential if the material under investigation is tested alone, while its activity in collaboration with other agonists has to be taken into account.

Our results suggest that pSi microparticles with or without coating do not have any toxic effect and are not able, alone, to stimulate the DCs response, thus meaning that this material has good chances to be used for theranostic applications and to be traced by optical imaging.

CHAPTER 7

IMMUNE ADJUVANTS DELIVERY FOR IMMUNOTHERAPY: A PRELIMINARY STUDY

In the previous chapters, we showed how functionalized pSi microparticles are good candidates for theranostic applications: they have neither toxicity nor immunogenicity towards the human immune cells. The deposition of an inorganic coating allows stabilizing the optical emission properties for months in biological media (see Chapter 5), with the opportunity to trace the material inside the cells, as proved in Chapter 6.

Within this chapter, we complete the trajectory towards theranostics by presenting some preliminary results about the employment of pSi microparticles as carriers of vaccine adjuvants in perspective of immunotherapy. In particular, we select Pam3CSK4, a small positively charged lipopeptide, able to enhance immune responses mediated by dendritic cells and we evaluate the cell activation by measuring the cytokine release. Then, we investigate the effect of different concentrations of Pam3CSK4 loaded on pSi microparticles on human DCs.

7.1. Immunotherapy and vaccine adjuvants

The role of the immune system is the defence from pathogens and aberrant growing and proliferating cells, such as cancer cells. Immunotherapy is a promising strategy whose aim is to enhance the immune response to fight against infections and cancer. This effect can be achieved in several ways, including the stimulation of dendritic cells (DCs) by means of molecules, i.e. vaccine adjuvants.^{194,195} In this kind of therapy, the DCs of the patient are firstly isolated (for instance from blood monocytes) and stimulated by antigens (specific for the disease) and vaccine adjuvants. After being activated, the cells are re-injected into the patient. [2] DCs are particularly suitable for immunotherapy since they are able to coordinate adaptive and innate immunity. As immature cells, they sample the surrounding environment, engulf

pathogens, after TLR (Toll-like Receptors) recognition, and trigger the immune response, by releasing specific cytokines. [3]

As an example, aluminium hydroxide is an adjuvant used in clinics, [4] but there is the need to develop a new generation of vaccine adjuvants based on TLR recognition. The TLRs are transmembrane proteins present on the surface and internal membrane of immune cells (macrophages and DCs), which are involved in the innate immune system activation, by recognizing typical structures of pathogens and microbes in the extracellular environment. [5] The recognized structures are part of the PAMPs (pathogens associated molecular pattern), a group of molecules including LPS (lipopolysaccharide), which was used to stimulate the DCs in Chapter 6, and LP (lipoprotein). The recognition of the PAMPs induces a release of pro-inflammatory cytokines, such as IL-6, IL-12 and TNF- α , which trigger the activation of the lymphocytes. Therefore, the local or systematic administration of such PAMPs is interesting in the field of vaccine research, to increase the immune cell activity against the disease. [6] LP is considered as the best TLR stimulator and gained interest in the development of new TLR agonists in perspective of immunotherapy. The reason why TLR ligands are not widely used in clinics and the need to improve the existent ones is related to their poor stability and effectiveness *in vivo*. [3] Furthermore, in the case of subcutaneous vaccination, a lot of vaccine molecules are cleared in the body, or uptaken by cells other than DCs. To protect and avoid the clearance of the vaccine adjuvant (Pam3CSK4 and Poly I:C, in this case), PLGA nanoparticles were exploited as a carrier, and the attachment of a proper ligand, *i.e.* CD40, allowed the correct targeting towards DCs. [7] Furthermore, the simultaneous injection of a photosensitizer led to a synergic action of immunotherapy and PDT (photodynamic therapy), very effective in eradicating cancer cells. [8]

7.1.1. Pam3CSK4

In this chapter, we focus on a particular molecule: Pam3CSK4 (palmitoyl-3-cysteine-serine-lysine-4), whose structure is reported in Figure 7.1 (a). It is a small and positively charged lipopeptide and agonist of the toll-like receptors TLR1 and TLR2, that are present on DCs membrane. More specifically, TLR2 needs to create a heterodimer with TLR1 (see Figure 7.1 (b)) to be able to recognize the specific

triacylated lipopeptides, such as Pam3CSK4. This molecule bears the same acylated amino-terminal portions of the immune-active bacterial lipoproteins (LPs), is therefore recognizable by DCs [9] and stimulates the release of specific pro-inflammatory cytokines, such IL-6, IL-12 and TNF- α by DCs. [10]

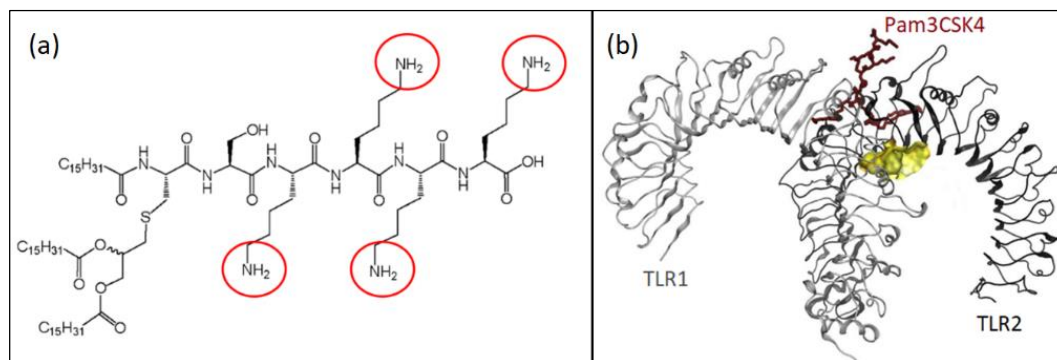


Figure 7.1 Structure of TLR agonist, Pam3CSK4. The amine groups are marked (panel a); Representation of TLR1-2 heterodimer to recognize Pam3CSK4 (panel b). [11]

TLR agonists, such Pam3CSK4, are frequently investigated as vaccine adjuvants because they are able to effectively induce the immune response by DCs activation. An ideal vaccine should induce a quick and long-term immune response with negligible autoimmune and allergic responses. For example, Pam3CSK4 in combination with poly I:C, a viral infection simulator, was found to synergistically enhance the B lymphocytes activation and increase antibody responses to protein vaccines in-vivo. [12]

7.2. Porous silicon delivery of Pam3CSK4

As reported in Chapter 1, drug delivery is related to the mechanism of therapeutic substances transportation inside the body, with the aim of prolonging its efficacy and avoiding its degradation. A carrier is employed with the aim of loading, protecting and transporting molecules to be released at a controlled rate and to a specific target. A lot of nanomaterials were investigated as drug delivery systems (DDS): organic (for example polymeric, lipidic) and inorganic (for example gold, silica) nanoparticles can encapsulate or bind drugs, to be released at a controlled rate. Porous materials are particularly suitable as DDS, having a huge amount of volume available for drug hosting. Moreover, they are interesting for the ability to

release a large amount of drug and to reduce the drug-related systemic toxicity. [13] For this application, mesoporous silicon microparticles are particularly indicated, due to its high loading capacity, its “tunable” surface chemistry, and its low toxicity. The release of the loaded molecules is triggered by the degradation of the porous structure in a biological medium, at a slow and controlled rate.

In porous silicon, molecules are usually hosted inside the pores and trapped by oxidation, at high or mild temperatures. This procedure reduces the drug degradation, [14] but unfortunately decreases the pore volume and sometimes quenches the photoluminescence of pSi. These particles can be used to deliver poorly soluble drugs, proteins, genes and nanoparticles. A lot of molecules were investigated for delivery by porous silicon and silica carriers, for example, antipyrine, ibuprofen, griseofulvin, ranitidine and furosemide towards oral delivery applications, [15] anticancer drugs, such as doxorubicin [16] and cisplatin, with folic acid attachment to target cancer cells. [17]

In previous studies, we performed some preliminary drug loading and release tests in-vitro, choosing cobinamide (Cbi - the precursor of B12 vitamin), a small and positively charged molecule that is used as cyanide antidote, and investigated the DDS feasibility of pSi microparticles as a function of the surface functionalization and coating. [18] In this case, we avoided the pore volume reduction available for drug loading and the PL quenching, by attaching and releasing Cbi only by electrostatic interaction. This is based on the fact that a positively charged molecule can be attracted by the negatively charged COOH groups of microparticles at acid pH and then, slowly released after dispersion in PBS (pH 7.4). Moreover, the porous silicon surface functionalization and PEG coating were found to be worthwhile to control the porous silicon redox activity towards the drug, which was not degraded. The study revealed that the loading capacity depends on the surface functionalization, which also determines the release rate, which is lower for negatively charged pSi microparticles.

After proving the suitability of pSi as a drug carrier, once opportunely functionalized, in this section of the thesis, we address the possibility to use pSi microparticles for vaccine adjuvant delivery, in perspective of immunotherapy. [19] In fact, it was

proved that upon infiltration with liposomes, loaded with a vaccine adjuvant (ovalbumin, a well-characterized model antigen), pSi is able to enhance the anti-tumour immunity, after DCs stimulation. [20]

In our case, Pam3CSK4 is chosen to fulfil the needs of a small (to infiltrate the porous structure of pSi microparticles with few nm pore size), positively charged molecule (to interact with negatively charged COOH groups). Pam3CSK4 is a highly efficient vaccine adjuvant, [21] recognized by TLR1/2 present on the surface of DCs and essential for T lymphocytes stimulation in-vivo, that are induced to release cytokines, stimulating the immune response. [22] This molecule bears 4 terminal amine groups (highlighted in Figure 7.1(a)), that at acid pH are positively charged and able to electrostatically interact with the terminal carboxyl groups (COOH) of functionalized porous silicon microparticles. We performed some preliminary investigation by using uncoated pSi-COOH microparticles as possible vaccine adjuvant carrier, to verify the efficacy of such a treatment, with the perspective of using coated microparticles, which are also photoluminescent stable.

7.2.1. Drug delivery and cell activation

Three steps have to be addressed to evaluate the exploitability of DDS: drug chemical stability, loading capacity and release time curve determination in-vitro. Moreover, we performed pSi uptake tests on monocyte-derived human dendritic cells. The aim was to study the effect of the vaccine adjuvant delivery on the DCs activation and evaluate a possible enhancement of the response in case of co-stimulation by pSi microparticles and Pam3CSK4.

The **molecule** (i.e. the vaccine adjuvant **Pam3CSK4**) **loading** on the pSi microparticles was assessed by means of optical microscopy (as a preliminary test) and by confocal microscopy; for this reason, a fluorophore-labelled molecule is needed. Thus, it is possible to image the photoluminescence coming from the labelled molecule and from pSi microparticles (i.e. the carriers) and to verify if there is a correspondence in position between them. In this case, we chose Pam3CSK4 labelled with rhodamine, hereafter named Pam3CSK4-R, with a very intense PL emission at 578 nm if excited at 555 nm.

The **release** of the molecule was studied **in-vitro** by spectrofluorimetry, in

PBS, as shown in Figure 7.2: first, a calibration curve is needed to correlate the intensity of the rhodamine PL signal to its concentration (a); then, the amount of released molecules is obtained by collecting the supernatant at set times, measuring its PL and replacing the removed supernatant with “fresh” PBS. By converting the intensity into molecule concentration, the release graph can be obtained (b).

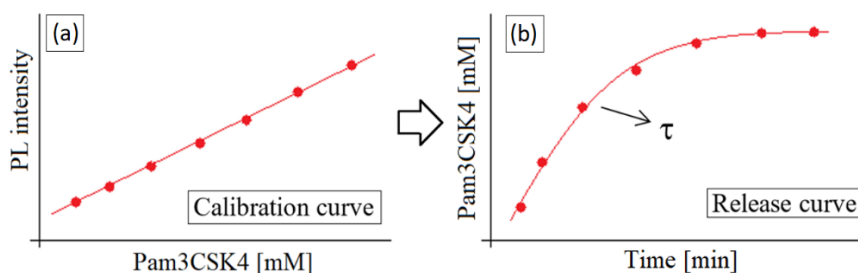


Figure 7.2 Calibration curve: correlation of PL intensity and molecule concentration (panel a); Release curve: released molecules at set times (panel b).

The **cell activation tests** are needed to assess the effectiveness of cell treatment with particles carrying the adjuvant. The estimation is performed qualitatively by optical imaging of the DCs, which undergo a shape change (elongation of the dendrites) after the activation, and quantitatively, estimating the amount of released cytokine, by ELISA assays. In fact, as already introduced in chapter 6, the DCs activation can be monitored by evaluating the release of cytokines, which are signalling molecules, that trigger the immune cells towards the immune response.

7.2.2. Experimentals

Pam3CSK4 loading. A 4 μM solution of protonated Pam3CSK4-R is obtained by adding 20 μL Pam3CSK4-R to 180 μL MES (2-(N-morpholino) ethanesulfonic acid) buffer at pH 5.8. This solution is added to 0.3 mg dried pSi microparticles (pSi-COOH_2 sample), re-dispersed with vortex and incubated 2 hours under mild rotation. To remove the unreacted molecules, the sample was centrifuged at 13000 rpm, the supernatant was collected and replaced with fresh MES buffer. This procedure was repeated twice. For cell activation tests and ELISA assays, the loading was repeated, but with unlabelled Pam3CSK4 and at different concentrations of Pam3CSK4 (1, 5 and 10 $\mu\text{g}/\text{mL}$).

For fluorescence and confocal microscopy observations, a drop of the sample was deposited on a slide and dilute by MES addition.

Release in-vitro. The sample is centrifuged, and the deposition is re-dispersed in 1.5 mL of PBS with mild agitation. After 20, 40, 60, 90 and 120 min the supernatant is collected to measure the PL.

Cell activation. DCs were prepared as described in Chapter 6: monocytes were isolated from buffy coats from healthy blood donors and then, cultured for 5 days with GM-CSF and IL-4 in order to obtain DCs. They were stimulated with pSi-COOH microparticles loaded with different concentrations of Pam3CSK4 and with pSi-COOH microparticles and the molecule, separately, as positive controls. The degree of activation was investigated by quantifying the cytokines secreted by the DCs in the culture supernatant (IL-6, IL-12 and TNF- α) by sandwich enzyme-linked immunosorbent assay (ELISA).

The instrumentation used to evaluate drug loading and release and DCs activation are reported in Table 7.1, the relative obtained information. All the detailed experimental techniques are reported in Appendix A2.

Table 7.1 Characterization techniques and related information

Technique	Measurement information
Fluorescence / Confocal microscopy	Particle loading tests
ELISA assay	Cell activation (immune response)
Spectrofluorometer	Release in-vitro

7.3. Drug loading: fluorescence and confocal microscopy

As above discussed, fluorescence and confocal microscopy are very useful to verify if Pam3CSK4-R is loaded onto the pSi microparticles. In fact, being rhodamine-labelled, the molecule is fluorescent, and its position is easily traced. Furthermore, being also pSi microparticles photoluminescent, they are both visible by confocal microscopy. Figure 7.3 shows the images obtained by fluorescence microscopy: optical microscope image of the pSi microparticles (panel a) and fluorescence signal coming from rhodamine (panel b).

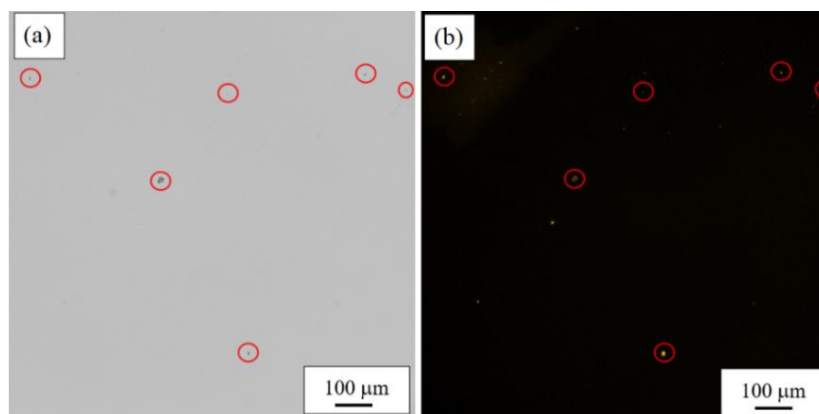


Figure 7.3 pSi microparticles after Pam3CSK4-R loading: optical microscope image of the microparticles (panel a) and fluorescence image relative to rhodamine (panel b). The points of microparticles and fluorescence co-presence are circled.

Since the pSi sample under investigation (pSi-COOH_2, see Chapter 3) has an average size of about one μm , the image in panel a (100 μm scale) only shows the largest microparticles. For the few pSi microparticles that can be detected, we can observe a quite good superposition with the fluorescence image of rhodamine, points highlighted with red circles.

To better visualize the superposition of pSi microparticles and rhodamine fluorescence of Pam3CSK4-R and to verify its effective loading, confocal microscopy was performed on the pSi-loaded sample, after the centrifugation. The images are reported in Figure 7.4 (100 μm scale) and 7.5 (25 μm scale).

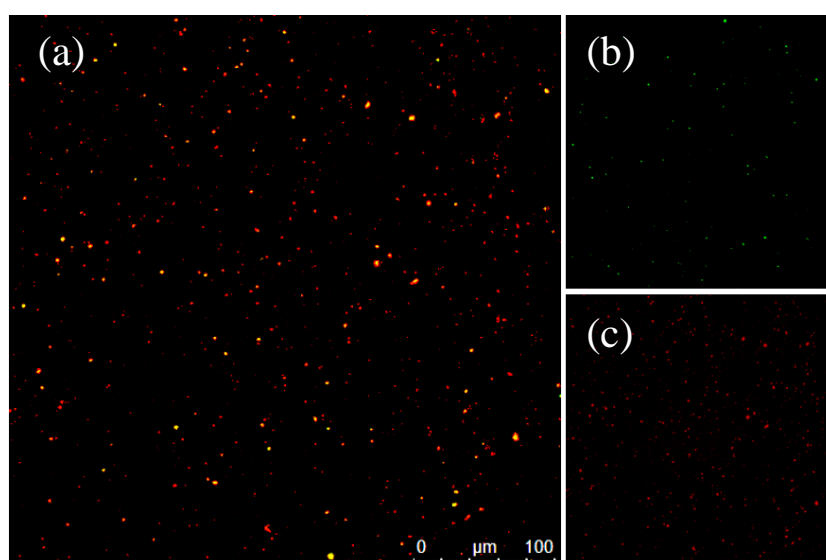


Figure 7.4 Confocal microscopy images of merged (panel a) and separate signals (panel b and c) of pSi microparticles, upon 405 nm excitation (in green) and rhodamine, upon 555 nm excitation (in red) at 100 μm scale.

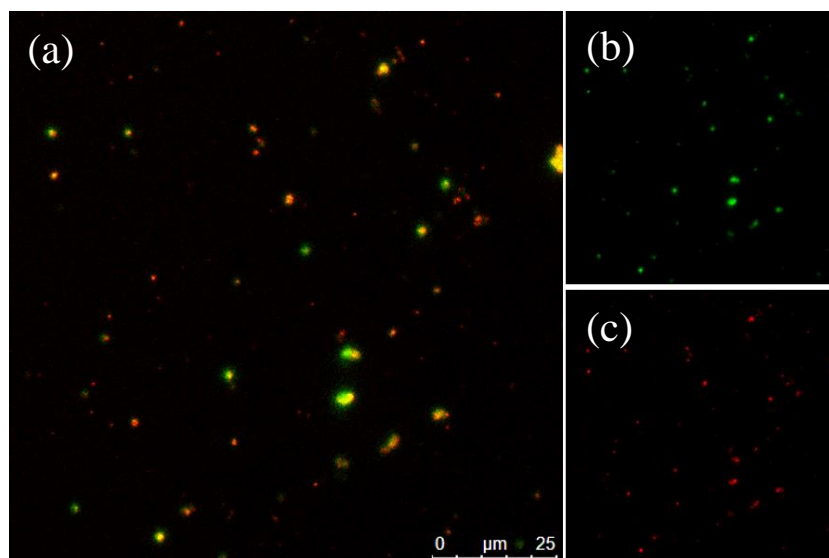


Figure 7.5 Confocal microscopy images of merged (panel a) and separate signals (panel b and c) of pSi microparticles, upon 405 nm excitation (in green) and rhodamine, upon 555 nm excitation (in red) at 25 μm scale.

The merging of the photoluminescence of pSi microparticles (green signals - excitation at 405 nm and emission at 650 nm) and of rhodamine (red signals - excitation at 555 nm and emission at 578 nm) shows a good overlapping. This is a preliminary proof of Pam3CSK4 efficient loading on pSi-COOH microparticles.

The presence of red points (relative to the molecules) with no correspondent green point could be due to the signal intensity of pSi that is too low to be detected. It is to be noted, in fact, that the quantum yield is about 70 % for rhodamine and only a few % for pSi.

7.4. Drug release in-vitro

For drug release tests in-vitro, after the last centrifugation, the sample was resuspended in 1.5 mL PBS (time 0 in Figure 7.6 (b)) and then, the PL relative to rhodamine in the supernatant was measured at set times to determine the release rate. Figure 7.6 (a) shows the excitation and emission spectra of Pam3CSK4-R: excitation peaked at 555 nm and emission at 578 nm. The release rate of this system was determined and is reported in Figure 7.6 (b).

First, the calibration curve is needed to have a correspondence between the measured PL intensity and the molecule concentration: it is reported in the inset of Figure

7.6 (b) and it is done by measuring the PL intensity at known values of molecule concentration. Then the intensity of the supernatant collected at set times was measured and converted to Pam3CSK4 concentration via the calibration curve.

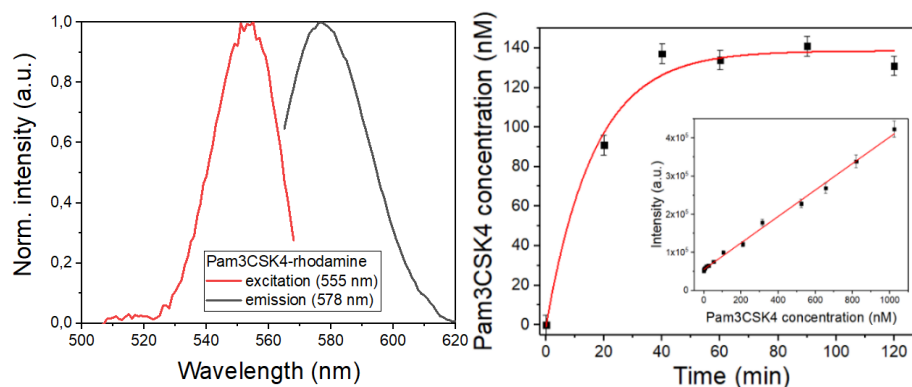


Figure 7.6 Normalized excitation (PLE) and emission (PL) spectra of Pam3CSK4-R (panel a). Determination of the release rate: Pam3CSK4-R concentration measured at set times. In the inset, the calibration curve to pass from PL intensity (of rhodamine) to Pam3CSK4-R concentration is reported. (panel b)

From this graph we can observe that at about 40 min, the quantity of released molecule reaches a plateau, hence no more molecules can be released to the medium. These preliminary result needs further tests, to better understand the feasibility of pSi microparticles for controlled delivery of vaccine adjuvants.

7.5. Drug delivery and cell activation

To assess the cellular uptake, DCs were stimulated by Pam3CSK4 loaded on pSi microparticles and by single Pam3CSK4 or pSi microparticles. The TLR agonist was loaded at different concentrations on pSi-COOH microparticles to evaluate the dose-dependence of DCs activation; pSi-COOH microparticles and the Pam3CSK4 alone were added to the cells as controls. A quantity of 50 $\mu\text{g}/\text{mL}$ of pSi-COOH microparticles (with and without drug) was used to stimulate the DCs.

The effect of the DCs stimulation was qualitatively examined by optical microscope (Figure 7.7) and quantitatively assessed by ELISA assay: the release of cytokines (specifically IL-6, IL-12, TNF- α , which are involved in the triggering of the immune response) has been analysed.

7.5.1. Optical analysis

In Figure 7.7 the optical microscope images of DCs without microparticles (panel a) and upon incubation with Pam3CSK4 (panel b), pSi-COOH (panel c) and pSi-COOH loaded microparticles (panel d) are shown, for qualitative considerations.

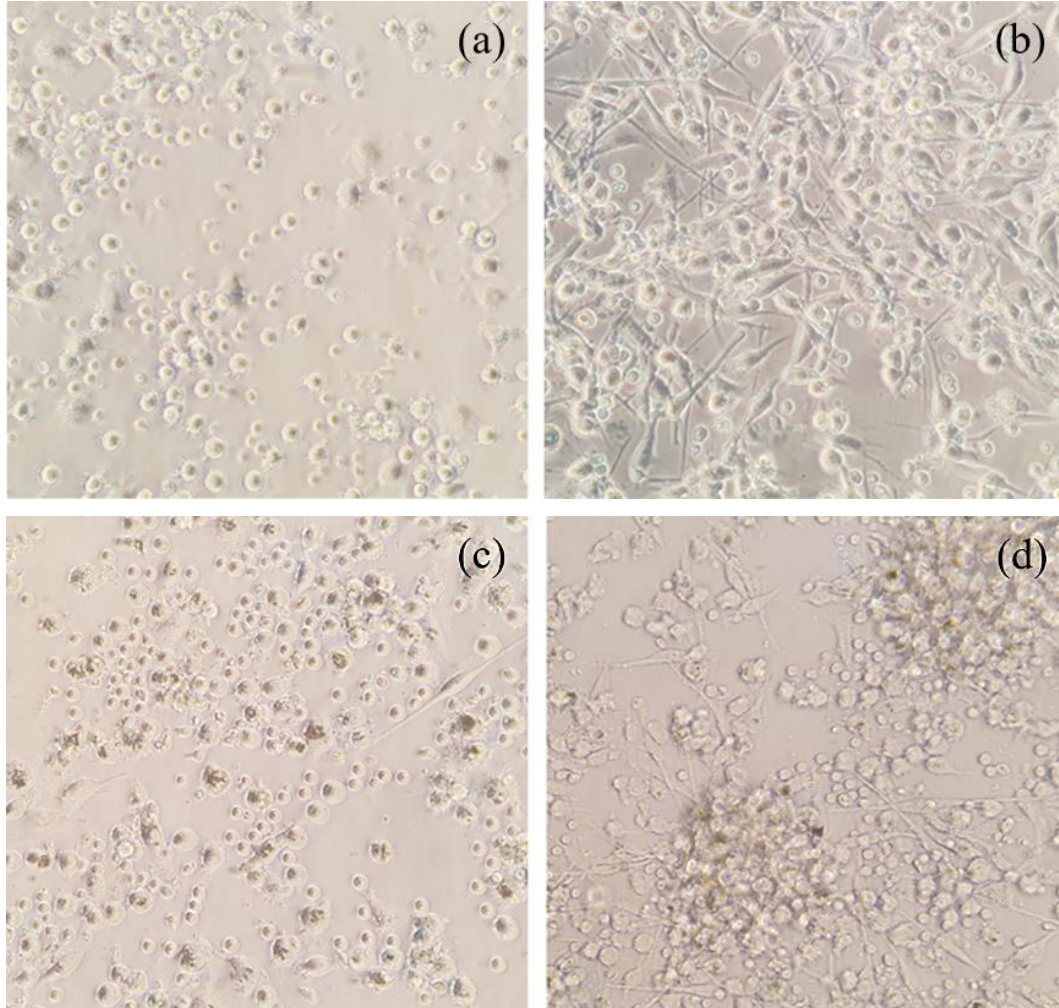


Figure 7.7 Optical microscope images of DCs (panel a), after the incubation with Pam3CSK4, 10 μ g/mL (panel b), pSi-COOH microparticles, 50 μ g/mL (panel c) and pSi-COOH loaded with 5 μ g/mL Pam3CSK4 (panel d).

Figure 7.7 (a) shows that the cells are well distributed and round-shaped, indicating that they are not activated. As expected, also upon pSi-COOH microparticles challenge no cell activation (see panel c) is observed. In fact, this material is not immunogenic, as it was demonstrated in Chapter 6. Differently, both in the positive control (i.e. the stimulation with 10 μ g/mL Pam3CSK4 - panel b) and after the injection

of the pSi-COOH loaded microparticles (panel d), the dendritic cells are activated, as it can be deduced from their elongated shape.

7.5.2. ELISA assays

The DCs stimulation was quantitatively evaluated by ELISA assays on culture supernatants, by detecting the quantity of released cytokine by the DCs. We monitored the presence of IL-6, IL-12 and TNF- α , that regulate both the innate and the adaptive immunity. The stimulation by Pam3CSK4, pSi-COOH and loaded pSi-COOH microparticles are compared and the number of released IL-6 (panel a), IL-12 (panel b) and TNF- α (panel c) are reported, in Figure 7.8.

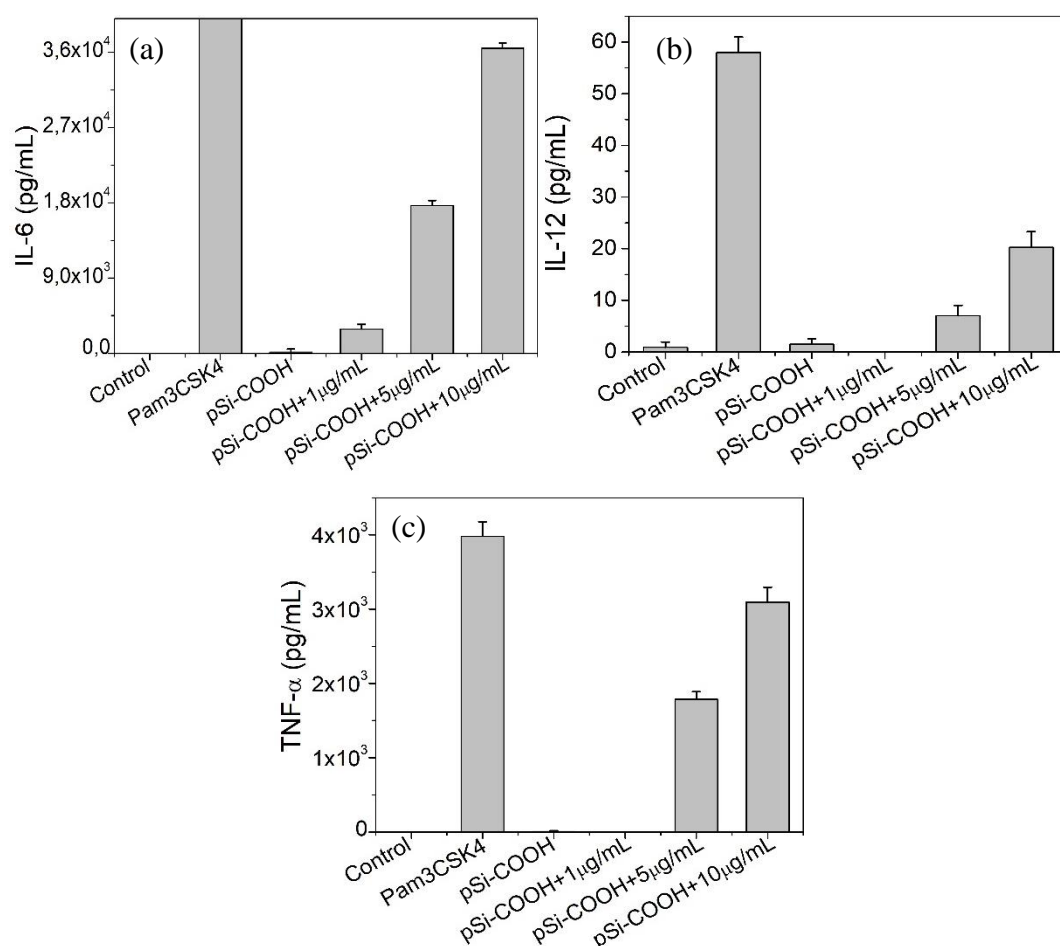


Figure 7.8 Evaluation of IL-6 (panel a), IL-12 (panel b) and TNF- α (panel c) cytokines secretion by DCs, upon incubation with Pam3CSK4, pSi-COOH microparticles and pSi-COOH microparticles loaded with different concentrations of Pam3CSK4. Ctrl refers to the DCs without stimulation.

As expected and proved in Chapter 6, we can observe that there is no release of cytokines after the incubation with bare pSi-COOH microparticles, meaning that this material is not *per se* immunogenic. Conversely, cytokine release can be observed after 10 µg/mL Pam3CSK4 stimulation (i.e. the positive control). Very interestingly, the challenge of DCs with Pam3CSK4-loaded pSi-COOH microparticles shows a dose-response effect, demonstrating a clear dependence between the concentration of Pam3CSK4 loaded on microparticles and the amounts of secreted cytokines. This effect was observed with all the investigated cytokine concentrations.

These preliminary results prove the effectiveness of the Pam3CSK4 loading on the pSi microparticles, that alone were unable to stimulate the DC activation (i.e. the release of the cytokines), and show that the cytokine release depends on the amount of loaded molecule. Further studies have to be addressed towards the quantification of the actual concentration of loaded molecules, to verify if, as it seems, the association to pSi microparticles potentiates the effect of the Pam3CSK4 and enhances the TLR agonist-dependent immune response. In fact, it is conceivable that Pam3CSK4 delivered by the microparticles could be more effective than the soluble molecule in DC stimulation.

7.6. Conclusions

In this chapter, we studied the exploitability of pSi microparticles as vaccine adjuvant carrier in perspective of immunotherapy.

We selected Pam3CSK4, a TLR 1 and 2 agonist present on DCs membrane, able to regulate the immune response. The molecule was rhodamine-labelled in order to render it visible by confocal microscopy and to verify its loading on pSi microparticles:

- we observed that an interaction between the positively charged Pam3CSK4 and the negatively charged pSi occurred, as proved by fluorescence and confocal microscopy
- we performed preliminary drug release test in-vitro, i.e. PBS at 7.4 pH, finding that after about 40 min no more molecules are released to the medium

- we performed preliminary cell activation tests by incubating the loaded microparticles with DCs. The activation of DCs has been evaluated by optical microscopy and cytokine release quantification. We observed a dose-response release of IL-6, IL-12 and TNF- α by DCs treated with pSi microparticles loaded with different Pam3CSK4 amounts, thus proving the effectiveness of the loading.

Next work is addressed towards the quantification of the actual concentration of loaded molecules, to better evaluate the pSi microparticles ability, in synergy with TLR agonists, to enhance the immune response activation. The properties of pSi microparticles as a photothermal agent could be exploited to have a synergic action between immunotherapy and PTT (photothermal therapy), in order to boost the effectiveness of cancer immunotherapy. Moreover, by decorating pSi microparticles loaded with Pam3CSK4, together with ligands of molecules expressed on the DC surface, it could be possible to specifically target DCs. In this way, the DC isolation from the patient and the subsequent re-inoculation after activation can be avoided, and particles can be directly injected into the patient's body.

CHAPTER 8

pSi INFILTRATION WITH MAGNETIC NANOSPHERES

As discussed in Chapter 1 and 2, porous silicon microparticles are promising as a theranostic agent, because of biocompatibility, porosity and photoluminescence at room temperature, thus being a drug carrier traceable in-vitro and in-vivo. The overall target of this project is to realize a wide-ranging tool for theranostics, by adding other therapeutic and diagnostic properties. So far, we proved that:

- *pSi microparticles are biocompatible, neither toxic, nor activator of human dendritic cells immune response system*
- *organic or inorganic coatings are sufficient to stabilize the PL emission properties in aqueous media for several months so that pSi microparticles can be traced by fluorescence imaging*
- *due to the huge porosity pSi microparticles could be used to load and release drugs and immune adjuvants.*

Along this direction, we aim at adding another important functionality to this system: we focus on the possibility of adding magnetic properties to the pSi microparticles. In such a way, functionalized pSi would be traceable also by MRI (magnetic resonance imaging).

For this purpose, pSi microparticles were decorated with magnetic nanospheres. The infiltration procedure has been optimized during the last part of the PhD work and the produced samples have been characterized to determine their structural and magnetic properties.

The subject of the chapter is briefly summarized in the table:

<i>Problem</i>	<i>Solution</i>
<i>Addition of magnetic properties</i>	<i>Infiltration of magnetic NPs</i>

8.1. Magnetic resonance imaging

8.1.1. Magnetic principles and techniques

MRI is a powerful diagnosis technique because it is non-invasive, it is characterized by high resolution, deep penetration, soft tissue contrast and does not use ionizing electromagnetic radiation, but it employs RF (radiofrequency) signals in an external magnetic field. In particular, it uses the nuclear magnetic resonance (NMR) signals, coming from the protons, to generate pictures of the anatomy and of the physiological process of the body.

The NMR signal is the response to the RF frequency of the nuclei present in the sample under investigation, most of which are hydrogens in the case of the human body. When these magnetic dipoles are placed in an external magnetic field B_0 , they tend to align in its direction (both parallel and anti-parallel), thus producing a weak net magnetization in the B_0 direction, and precessing (tilting of the spin axes) at a frequency (Larmor frequency: $\nu = \gamma B$) that is characteristic of each atom. When the spins are excited at this frequency (by RF radiation), the hydrogen atoms tend to precess with the same phase, thus generating a magnetization vector, which rotates at the Larmor frequency on the plane perpendicular to B_0 vector. The turning-off of the RF signal generates two types of protons relaxation, which cause a variation of the magnetization, as shown in Figure 8.1:

- Longitudinal relaxation time (T_1 – spin-lattice), which indicates the time needed for the protons to return parallel to the B_0 direction
- Transversal relaxation time (T_2 – spin-spin), which indicates the time needed for the protons to dephase.

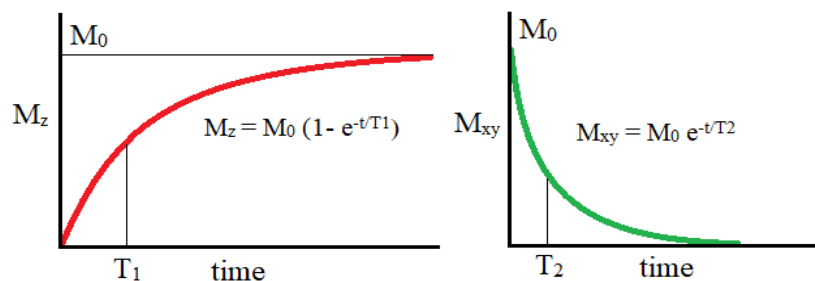


Figure 8.1 proton relaxation caused by the RF turning off: longitudinal (T_1) and transversal (T_2) relaxation times determination.

The cross-sectional or 3D images of structures and organs of the human body are obtained by detecting the NMR signal point by point in the ROI (region of interest) and plotting it in greyscale, depending on the signal intensity. To produce an image, both the signal intensity and the position where it originated are needed: gradient coils in the three dimensions (x, y and z) are used for this purpose. They cause a local variation (linear in space) of the external magnetic field B_0 that acts on the protons. Since the resonance frequency depends on the magnetic fields, it is possible to excite selectively the protons in different position by proper RF signal.

The produced images have high spatial resolution and contrast between different soft tissues, because of the sensitivity to water molecules (i.e. protons) concentration,¹⁹⁶ but also to their relaxation times, which allows distinguishing different soft tissues. To further increase the contrast among the tissues and thus the diagnostic sensitivity, nanoparticles and metal complexes with magnetic properties are widely employed.^{197,198} Two classes of contrast agents (CAs) are usually used to shorten the relaxation times thus enhancing the contrast of the image:¹⁹⁹

- positive contrast agents, for example, paramagnetic gadolinium, which shorten the longitudinal relaxation times T_1 , thus brighten the image
- negative contrast agents, such as superparamagnetic iron oxides (SPIO), which darken the image by acting on the transversal relaxation time T_2 .

Every contrast agent is characterized by a certain relaxivity: r_1 for materials acting on T_1 values and r_2 for materials acting on T_2 values.²⁰⁰ They can be obtained by a linear fit of the relative relaxation rate as a function of the contrast agent concentration, as shown in Figure 8.2.

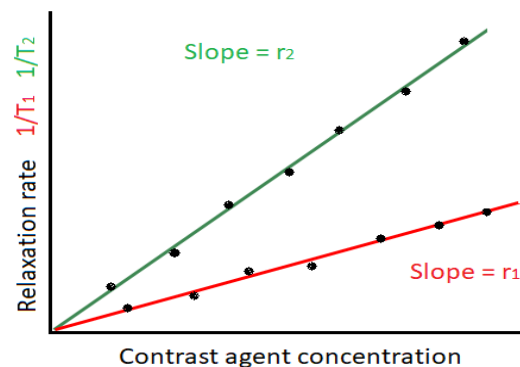


Figure 8.2 Contrast agent relaxivity obtained from the relaxation rate against the CA concentration.

The CAs can be classified as a function of the magnetic properties: paramagnetic and superparamagnetic. Paramagnetic ions, including gadolinium (Gd^{3+}), dysprosium (Dy^{3+}) and manganese (Mn^{2+}), are water-soluble; iron ions (Fe^{2+} and Fe^{3+}) are superparamagnetic. CAs with different chemical compositions are have been widely studied: small paramagnetic ion chelates, where a metal ion is bound to a large molecule,²⁰¹ macromolecules labelled with paramagnetic chelates,²⁰² micelles or liposomes containing magnetic ions.²⁰³

8.1.2. Magnetic nanoparticles

There is a research field that deals with the synthesis of nanoparticles for MRI applications. Among them, there are paramagnetic Gd-based NPs²⁰⁴ or superparamagnetic particles, for instance, maghemite (Fe_2O_3) or magnetite (Fe_3O_4) NPs with different sizes and coatings.²⁰⁵ Gadolinium cannot be employed in its ionic form, because it accumulates in bones, liver or spleen and has relatively high toxicity. Therefore, it has to be chelated to form more stable and safe complexes, which are the most common MRI contrast agents approved and used in clinics.²⁰⁶ On the contrary, SPIONs (SuperParamagnetic Iron Oxide Nanoparticles) are very fascinating, due to their biocompatibility beyond their strong magnetic properties.¹⁹⁶ Moreover, the reason to prefer SPIONs among other magnetic nanoparticles for MRI application is the total disappearing of the magnetic excitation after turning-off the external magnetic field. This is an important property for a tool exploitable in biomedicine.^{207,208} SPIONs are studied as contrast agents, since they can modify the relaxation time of the water molecules they interact with^{209,210} and specifically, they are negative contrast agents, hence increase the contrast by darkening the image.

Magnetic nanoparticles are usually coated and functionalized to protect them and avoid degradation²¹¹ by PEG (polyethylene glycol),²¹² but also by PLGA, chitosan, dextran, other polymers²¹³ and silica.²¹⁴ Some studies were also performed to use the magnetic nanoparticles as a coating or as a payload in porous materials. Some studies reported the infiltration of iron oxide NPs in porous silicon,²¹⁵ where the microparticles were placed in an aqueous solution containing magnetite NPs, that infiltrated in the porous structure and were trapped by means of a thermal oxidation/dehydration procedure. This procedure was needed to further load the magnetic

pSi microparticles with a drug and deliver it under the control of a magnetic field. In another case, the magnetite nanoparticles were anchored to mesoporous silica nanoparticles²¹⁶ by a boronate esters linker: this pH-responsive carrier is preferentially delivered to low pH tissues, such as tumour tissues. SPIONs are generally shielded with organic polymers to protect them from being cleaved in the circulation,²¹⁷ while the use of a porous silicon matrix could avoid this need.

Concerning this thesis chapter, we investigated the opportunity to decorate the functionalized luminescent pSi microparticles with magnetite (Fe_3O_4) nanoparticles, to be observable also by MRI technique. After a review of the state of the art in this field, the choice fell on very small (about 5 nm size) SPIONs (Superparamagnetic iron Oxide Nanoparticles). This allows the infiltration in large quantity in the pores of our pSi microparticles samples, which, as evaluated in Chapter 3, have a dimension of few tens of nanometres and has a high surface-to-volume ratio.

Beyond the very small dimension, the SPIONs (e.g. the magnetic material) has been selected for the high magnetic susceptibility, which allows a stronger and more rapid response to an external magnetic field. In particular, we chose commercial magnetic nanoparticles, in order to begin with more applicative and reproducible experiments. We characterized the purchased SPIONs and evaluated the way pSi and SPIONs could interact, by an appropriate functionalization. In fact, pSi microparticles present a negative surface charge (see Chapter 3), because of the COOH groups, and also the SPIONs are surprisingly negatively charged, differently from what declared in the datasheet (see next chapters for more details).

8.2. Infiltration of SPIONs within pSi microparticles

The pSi samples functionalized with COOH groups were prepared according to the procedure described in Chapter 3.

The commercial SPIONs were purchased from Sigma-Aldrich (concentration: 5 mg/mL in water, magnetization > 25 emu/g at 4500 Oe, average particle size: 5-7 nm) and diluted in PBS and in water to perform the experiments. The cyclohexane diamine ((\pm)-trans-1,2-Diaminocyclohexane), used for the SPIONs functionalization was purchased from Sigma-Aldrich.

The experimental details are reported in Appendix A1 and a summary of the techniques and relative information obtained is reported in Table 7.1.

Table 7.1 Characterization techniques and related information

Characterization	Technique	Measurement information
Surface	Raman	Vibrational modes of molecules
	DLS	ζ -potential
Structural	DLS	Average dimension
	S/TEM/EDS	Morphology, dimension, porosity and elemental composition
Magnetic	MRI	Relaxation times

The SPIONs and the decorated pSi microparticles were investigated by S/TEM coupled to EDS for the elemental, structural and morphological analysis, by Raman spectroscopy to investigate the vibrational modes of the molecules, by DLS to determine the average size and surface charge and by MRI for the magnetic characterization and determination of the relaxivity.

The functionalization of the purchased magnetic nanoparticles and their characterization were an important part of the PhD thesis. The work was performed at the University of Verona, with the instrumentation of CPT (Centro Piattaforme Tecnologiche). The electron microscopy observations for the structural analysis were done at the Department of Industrial Engineering of the University of Trento in collaboration with dr. Gloria Ischia. The magnetic properties evaluation was performed in collaboration with Prof. P. Marzola and M. Gerosa at Department of Morphological-Biomedical Sciences, Section of Anatomy and Histology of the University of Verona.

8.2.1. SPIONs functionalization

Being the crucial point of the work the addition of magnetic properties, we evaluate the best way to decorate the surface of the pSi-COOH microparticles with the purchased magnetic nanospheres (i.e., the SPIONs).

As shown in details in the following, SPIONs were found to have a negatively charged surface instead of the supposed neutral surface declared in the datasheet.

To fix this problem, we thought to functionalize the SPIONs surface with a molecule bearing at least two positive charged groups, to be a connection between the magnetic and the pSi negatively charged surface. With this purpose, we chose a cyclohexane diamine, whose chemical structure is reported in the left part of Figure 8.3. Some HCl was added to protonate it, which means to let the terminal amine molecules (NH_2) to become positive (NH_3^+) as shown in Figure 8.3.

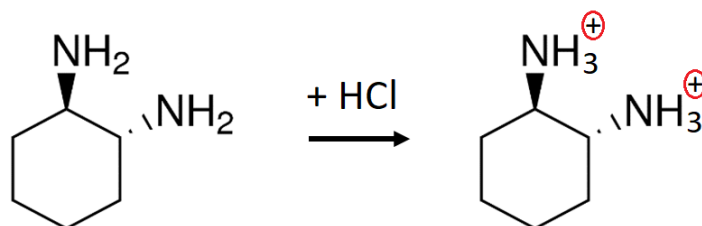


Figure 8.3 Cyclohexane diamine molecule and protonation of the NH_2 groups.

Then, the protonated cyclohexane diamine was added to the SPIONs, having a concentration of 0.2 mg/mL in PBS.

The idea is that the protonated molecule could connect the COOH groups present on the pSi porous surface with the negatively charged nanoparticle, as it is schematized in Figure 8.4, where a pore covered by SPIONs is represented and zoom of a portion of the pSi surface shows a representation, not in scale, of the mechanism of pSi-SPIONs interaction.

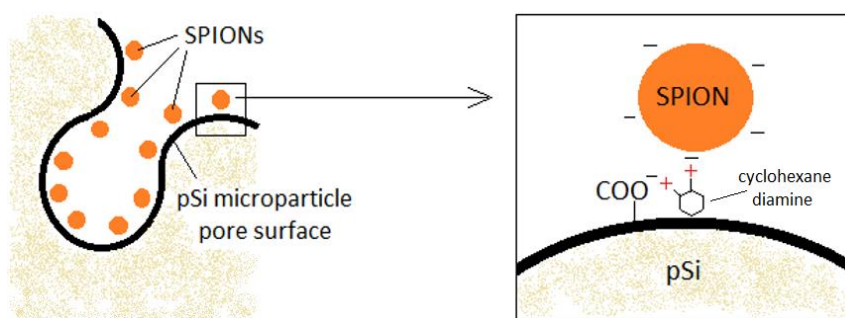


Figure 8.4 Representative portion of the pSi surface, not in scale, and pSi-SPIONs interaction.

The procedure of SPIONs surface functionalization with cyclohexane diamine was optimized by varying its concentration (from 0.3 M to 2 M) to assess the best result in terms of SPIONs dimension and ζ -potential. The optimized SPIONs functionalized sample was incubated with the 0.6 mg/mL pSi microparticle (sample pSi-COOH_2) in PBS to decorate the pSi porous surface with magnetic nanospheres,

as shown in Figure 8.5, where it is shown that the union of the functionalized SPIONs and the negatively charged pSi-COOH microparticles, produces a porous microparticles covered by the magnetic nanospheres.

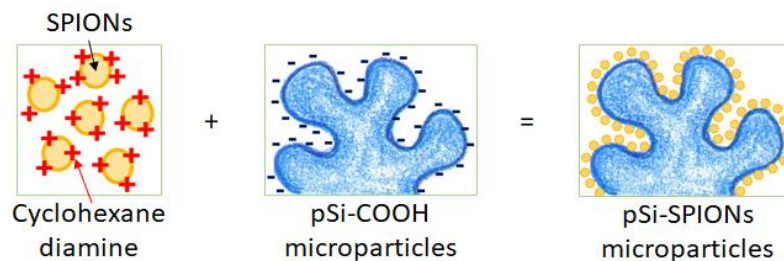


Figure 8.5 Sample preparation schematic: the yellow dots represent the SPIONs, the red cross, the positively charged cyclohexane diamine and the pSi-COOH microparticles are in blue.

The produced sample, labelled as pSi-SPIONs microparticles, was redispersed in water by centrifugation, supernatant removal and water refilling, for several times. The supernatant was conserved for further investigations, described in the results. This procedure, as described in the next paragraphs, let also evaluate if the SPIONs were actually on the pSi microparticles.

8.2.2. Functionalized SPIONs characterization

Purchased SPIONs have been characterized by means of Raman spectroscopy and Electron Microscopy.

Raman spectra of magnetite should be characterized by a low-intensity peak at about 670 cm^{-1} :²¹⁸ our measurements showed no peaks in that region but only peaks compatible with tetramethylammonium fluoride (TMAF) tetrahydrate. These features can be observed in Figure 8.6, where the Raman spectrum of SPIONs (black line) is compared with TMAF tetrahydrate (red line) from the literature and they are superimposable. This was surprising since its presence was not declared in the datasheet. A small quantity of this salt was probably added to the solution to keep the particles well dispersed for a long time in water and prevent agglomeration or precipitation of the nanoparticles, or it could be a residual of the reaction used to synthesize the SPIONs.

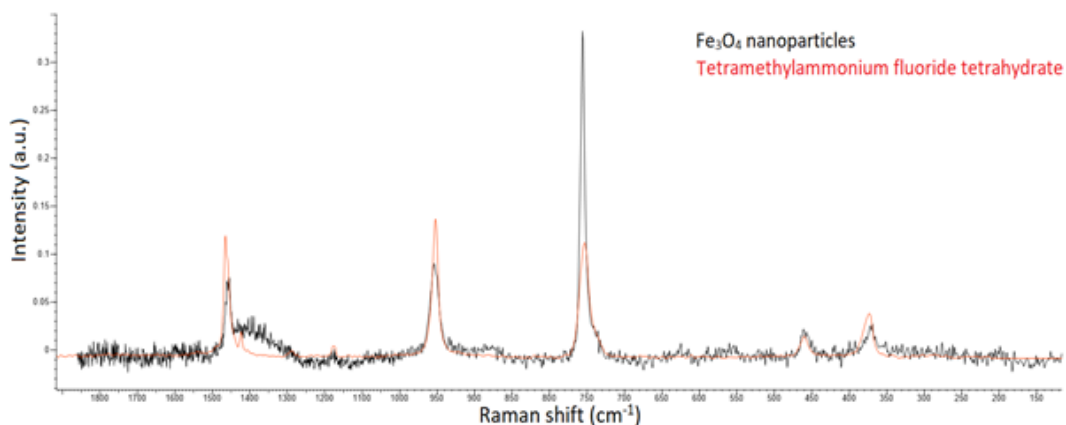


Figure 8.6 Raman spectra of SPIONs (black line) and comparison with tetramethylammonium fluoride tetrahydrate (red line) from the literature.

The structural properties of the SPIONs were examined by TEM and their size was evaluated and compared with the nominal one. Figure 8.7 shows the microparticles structure at different scales, after dilution in water, (panel a-c) and the comparison of size distribution obtained by DLS and TEM images (panel d).

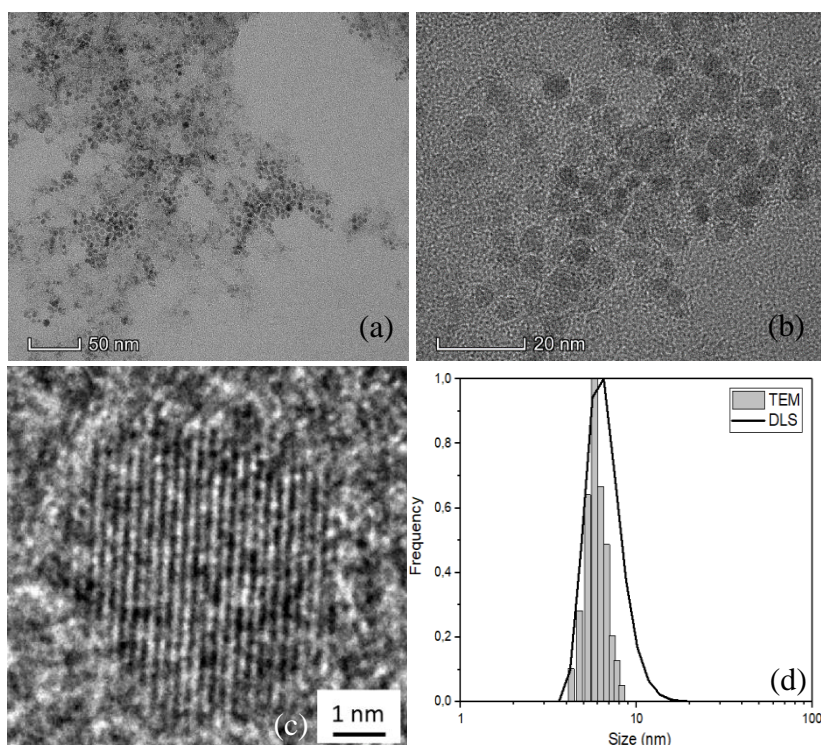


Figure 8.7 TEM images of SPIONs dispersed in water at 50 nm (panel a), 20 nm (panel b) scale and HR-TEM image of a SPION nanoparticle, where the lattice planes are visible (panel c). Comparison of size distributions obtained by DLS and TEM analysis (panel d).

The dark spots visible in the TEM image at 50 nm scale (panel a), that are similar in shape and dimension and well distributed, are the SPIONs deposited on a copper grid (i.e. the grey surface on the background). Panel b shows an enlarged portion of the first image to better appreciate the spherical shape of the nanoparticles and evaluate their dimension. Panel c is a high-resolution image of a single SPION, where also the lattice planes are visible.

The SPIONs dimension was evaluated by using *ImageJ* software and processing a fair number of TEM images. The result of this analysis leads to an average value of (6 ± 2) nm (see histogram panel d) which is in agreement with the nominal value of the purchased NPs and confirms the quite narrow size distribution. It is also consistent with the average value obtained by DLS analysis, (7 ± 3) nm. This slight overestimation is caused by the fact that DLS measurement is performed in liquid and gives an estimation of the hydrodynamic particle diameter,²¹⁹ while TEM images give a proper value since the sample is deposited on a support, dried and placed in the vacuum chamber. Moreover, TEM allows a direct estimation of the dimension, differently from DLS analysis, where it is obtained from scattering fluctuations detection.

By DLS measurements we determined the surface charge (i.e. ζ -potential) of the purchased SPIONs with a result of about -25 -30 mV, differently from the declared neutral charge, with a very broad potential distribution (see Figure 8.8 (a)). As reported in Chapter 3, also pSi microparticles have a negative surface charge (-35mV for sample pSi-COOH_2, see Table 3.5) and would thus repulse the SPIONs.

Therefore, we studied the possibility to introduce positive groups on the magnetic nanoparticles surface to avoid the repulsion: we studied and validated a functionalization with cyclohexane diamine molecules, by varying its concentration and evaluated the effect on the ζ -potential value (Figure 8.8) and on the size distribution (Figure 8.9). The ζ -potential values of the functionalized SPIONs (namely sample SPIONs_A, SPIONs_B and SPIONs_C) as the cyclohexane diamine is 0.3 M, 1 M and 2 M, respectively are reported in Figure 8.8.

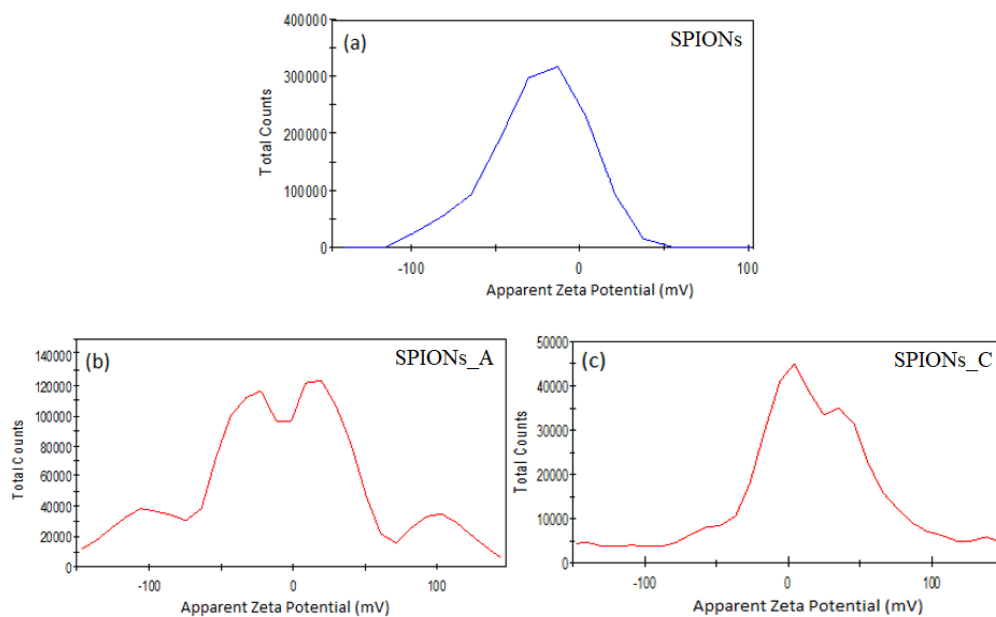


Figure 8.8 ζ -potential distribution obtained by DLS technique of diluted SPIONs (panel a) and after the functionalization with different cyclohexane diamine concentration: 1 M (panel b) and 2 M (panel c).

The size distributions of the functionalized SPIONs, with different cyclohexane diamine concentrations, are reported in Figure 8.9.

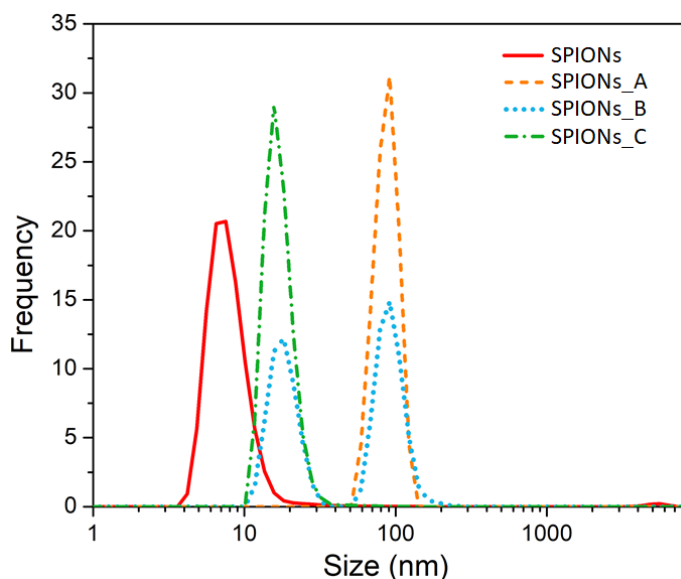


Figure 8.9 Size distribution obtained by DLS technique of diluted SPIONs and after the functionalization with different cyclohexane diamine concentration. Each distribution was determined by the media of three measurements.

It is to be noted that the size distributions are reported in terms of the number of nanoparticles, instead of intensity, that for small nanoparticles is preferable. It allows to better remove the contribution given by large particles, for instance, dust that could be present in the buffer. DLS technique measures the fluctuations in the intensity of the light scattered by the particles, having a random Brownian motion in liquids. From the correlation function of the intensity, it is possible to obtain information on the particles size: $I \propto d^6$ (I is the intensity of the scattered light and d the diameter of the spherical particle). Therefore, in the case of a bimodal distribution with the same number of large and small particles, the scattering intensity relative to the larger particles is always much higher. Thus, in the case of SPIONs (average size of 6 nm), it is better to report the results in number instead of intensity. It can be observed that the cyclohexane diamine addition causes a remarkable increase in the size distribution: from about 7 nm to about 100 nm (orange dashed line of Figure 8.9). probably, the presence of an almost equal amount of both positive and negative charged SPIONs caused their agglomeration. This is supported by the broad and peaked charge distribution (Figure 8.8 (b)) and suggests that this cyclohexane diamine concentration only allows a partial SPIONs functionalization. It is also to be considered that at low diamine concentration, each amine group present at the ends of the molecule could bind different iron oxide nanoparticles at the same time, thus producing an agglomerate of SPIONs and explaining the increase of the average size detected by DLS analysis. Differently, by increasing the concentration, it is possible that each diamine molecule (i.e. one of its terminal amine group) binds a different SPIO and exposes the other positive group, thus avoiding the agglomeration of the nanoparticles, due to the electrostatic repulsion.

In order to increase the electrostatic repulsion among the SPIONs, hence avoid agglomeration, we further increased the ratio between protonated cyclohexane diamines and SPIONs by a factor three (sample SPIONs_B, 1 M cyclohexane diamine). In this case, we observed a size distribution with two populations: a peak centred at about 80-100 nm (blue dotted line in Figure 8.9) and related to the agglomerated particles; a peak centred at about 20 nm, relative to positively functionalized SPIONs. Thus, the addition of cyclohexane diamine up to 2 M (see green line in Figure 8.9) allowed to decrease the average size distribution up to (18 ± 3)

nm, by avoiding the SPIONs agglomeration, and to obtain an averagely positive ζ -potential distribution (see Figure 8.8 (c)).

These experimental results allowed to optimize a protocol to obtain positively charged SPIONs to infiltrate the pSi-COOH microparticles. The resulting sample (namely pSi-SPIONs microparticles) was obtained after incubation of the positively charged SPIONs (i.e. sample SPIONs_C) with pSi-COOH microparticles (i.e. sample pSi-COOH_2) in PBS.

8.3. Magnetic porous silicon microparticles

8.3.1. Optical and structural characterization

Being photoluminescence a key and important property for pSi microparticles, we would investigate if it is affected by the SPIONs presence. The PLE and PL spectra of the pSi-SPIONs sample in PBS are reported in Figure 8.10.

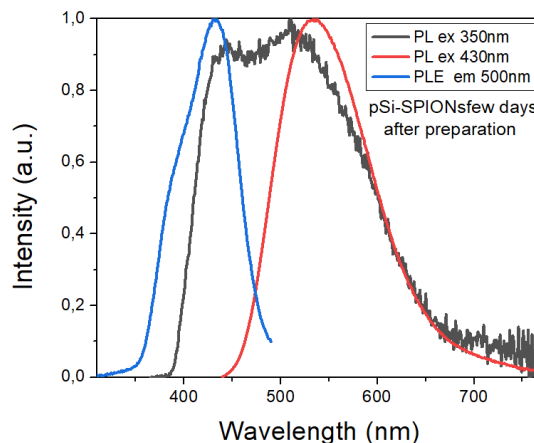


Figure 8.10 PL and PLE spectra of pSi-SPIONs in PBS. PL spectra exciting at 350 nm (black line) and 430 nm (red line); PLE spectrum with emission at 500 nm (blue line).

It is to be noted that the sample undergoes a degradation, due to the oxidation in aqueous media, which would lead to a total quenching of the optical properties in some days. The PL spectrum of the pSi-SPIONs sample shows the presence of two bands at about 500 nm and 430 nm. The latter is related to the nitrogen impurities introduced at the interface of silicon and silicon oxide. As previously reported in the case of NH_2 functionalized pSi-microparticles, which, beyond the orange-red band related to the QC effect, shows the appearance of a blue-band at about 470

nm.⁸⁸ In fact, as for pSi-NH₂ microparticles, in this case, we introduced NH₂ groups on the pSi surface by the cyclohexane diamine functionalization. To better understand the origin of the sample emission, the PLE was measured, with emission at 500 nm, finding a peak at about 430 nm. By exciting the pSi-SPIONs sample at this wavelength, we observed an intense emission at about 550 nm, that could be related to a sort of energy transfer phenomenon.

TEM and STEM analysis were fundamental to verify the effective interaction between the positively charged SPIONs and the porous silicon surface since these techniques allow to obtain the image of a single microparticle and to distinguish materials with different electron densities. The combination with EDS analysis that shows the elemental composition, consents to verify if the Fe and O elements (i.e. the SPIONs) are superimposable to the Si elements (i.e. the pSi microparticles). An example of pSi-SPIONs TEM image is reported in Figure 8.11, where also the relative EDS spectrum is reported (panel c).

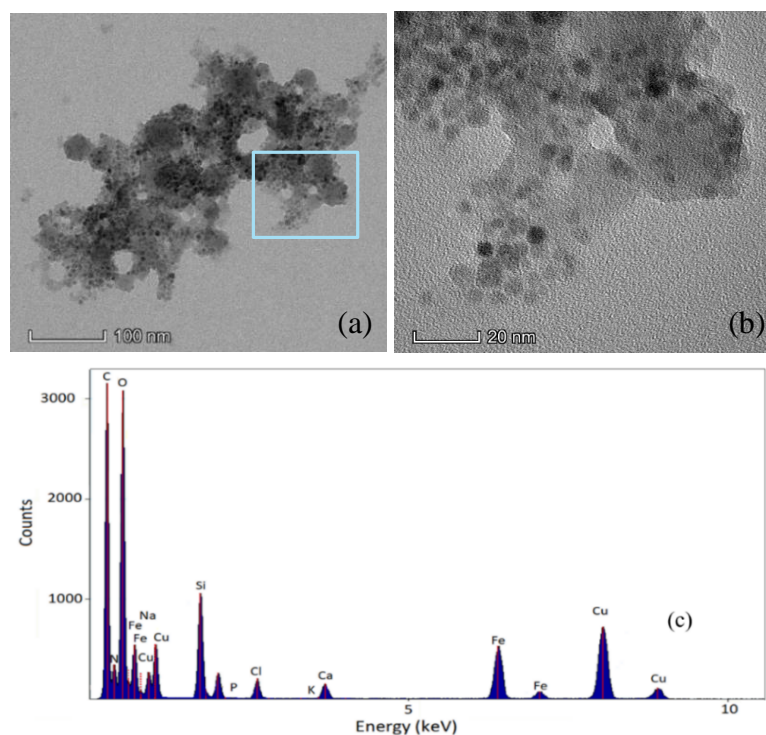


Figure 8.11 TEM images of a pSi-SPIONs microparticle at 100 nm scale (panel a), zoom of the highlighted portion, at 20 nm scale (panel b) and relative EDS spectrum (panel c).

A single porous silicon microparticle can be seen in panel (a) at 100 nm scale, a length of about 500 nm and a width of 300 nm. The darks small dots covering the

pSi surface are the SPIONs: it is worth noting that they are covering quite all the porous surface. They are even more clear in the zoomed area (20 nm scale - Figure 8.11(b)). TEM technique does not allow to obtain information on the position in depth of the different structures present in the sample. Anyway, it is possible to make some considerations relative to the darkness of structures: the darker portions reflect the dense area of the sample, thus the darker spots may be related to the presence of more than a SPION. This suggests that the SPIONs are homogeneously distributed inside the porous structure, some on the top of the sample and others deeper inside, relatively to the grey-scale colour of the small dots.

In the EDS analysis of the TEM image, we can recognize the elemental peaks related to the functionalized microparticle (Si, C, O), the Fe and N peaks relative to SPIONs and cyclohexane diamine functionalization, respectively. It is to be reminded, as done in Chapter 3 and 4, that the presence of Cu peak is due to the sample holder.

To further verify if the dark spots in the image were actually the SPIONs, the diffraction pattern of the investigated area (Figure 8.11 a) was analysed. The results are reported in Figure 8.12.

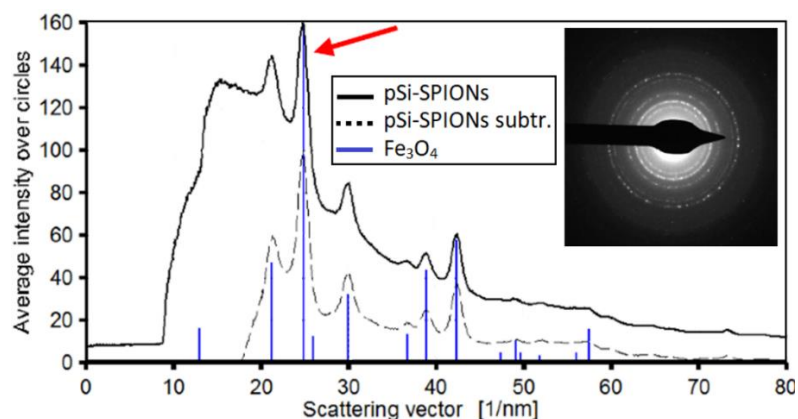


Figure 8.12 Diffraction pattern of the selected area (SAED in the figure inset) with the indexing relative to magnetite (PDF card 82-1533).

The inset of Figure 8.12 shows the SAED (selected area electron diffraction) pattern generated from the SPIONs; The ring pattern is consistent with the SPIONs dimension and indicates a random orientation of the Fe_3O_4 nanocrystal. The spectra relative to the sample pSi-SPIONs (solid black line) and that with the background subtraction (dashed black line) are compared to the indexing diffraction of magnetite

(Fe_3O_4 - blue lines). Due to the quite complete superimposition of the sample peaks with the reference ones, we can state that the measured pattern is attributable to magnetite and then, the dark spots are the SPIONs.

Bright-field (BF) and dark field (DF) TEM images of a pSi-SPIONs single microparticle are reported in Figure 8.13 (a) and (c), respectively. Panel (b) shows a dark field image recorded by using electrons relative to the (3 1 1) reflection peak (pointed out with an arrow in Figure 8.12) of the magnetite spectrum. By selectively “excite” the iron oxide NPs (i.e. the bright dots of panel b), it is possible to verify that the bright dots are actually the SPIONs made of Fe_3O_4 and to better appreciate their distribution and size inside the pSi microparticle, but losing information on the other parts of the sample.

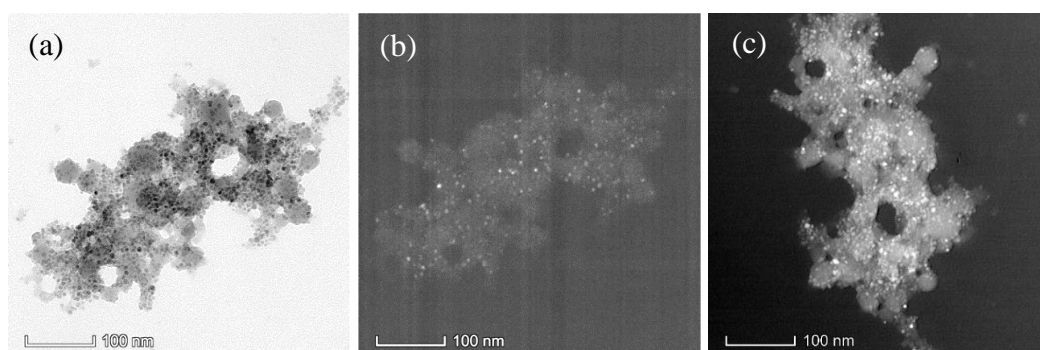


Figure 8.13 Bright image (panel a) and dark TEM images (panel b and c) of a single pSi-SPIONs microparticle.

In order to check if the buffer medium could play a role in the attachment of the SPIONs, we redisperse the pSi-SPIONs microparticles in water by several washings (i.e. centrifugation, removal of the supernatant and refill with freshwater). This procedure was also useful to remove the SPIONs present in solution, that did not infiltrate the porous structure. Thus, TEM observations were performed and the comparison between the sample dispersed in PBS and water is reported in Figure 8.14. The comparison of TEM imaging of pSi microparticles decorated with SPIONs in PBS (panel a) or water (panel b) shows no substantial difference. In both the images, the SPIONs are present and their morphology is not modified. It is worth noting that the presence of the PBS salts gives more contrast to the image, and the SPIONs are more visible.

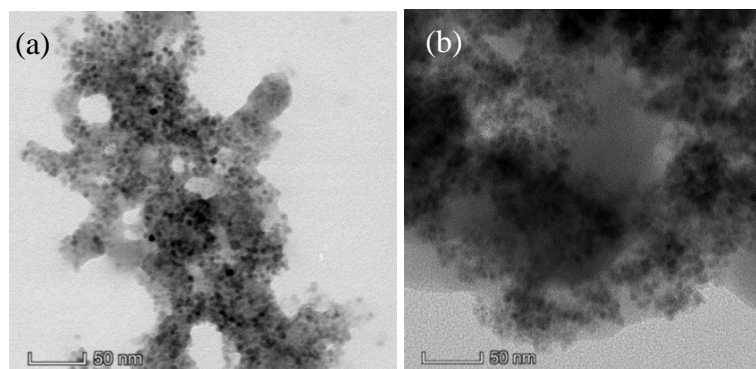


Figure 8.14 TEM images of a representative pSi-SPION at 50 nm scale in PBS (panel a) and water (panel b).

To get the evidence that no SPIONs were removed by the washings, TEM imaging and EDS analysis were carried on the supernatant that was removed after the centrifugation performed to re-disperse of pSi-SPIONs microparticles in water. The results of morphology and elemental composition are reported in Figure 8.15.

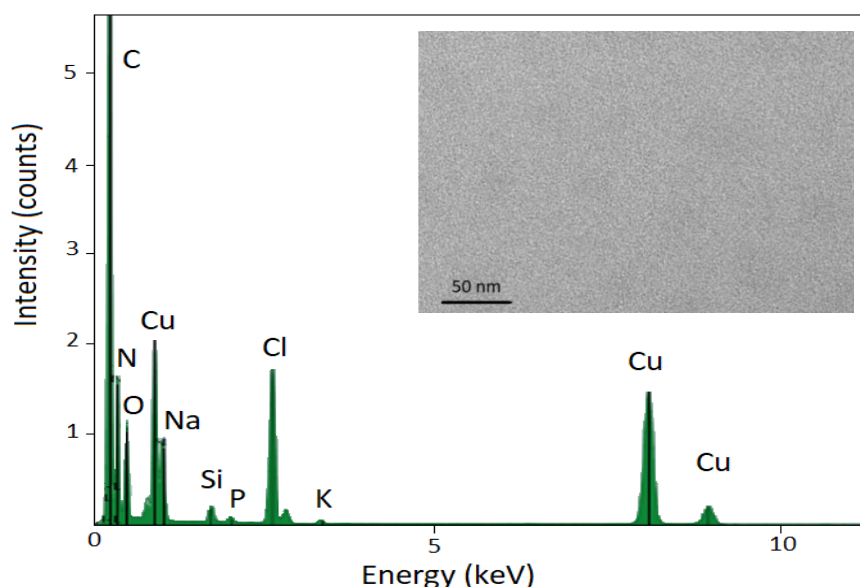


Figure 8.15 TEM image of the supernatant removed after centrifugation (panel a) and its EDS spectrum (panel b).

No presence of SPIONs was detected by TEM imaging and EDS spectra, thus confirming that the SPIONs are well electrostatically bound to the pSi microparticles and were deposited together during the centrifugation. EDS spectrum (Figure 8.15) shows neither peaks related to the porous silicon nor to iron, but only the presence of PBS salts and cyclohexane diamine residuals (peaks of Na, P, K, and Cl and of C and N, respectively).

Another verification of the SPIONs infiltration into the pSi microparticles was performed by observing the samples in STEM mode: a focused electron beam is scanned on the sample surface and allows to combine the morphological investigation with composition analysis by EDS mapping. STEM is a powerful technique to investigate the actual elemental distribution inside the material with high spatial resolution. The bright-field STEM images are reported in Figure 8.16.

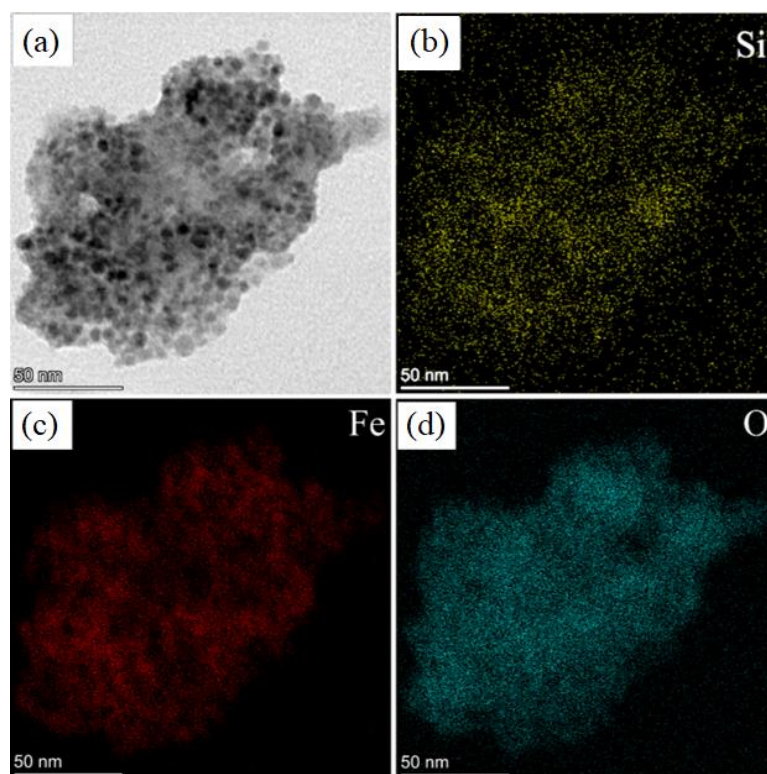


Figure 8.16 STEM (BF) images of a single pSi-SPIONs microparticle at 50 nm scale (panel a) and elemental mapping of Si (panel b), Fe (panel c) and O (panel d) elements.

By STEM it is possible to obtain the map of the image as a function of the atomic elements present. In this case, we analysed the map of Si (panel b), Fe (panel c) and O atoms (panel d): there is a quite perfect overlap between the positions of the elements, and also with the morphological image. The overlap of Fe and O distribution is quite obvious and related to the composition of the SPIONs (i.e. Fe_3O_4), while the overlap between them and Si atoms (which compose the pSi structure) means that the SPIONs are on the porous silicon surface. Moreover, the weak signal coming from the Si atoms (as compared to non-porous silicon, see Figure 8.17b in the following) is related to the pSi structure, with high surface to volume ratio, characterized by a lot of voids in a crystalline silicon matrix.

The same analysis was performed on a piece of non-porous silicon (by chance we got the image of a small non-etched piece of silicon), to investigate if there was a preferential interaction of SPIONs with porous or non-porous structures. The STEM (BF) images are reported in Figure 8.17.

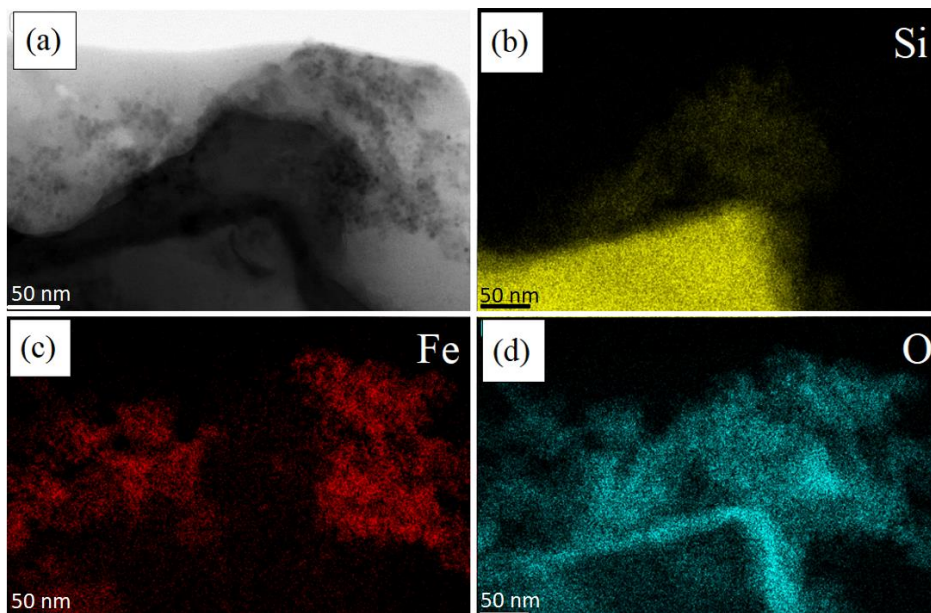


Figure 8.17 STEM (BF) images of a non-porous microparticle after SPIONs infiltration 50 nm scale (panel a) and elemental mapping of Si (panel b), Fe (panel c) and O (panel d).

A triangular portion of non-porous silicon, with a smooth surface and homogeneous colour, can be seen at the bottom of the panel (a). STEM analysis in Figure 8.17(b) shows a much dense Si structure, due to the non-porosity (see in comparison the porous microparticle in Figure 8.16(b), characterized by a lot of voids in a silicon matrix) and its surface is covered by an oxidized layer, i.e. the light blue line visible in panel (d). There is no overlap between Fe atoms position (panel c) and Si atoms position (panel b), meaning that in this case the SPIONs were not electrostatically attracted by the porous silicon: a cloud of SPIONs (position of Fe and O atoms) are accumulated at the right top of the images, but not on the silicon surface, suggesting that the Fe atoms are dispersed inside the aqueous medium.

From these observations, we can conclude that the SPIONs are not attached to non-porous silicon. But we can observe the typical SiO₂ layer of about 15 nm that is formed by the oxidation on the surface of the microparticles and therefore no more COOH (negatively charged) groups are present.

8.3.2. Magnetic properties

After proving the efficacy of the SPIONs functionalization protocol and their infiltration inside the pSi microparticles by electrostatically attraction, we investigated the magnetic properties of the “new” combined system.

We verified if the pSi-SPIONs microparticles were attracted by a simple magnet, as the first evidence of magnetic properties added to the system. Figure 8.18 shows that effectively the pSi-SPIONs microparticles are attracted by the magnet (i.e. all the microparticles in solution, highlighted by an arrow in the picture are near the small cubic magnet), differently from pSi-COOH microparticles which do not have magnetic properties, since they are not attracted by the magnet.

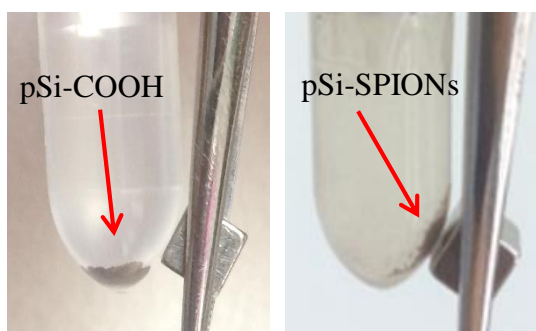


Figure 8.18 Evidence of the pSi-SPIONs microparticles magnetic properties, differently from pSi-COOH microparticles, not attracted by the magnet.

As previously introduced, the diagnostic application of SPIONs in MRI depends on the fact that they are able to modify the relaxation times of water and for this reason are used as a contrast agent, to increase the contrast between different tissues in MRI images. Therefore, MRI was employed to investigate if also pSi-SPIONs microparticles were effective in this way. To perform a quantitative evaluation on the magnetic properties after the SPIONs infiltration in the silicon pores, we investigated the magnetic parameters (i.e. the relaxivity) and compare it with the values obtained for SPIONs and pSi-COOH microparticles, alone. Both longitudinal (spin-lattice) relaxation time T_1 and transversal (spin-spin) relaxation time T_2 are determined according to the procedure reported in the introduction,²⁰⁰ upon a constant magnetic field (7 T). The longitudinal and transversal relaxation times of SPIONs, pSi microparticles and pSi-SPIONs microparticles were measured at different sample concentration. The relative relaxation rates ($1/T_i$) are reported in Figure 8.19.

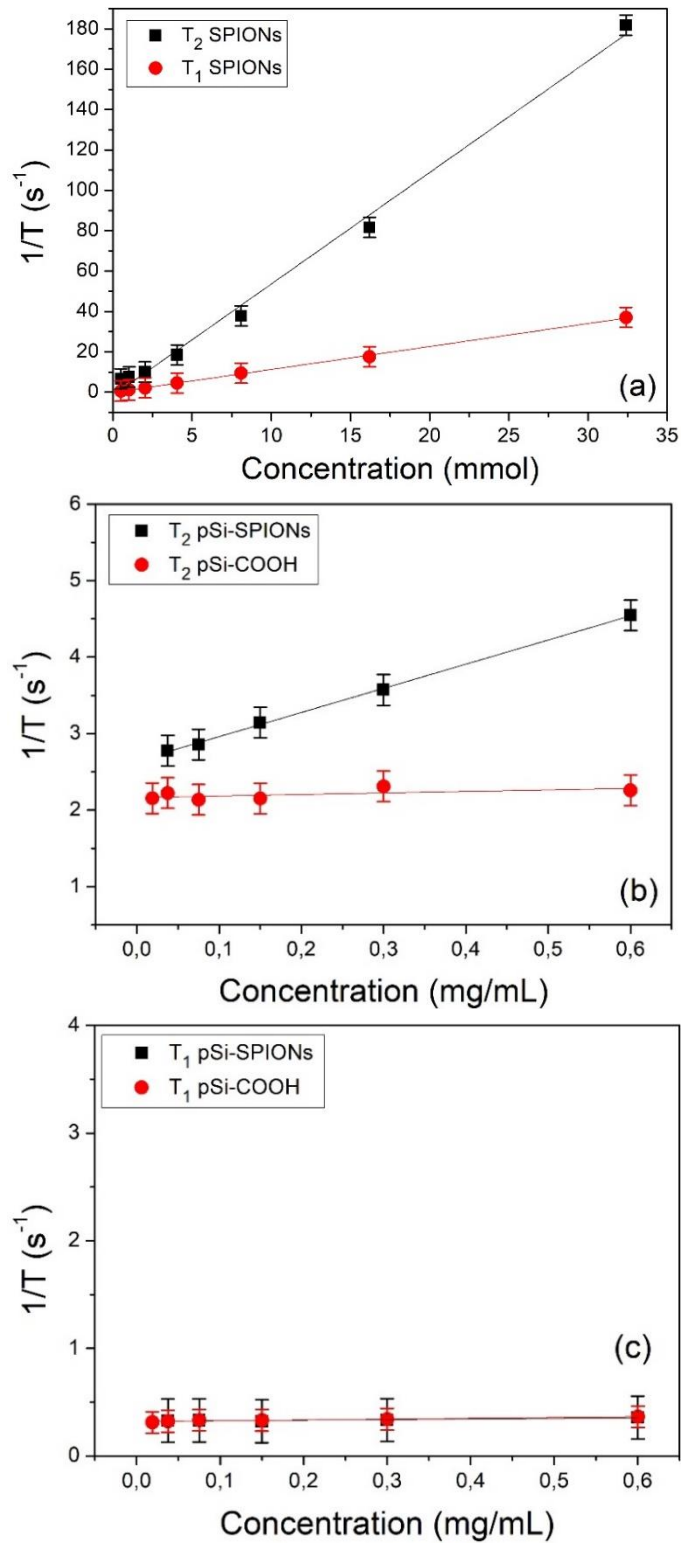


Figure 8.19 Relaxivity determination: $1/T_1$ and $1/T_2$ relaxation rates of SPIONs as a function of the iron concentration (panel a) and $1/T_2$ and $1/T_1$ relaxation rate of pSi-SPIONs and pSi-COOH microparticles as a function of the microparticles concentration (panel b and c, respectively). In a 7T external magnetic field.

Subsequently, the relative relaxivities r_1 and r_2 are extrapolated via a linear fit of the relaxation rates $1/T_i$ measured as a function of sample concentration, as described in Appendix A1, by the formula:

$$\frac{1}{T_i} = \frac{1}{T_{i,0}} + r_i \cdot c$$

From the linear fit of the data, we obtained a longitudinal relaxivity r_1 of about 1.1 (mmol)⁻¹s⁻¹ and a transversal relaxivity of about 5.5 (mmol)⁻¹s⁻¹. As expected for such nanoparticles, the transversal relaxation time is higher than the longitudinal one²⁰⁰ with an r_2/r_1 ratio of about 5. The results are almost compatible with the values found in literature,³⁸ for SPIONs smaller than 5 nm, which were characterized by a r_2/r_1 of about 12, with $r_1 \approx 0.6$ and $r_2 \approx 7.5$ with an external magnetic field of 3 T. The difference in the transversal relaxivity is due to the magnetic field intensity (in our study 7 T), which is known to reduce the T_2 value.

In fact, this kind of nanoparticles is employed as negative contrast agents (i.e. affecting the T_2 relaxation time of water surrounding the nanoparticle) to increase the darkness of the image. The decreasing of the signal intensity is due to the dipolar coupling of the magnetic moment of water and nanoparticles, thus inducing a dephasing of the spin and a shortening of the T_2 .

Moreover, it seems that the SPIONs T_2 data (panel a, black squares) can be fitted differently at lower (less than 2.5 mmol) or higher concentration. The increase of relaxation rate at higher concentration could be related to the formation of nanoparticles clusters. It is supported by the linear dependence of the relaxation time with size¹⁹⁶ and that uncoated SPIONs tend to aggregate.

Then, the relaxation efficacy of the pSi microparticles before and after the infiltration with SPIONs was investigated: transversal and longitudinal relaxation times are reported against the microparticle concentration (expressed in mg/mL) in Figure 8.19 (b and c, respectively). The relaxivity was determined via linear fit and it is 3.2 (mL/mg) s⁻¹. Concerning the transversal relaxivity r_2 (panel b) for pSi microparticles, we did not observe any variation of the relaxation rate within the experimental error by varying the microparticles concentration. After the infiltration of SPIONs, the transversal relaxivity is modified and increases as the sample concentration increases. The effect on longitudinal relaxivity T_1 is negligible for both pSi

microparticles and pSi-SPIONs samples, as it is clearly visible in panel (c), where the relaxation rate is constant at any sample concentration. In the case of pSi microparticles, we found relaxation times $T_1 \approx 3000$ ms and $T_2 \approx 450$ ms; the small decrease with respect to the relaxation times obtained for pure water ($T_1 \approx 3100$ ms, $T_2 \approx 600$ ms) could be attributable to the interaction of the spins with the microparticles, meaning that their presence accelerates the returning to the spins in the external magnetic field direction, after the removal of the RF excitation. No concentration-dependent effect is detected because the variation of the microparticles concentration does not modify further the relaxation time.

A real comparison between MRI results for the SPIONs alone (expressed in $(\text{mmol})^{-1}\text{s}^{-1}$) or infiltrated in the silicon porosity (expressed in mg/mL of pSi) was not possible, since the concentration of SPIONs that were effectively internalized by electrostatic force is not known. Even if no SPIONs were detected by TEM in the supernatant removed after the redispersion of the pSi-SPIONs in water, we investigated the supernatant by size distribution measurements. The size distribution of supernatant, pSi-SPIONs microparticles and pSi-COOH microparticles (relative to sample pSi-COOH_2, see Figure 4.3 in Chapter 4) are reported in Figure 8.20.

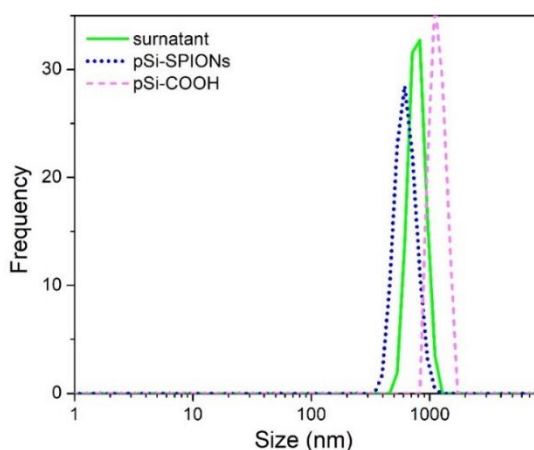


Figure 8.20 Size distribution obtained by DLS technique of the supernatant (the centrifugation performed to re-disperse of pSi-SPIONs microparticles in water – solid green line) compared to the size distribution of obtained for pSi-SPIONs microparticles (dotted blue line) and the pSi-COOH without SPIONs (dashed pink line).

It is to be noted that there is no correlation between the height of the size distribution and the concentration of material in the sample since, before every measurement,

the instrument set automatically an attenuator to decrease the signal intensity, depending on the sample concentration. Here we can observe that all the distributions are peaked at about one μm and this could suggest that some microparticles infiltrated by SPIONs could have been removed with the supernatant after the washing procedure. For this reason, we have in program to perform ICP-MS (Inductively Coupled Plasma - Mass Spectrometry) measurements, to determine the iron concentration. This would allow obtaining a relaxivity value expressed in $(\text{mmol})^{-1}\text{s}^{-1}$, to be compared with the SPIONs one.

8.4. Conclusions

In this chapter, we studied a procedure to combine magnetic properties to the well-known properties of functionalized pSi microparticles, by infiltration of iron oxide nanoparticles (SPIONs). They can easily enter the pores (about 20 nm in size) because of their small dimension (about 6 nm) and interact with the porous silicon surface by electrostatic force once opportunely functionalized by cyclohexane diamine addition.

We developed an easy (just chemical mixture), fast (only a few minutes) and cheap (very inexpensive reagents: less than 80 cents per mg of SPIONs) protocol to functionalize the SPIONs with positively charged molecules and observed and proved that:

- SPIONs have an average dimension of 6 nm and a broad surface charge distribution
- A functionalization with cyclohexane diamine was optimized and we obtained positively charged SPIONs
- The positively charged SPIONs infiltrate the porous structure of the microparticles due to the electrostatic interaction with the carboxylic groups, which was proved by means of TEM and STEM analysis
- the presence of the iron oxide nanoparticles is confirmed by the relative diffraction pattern. On the other hand, no attachment was observed in the case of non-porous surfaces

- Almost all the SPIONs remain inside the porous silicon structure, even after several centrifugations and washings
- As the first evidence of magnetic properties addition, we verified that the microparticles decorated with SPIONs are effectively attracted by a magnet, differently from pSi-COOH microparticles
- Concerning the use of pSi-SPIONs microparticles as a contrast agent in MRI, we observed some variations in the transversal relaxivity ($3.2 \text{ (mL/mg) s}^{-1}$), differently from pSi-COOH microparticles, which as expected have no magnetic properties and no effect on the orientation of the spins. The evaluation of the concentration of actual infiltrated SPIONs could be helpful to better understand the potentiality of pSi microparticles to be traced in MRI.

These encouraging new results, although they need further investigations, open the way to pSi microparticles to be used as a tracer in MRI.

CONCLUSIONS

Porous silicon microparticles potentialities and limitations were evaluated for the employment of this material as theranostics system, i.e. diagnostics, therapy and treatment. The aims of this thesis work were the overcoming of the limiting issues and the improvement of the potentialities, of pSi microparticles, in an original and effective way. The main results achieved are summarized in the following conclusions.

*In Chapter 4, we dealt with the lack of fine control on the average size and **size distribution** of the produced material, intrinsic in the top-down fabrication. An easy, fast and cheap post-functionalization treatment based on sonochemical effects was optimized in terms of duration and power density. This **ultrasonic treatment** was effective in decreasing the average dimension by fracturing the large microparticles and, more probably, by disaggregating the grouped ones. We halved the average size of the pSi microparticles from about a few μm to about 500 nm, without affecting neither the luminescent properties nor the porosity.*

*We demonstrated for the first time the possibility to stabilize the photoluminescence of pSi-COOH functionalized microparticles in biological media with an **inorganic coating** (TiO_2) by an innovative method of deposition (see results reported in Chapter 5). This technique allowed to obtain a uniform thin layer (e.g. few nm) with tuneable thickness, covering all the porous surface of the microparticles. It effectively prolonged the **PL emission stability** in biological aqueous media for more than 5 months, without modifying morphology, surface charge, average size and porosity of pSi microparticles.*

*In Chapter 6, we verified the reliability of our pSi microparticles in theranostics by investigating the cells internalization mechanism, the **cytotoxicity** and the **immunogenicity** of pSi microparticles inside the **human immune cells** (dendritic cells, monocytes and lymphocytes). We observed that the microparticles, both coated and uncoated, are internalized via a non-receptor mediated mechanism, without toxic effects, as proved by imaging and viability assays. They are still*

photoluminescent inside the cells and thus can be traced by optical imaging. Concerning the immune response and the relative release of cytokines, the pSi microparticles alone, with or without coating, did not activate the immune response, thus suggesting no immunogenic activity.

In Chapter 7, we performed preliminary vaccine adjuvants **delivery tests** in the perspective of **immunotherapy**. We selected an agonist of the toll-like receptors of dendritic cells (**Pam3CSK4**), which is an activator of the immune response. In these preliminary tests, we proved by confocal microscopy the loading of the rhodamine-labelled molecule within the pSi microparticles and performed some preliminary release trials in PBS at 7.4 pH. Cell activation experiments showed no toxic effect and an increased immune response as the quantity of loaded molecules increases, thus suggesting that the loading was effective.

In Chapter 8, the possibility to add magnetic properties to the functionalized pSi microparticles was demonstrated. We infiltrated magnetic nanoparticles (**SPIOs**), with an average dimension of 6 nm, inside the pores (about 20 nm in size), thanks to electrostatic interaction with the porous silicon surface. This was possible because we developed an easy, fast and cheap protocol to functionalize the SPIOs with positively charged molecules, to be able to interact with the negative carboxylic groups present at the functionalized pSi surface. TEM and STEM analysis proved the presence of the iron oxide nanoparticles only onto the porous and functionalized silicon structures. The optimized pSi microparticles infiltrated with SPIOs was proved to be magnetic since it was attracted by a magnet, and MRI measurements confirmed the possibility to use pSi-SPIOs microparticles as a **negative MRI contrast agent**.

In conclusion, among the several nanomaterials that are studied for theranostics, pSi microparticles stand out, particularly, for the absence of toxicity and for their intrinsic diagnostic and therapeutic assets. The interesting findings discussed in this thesis are a further fundamental step towards the exploitability of this material as a drug and vaccine adjuvant carrier, which may be traced by optical and/or magnetic resonance imaging.

MAIN RESULTS ACHIEVED

In the following, a summary of the main results achieved in this PhD thesis work that overcame the state of the art:

- *Photoluminescence stability for over 5 months in aqueous media thanks to thin (a few nm) **TiO₂** coating*
- *Absence of **toxicity and immunogenicity** up to 50 µg/mL of coated (**TiO₂**) and uncoated pSi microparticles*
- *Preliminary demonstrations of the combined effect of pSi microparticles and **Pam3CSK4** on DCs activation*
- *Easy (just chemical mixing in a simple bucket), fast (only a few minutes), cheap (very inexpensive reagents) chemical protocol to **infiltrate SPIONs** inside pSi pores for MRI*

PERSPECTIVE AND FUTURE WORK

The possibility to exploit loaded pSi microparticles as vaccine adjuvant is challenging, stimulating and the way is still to be paved. The intent is to induce a stronger antibody-mediated immunity and to improve protection against infectious diseases, for which vaccines formulations exist but are not sufficient yet. Moreover, the chance to add a ligand to the functionalized surface of pSi microparticles could have interesting potentials for targeting delivery to increase the cell/tissue selectivity and avoid unwanted toxicity. For example, hyaluronic acid (HA) is a valid choice because its receptor is highly overexpressed in certain tumour cells (pancreatic, breast and lung cancer cells) and could, therefore, accumulate in those tissues but not in healthy cells.

In perspective of immunotherapy, it could be possible to specifically target DCs by decorating with specific ligands the pSi microparticles, that carry the vaccine adjuvant. In this way, the DC isolation from the patient and the subsequent re-inoculation after activation can be avoided, and microparticles can be directly injected into the patient's body, to reach their target.

For a different therapeutic application, pSi microparticles are known to absorb in the NIR region and could, therefore, be employed to ablate the cancer cells by releasing heat after NIR excitation (PTT), while being imaged by several techniques. From the fabrication and functionalization point of view, the efficacy of inorganic TiO₂ coating opened the way for further developments. A new research path to be pursued would be the coating of the pSi microparticles by a thin layer of other oxides, such as iron oxides (to provide magnetic properties), rare earth oxides (to provide magnetic and/or to improve optical properties) and zinc (to include anti-bacterial properties) oxides. All this to provide to light-emitting pSi microparticles other functionalities thus realizing a multimodal and comprehensive system for theranostics.

Publications

E. Chistè, A. Ghafarinazari, M. Donini, V. Cremers, J. Dendooven, C. De-tavernier, D. Benati, M. Scarpa, S. Dusi and N. Daldosso, "TiO₂-coated luminescent porous silicon microparticles as a promising system for nanomedicine", J. Mat. Chem. B, **2018**, 6, 1815-1824.

E. Chistè, G. Ischia, M. Scarpa and N. Daldosso "Ultrasonication effect on size distribution of functionalized porous silicon microparticles" Mater. Res. Express **2019** 6 (7) 075006.

E. Chistè, G. Ischia, M. Gerosa, P. Marzola, M. Scarpa and N. Daldosso "Porous Si microparticles infiltrated with magnetic nanospheres for theranostics" Nanomaterials **2020** 10 463.

Conferences contributions

Conference NN17 (International Conference on Nanoscience & Nanotechnologies) 01-08 July 2017- Thessaloniki (Greece) with an oral presentation on "Inorganic coating of luminescent porous silicon by ALD technique to enhance optical stability for biomedical applications".

Conference NANOMEDICINE Rome 2018 - Rome (ISS – Istituto Superiore di Sanità) 18-20 June 2018 with a poster presentation on “TiO₂ -coated pSi microparticles for nanomedicine”.

Conference NanoMedicine 2018 International Conference and Exhibition, 23-25 October 2018 - Venice (Italy), 23 - 25/10/2018 with an oral presentation on “Titanium dioxide coating of porous silicon microparticles towards nanomedicine applications”.

Workshop Nanomedicine 2019 02-03 May 2019 – Milan (Italy) with a poster presentation on “Organic and inorganic coating of light-emitting porous silicon microparticles”.

Conference FisMat 2019 (Italian national conference on the physics of matter), 30 September 2019 – 04 October 2019 – Catania (Italy) with a poster presentation on “Porous silicon light-emitting microparticles for NanoMedicine” and oral presentation on “Light-emitting porous silicon microparticles: from fabrication to surface functionalization”.

Conference PSST (Porous Semiconductors – Science and Technology) 2020, 15 – 20 March 2020 – Lido di Camaiore (Italy) accepted abstracts: “Magnetic nanospheres within porous silicon light-emitting microparticles” and “Porous silicon microparticles for immune adjuvant delivery.

References

- ¹ K.E. Drexler, Proc. Natl. Acad. Sci. U. S. A. **78**, 5275 (1981).
- ² R.T. Collins, P.M. Fauchet, and M.A. Tischler, Phys. Today **50**, 24 (2008).
- ³ D. Guo, G. Xie, and J. Luo, J. Phys. Appl. Phys. **47**, 013001 (2013).
- ⁴ Z. Zhang, J.C. Li, and Q. Jiang, J. Phys. Appl. Phys. **33**, 2653 (2000).
- ⁵ C.Q. Sun, Prog. Solid State Chem. **35**, 1 (2007).
- ⁶ A.D. Yoffe, Adv. Phys. **50**, 1 (2001).
- ⁷ A.K. Yetisen, H. Qu, A. Manbachi, H. Butt, M.R. Dokmeci, J.P. Hinstroza, M. Skorobogatiy, A. Khademhosseini, and S.H. Yun, ACS Nano **10**, 3042 (2016).
- ⁸ T. Abitbol, A. Rivkin, Y. Cao, Y. Nevo, E. Abraham, T. Ben-Shalom, S. Lapidot, and O. Shoseyov, Curr. Opin. Biotechnol. **39**, 76 (2016).
- ⁹ R. Arvidsson, S. Molander, and B.A. Sandén, J. Ind. Ecol. **16**, 343 (2012).
- ¹⁰ D. Akinwande, N. Petrone, and J. Hone, Nat. Commun. **5**, 5678 (2014).
- ¹¹ M. Heiranian, A.B. Farimani, and N.R. Aluru, Nat. Commun. **6**, 1 (2015).
- ¹² T.J. Webster, Int. J. Nanomedicine **1**, 115 (2006).
- ¹³ S. Wang, P. Huang, and X. Chen, ACS Nano **10**, 2991 (2016).
- ¹⁴ D.-E. Lee, H. Koo, I.-C. Sun, J.H. Ryu, K. Kim, and I.C. Kwon, Chem. Soc. Rev. **41**, 2656 (2012).
- ¹⁵ S.M. Janib, A.S. Moses, and J.A. MacKay, Adv. Drug Deliv. Rev. **62**, 1052 (2010).
- ¹⁶ Y.F. Tan, P. Chandrasekharan, D. Maity, C.X. Yong, K.-H. Chuang, Y. Zhao, S. Wang, J. Ding, and S.-S. Feng, Biomaterials **32**, 2969 (2011).
- ¹⁷ F. Pene, E. Courtine, A. Cariou, and J.-P. Mira, Crit. Care Med. **37**, S50 (2009).
- ¹⁸ S.S. Kelkar and T.M. Reineke, Bioconjug. Chem. **22**, 1879 (2011).
- ¹⁹ S. Tran, P.-J. DeGiovanni, B. Piel, and P. Rai, Clin. Transl. Med. **6**, (2017).
- ²⁰ T. Lammers, W.E. Hennink, and G. Storm, Br. J. Cancer **99**, 392 (2008).
- ²¹ M. Goldsmith, L. Abramovitz, and D. Peer, ACS Nano **8**, 1958 (2014).
- ²² J.H. Sakamoto, A.L. van de Ven, B. Godin, E. Blanco, R.E. Serda, A. Grattoni, A. Ziemys, A. Bouamrani, T. Hu, S.I. Ranganathan, E. De Rosa, J.O. Martinez, C.A. Smid, R.M. Buchanan, S.-Y. Lee, S. Srinivasan, M. Landry, A. Meyn, E. Tasciotti, X. Liu, P. Decuzzi, and M. Ferrari, Pharmacol. Res. Off. J. Ital. Pharmacol. Soc. **62**, 57 (2010).
- ²³ S.K. Patel and J.M. Janjic, Theranostics **5**, 150 (2015).
- ²⁴ S. Mura and P. Couvreur, Adv. Drug Deliv. Rev. **64**, 1394 (2012).
- ²⁵ S. Marchesan and M. Prato, ACS Med. Chem. Lett. **4**, 147 (2013).

- ²⁶ A. Kumar, H.M. Mansour, A. Friedman, and E.R. Blough, *Nanomedicine in Drug Delivery* (CRC Press, 2013).
- ²⁷ J.J. Giner-Casares, M. Henriksen-Lacey, M. Coronado-Puchau, and L.M. Liz-Marzán, *Mater. Today* **19**, 19 (2016).
- ²⁸ J. Coniot, J.M. Silva, J.G. Fernandes, L.C. Silva, R. Gaspar, S. Brocchini, H.F. Florindo, and T.S. Barata, *Front. Chem.* **2**, (2014).
- ²⁹ V.P. Torchilin, *Pharm. Res.* **24**, 1 (2007).
- ³⁰ T.T.T. Nguyen, C. Ghosh, S.-G. Hwang, L.D. Tran, and J.S. Park, *J. Mater. Sci.* **48**, 7125 (2013).
- ³¹ H. Cho and G.S. Kwon, *ACS Nano* **5**, 8721 (2011).
- ³² X. Yang, J.J. Graier, I.J. Rowland, A. Javadi, S.A. Hurley, V.Z. Matson, D.A. Steeber, and S. Gong, *ACS Nano* **4**, 6805 (2010).
- ³³ P. Rungta, Y.P. Bandera, R.D. Roeder, Y. Li, W.S. Baldwin, D. Sharma, M.G. Sehorn, I. Luzinov, and S.H. Foulger, *Macromol. Biosci.* **11**, 927 (2011).
- ³⁴ A.D. Wong, M.A. DeWit, and E.R. Gillies, *Adv. Drug Deliv. Rev.* **64**, 1031 (2012).
- ³⁵ M. Karadag, C. Geyik, D.O. Demirkol, F.N. Ertas, and S. Timur, *Mater. Sci. Eng. C* **33**, 634 (2013).
- ³⁶ V.P. Torchilin, *Nat. Rev. Drug Discov.* **4**, 145 (2005).
- ³⁷ X. He, X. Wu, K. Wang, B. Shi, and L. Hai, *Biomaterials* **30**, 5601 (2009).
- ³⁸ K. Ma, H. Sai, and U. Wiesner, *J. Am. Chem. Soc.* **134**, 13180 (2012).
- ³⁹ Y.-S. Lin and C.L. Haynes, *Chem. Mater.* **21**, 3979 (2009).
- ⁴⁰ J.E. Lee, N. Lee, H. Kim, J. Kim, S.H. Choi, J.H. Kim, T. Kim, I.C. Song, S.P. Park, W.K. Moon, and T. Hyeon, *J. Am. Chem. Soc.* **132**, 552 (2010).
- ⁴¹ D.L. Huber, *Small Weinh. Bergstr. Ger.* **1**, 482 (2005).
- ⁴² M. Mahmoudi, S. Sant, B. Wang, S. Laurent, and T. Sen, *Adv. Drug Deliv. Rev.* **63**, 24 (2011).
- ⁴³ S. Santra, C. Kaittanis, J. Grimm, and J.M. Perez, *Small Weinh. Bergstr. Ger.* **5**, 1862 (2009).
- ⁴⁴ M. Das, D. Mishra, P. Dhak, S. Gupta, T.K. Maiti, A. Basak, and P. Pramanik, *Small* **5**, 2883 (2009).
- ⁴⁵ P. Huang, L. Bao, C. Zhang, J. Lin, T. Luo, D. Yang, M. He, Z. Li, G. Gao, B. Gao, S. Fu, and D. Cui, *Biomaterials* **32**, 9796 (2011).
- ⁴⁶ X. Wu, T. Ming, X. Wang, P. Wang, J. Wang, and J. Chen, *ACS Nano* **4**, 113 (2010).
- ⁴⁷ L. Vigderman and E.R. Zubarev, *Adv. Drug Deliv. Rev.* **65**, 663 (2013).

- ⁴⁸ Md. Nurunnabi, K.J. Cho, J.S. Choi, K.M. Huh, and Y. Lee, *Biomaterials* **31**, 5436 (2010).
- ⁴⁹ E. Cassette, M. Helle, L. Bezdetsnaya, F. Marchal, B. Dubertret, and T. Pons, *Adv. Drug Deliv. Rev.* **65**, 719 (2013).
- ⁵⁰ S. Akhter, M.Z. Ahmad, F.J. Ahmad, G. Storm, and R.J. Kok, *Expert Opin. Drug Deliv.* **9**, 1225 (2012).
- ⁵¹ J.T. Robinson, K. Welsher, S.M. Tabakman, S.P. Sherlock, H. Wang, R. Luong, and H. Dai, *Nano Res.* **3**, 779 (2010).
- ⁵² A. Fabbro, A. Villari, J. Laishram, D. Scaini, F.M. Toma, A. Turco, M. Prato, and L. Ballerini, *ACS Nano* **6**, 2041 (2012).
- ⁵³ L.L. Ma, M.D. Feldman, J.M. Tam, A.S. Paranjape, K.K. Cheruku, T.A. Larson, J.O. Tam, D.R. Ingram, V. Paramita, J.W. Villard, J.T. Jenkins, T. Wang, G.D. Clarke, R. Asmis, K.V. Sokolov, B. Chandrasekar, T.E. Milner, and K.P. Johnston, *ACS Nano* **3**, 2686 (2009).
- ⁵⁴ M.P. Melancon, A. Elliott, X. Ji, A. Shetty, Z. Yang, M. Tian, B. Taylor, R.J. Stafford, and C. Li, *Invest. Radiol.* **46**, 132 (2011).
- ⁵⁵ M. Ma, H. Chen, Y. Chen, X. Wang, F. Chen, X. Cui, and J. Shi, *Biomaterials* **33**, 989 (2012).
- ⁵⁶ L.-S. Wang, M.-C. Chuang, and J.A. Ho, *Int. J. Nanomedicine* **7**, 4679 (2012).
- ⁵⁷ A. Uhlir, *Bell Syst. Tech. J.* **35**, 333 (1956).
- ⁵⁸ L.T. Canham, *Appl. Phys. Lett.* **57**, 1046 (1990).
- ⁵⁹ A.G. Cullis, L.T. Canham, and P.D.J. Calcott, *J. Appl. Phys.* **82**, 909 (1997).
- ⁶⁰ V. Lehmann and U. Gösele, *Adv. Mater.* **4**, 114 (1992).
- ⁶¹ L. Canham, in *Handb. Porous Silicon*, edited by L. Canham (Springer International Publishing, Cham, 2014), pp. 3–9.
- ⁶² M.J. Sailor, *Porous Silicon in Practice* (Wiley-VCH, Weinheim, 2012).
- ⁶³ J. Salonen, M. Björkqvist, E. Laine, and L. Niinistö, *Phys. Status Solidi A* **182**, 249 (2000).
- ⁶⁴ K. Barla, R. Herino, G. Bomchil, J.C. Pfister, and A. Freund, *J. Cryst. Growth* **68**, 727 (1984).
- ⁶⁵ P. Granitzer and K. Rumpf, *Materials* **3**, 943 (2010).
- ⁶⁶ L. Canham, *Handbook of Porous Silicon* (Springer, New York, 2014).
- ⁶⁷ L. Canham, in *Handb. Porous Silicon*, edited by L. Canham (Springer International Publishing, Cham, 2014), pp. 201–206.

- ⁶⁸ C. Chiappini, E. Tasciotti, J.R. Fakhoury, D. Fine, L. Pullan, Y.-C. Wang, L. Fu, X. Liu, and M. Ferrari, *ChemPhysChem* **11**, 1029 (2010).
- ⁶⁹ L. Cheng, E. Anglin, F. Cunin, D. Kim, M.J. Sailor, I. Falkenstein, A. Tammewar, and W.R. Freeman, *Br. J. Ophthalmol.* **92**, 705 (2008).
- ⁷⁰ J. Salonen, L. Laitinen, A.M. Kaukonen, J. Tuura, M. Björkqvist, T. Heikkilä, K. Vähä-Heikkilä, J. Hirvonen, and V.-P. Lehto, *J. Control. Release Off. J. Control. Release Soc.* **108**, 362 (2005).
- ⁷¹ J.P. Rolland, B.W. Maynor, L.E. Euliss, A.E. Exner, G.M. Denison, and J.M. DeSimone, *J. Am. Chem. Soc.* **127**, 10096 (2005).
- ⁷² J. Ping and Z. Hou-zhi, *Physics Of Semiconductors, The - Proceedings Of The Xxi International Conference (In 2 Volumes)* (World Scientific, 1993).
- ⁷³ Y. Kanemitsu, H. Uto, Y. Masumoto, T. Matsumoto, T. Futagi, and H. Mimura, *Phys. Rev. B* **48**, 2827 (1993).
- ⁷⁴ S.S. Iyer and Y.H. Xie, *Science* **260**, 40 (1993).
- ⁷⁵ V. Lehmann and U. Gösele, *Appl. Phys. Lett.* **58**, 856 (1991).
- ⁷⁶ G.C. John and V.A. Singh, *Phys. Rep.* **263**, 93 (1995).
- ⁷⁷ O. Bisi, S. Ossicini, and L. Pavesi, *Surf. Sci. Rep.* **38**, 1 (2000).
- ⁷⁸ G. Ledoux, O. Guillois, D. Porterat, C. Reynaud, F. Huisken, B. Kohn, and V. Paillard, *Phys. Rev. B* **62**, 15942 (2000).
- ⁷⁹ K.H. Beckmann, *Surf. Sci.* **3**, 314 (1965).
- ⁸⁰ I.N. Lees, H. Lin, C.A. Canaria, C. Gurtner, M.J. Sailor, and G.M. Miskelly, *Langmuir* **19**, 9812 (2003).
- ⁸¹ M.J. Sailor, in *Handb. Porous Silicon*, edited by L. Canham (Springer International Publishing, Cham, 2014), pp. 355–380.
- ⁸² V. Petrova-Koch, T. Muschik, A. Kux, B.K. Meyer, F. Koch, and V. Lehmann, *Appl. Phys. Lett.* **61**, 943 (1992).
- ⁸³ K. Murakoshi and K. Uosaki, *Appl. Phys. Lett.* **62**, 1676 (1993).
- ⁸⁴ S. Shih, K.H. Jung, D.L. Kwong, M. Kovar, and J.M. White, *Appl. Phys. Lett.* **62**, 1780 (1993).
- ⁸⁵ M.P. Schwartz, F. Cunin, R.W. Cheung, and M.J. Sailor, *Phys. Status Solidi A* **202**, 1380 (2005).
- ⁸⁶ L.T. Canham, J.P. Newey, C.L. Reeves, M.R. Houlton, A. Loni, A.J. Simons, and T.I. Cox, *Adv. Mater.* **8**, 847 (1996).
- ⁸⁷ J. Salonen, V.-P. Lehto, M. Björkqvist, E. Laine, and L. Niinistö, *Phys. Status Solidi A* **182**, 123 (2000).

- ⁸⁸ A. Ghafarinazzari, V. Paterlini, P. Cortelletti, P. Bettotti, M. Scarpa, and N. Daldosso, J. Nanosci. Nanotechnol. **17**, 1240 (2017).
- ⁸⁹ A. Ghafarinazari, M. Scarpa, G. Zoccatelli, M.C. Franchini, E. Locatelli, and N. Daldosso, RSC Adv. **7**, 6724 (2017).
- ⁹⁰ J. Lu, M. Liong, Z. Li, J.I. Zink, and F. Tamanoi, Small **6**, 1794 (2010).
- ⁹¹ R.J. Martín-Palma, J. Hernández-Montelongo, V. Torres-Costa, M. Manso-Silvan, and . Munoz-Noval, Expert Opin. Drug Deliv. **11**, 1273 (2014).
- ⁹² H.A. Santos, editor, *Porous Silicon for Biomedical Applications* (Elsevier/WP Woodhead Publishing, Woodhead Publishing is an imprint of Elsevier, Amsterdam ; Boston, 2014).
- ⁹³ R. Herino, Mater. Sci. Technol. **13**, 965 (1997).
- ⁹⁴ S. Kaskel and K. Schlichte, J. Catal. **201**, 270 (2001).
- ⁹⁵ F.A. Harraz, Sens. Actuators B Chem. **202**, 897 (2014).
- ⁹⁶ R.C. Erson, R.S. Muller, and C.W. Tobias, Sens. Actuators Phys. **23**, 835 (1990).
- ⁹⁷ L. Canham, in *Handb. Porous Silicon*, edited by L. Canham (Springer International Publishing, Cham, 2014), pp. 733–740.
- ⁹⁸ M. Takahashi and N. Koshida, J. Appl. Phys. **86**, 5274 (1999).
- ⁹⁹ G. Barillaro, in *Handb. Porous Silicon*, edited by L. Canham (Springer International Publishing, Cham, 2014), pp. 845–856.
- ¹⁰⁰ D.M. Reffitt, N. Ogston, R. Jugdaohsingh, H.F.J. Cheung, B.A.J. Evans, R.P.H. Thompson, J.J. Powell, and G.N. Hampson, Bone **32**, 127 (2003).
- ¹⁰¹ L. Canham, in *Handb. Porous Silicon*, edited by L. Canham (Springer International Publishing, Cham, 2014), pp. 999–1008.
- ¹⁰² H.A. Santos, L.M. Bimbo, B. Herranz, M.-A. Shahbazi, J. Hirvonen, and J. Salonen, J. Mater. Res. **28**, 152 (2013).
- ¹⁰³ J.-H. Park, L. Gu, G. von Maltzahn, E. Ruoslahti, S.N. Bhatia, and M.J. Sailor, Nat. Mater. **8**, 331 (2009).
- ¹⁰⁴ E. Secret, M. Maynadier, A. Gallud, A. Chaix, E. Bouffard, M. Gary-Bobo, N. Marcotte, O. Mongin, K.E. Cheikh, V. Hugues, M. Auffan, C. Frochot, A. Morere, P. Maillard, M. Blanchard-Desce, M.J. Sailor, M. Garcia, J.-O. Durand, and F. Cunin, Adv. Mater. **26**, 7643 (2014).
- ¹⁰⁵ J.M. Kinsella, S. Ananda, J.S. Andrew, J.F. Grondek, M.-P. Chien, M. Scadeng, N.C. Gianneschi, E. Ruoslahti, and M.J. Sailor, Adv. Mater. **23**, H248 (2011).
- ¹⁰⁶ L.M. Bimbo, M. Sarparanta, H.A. Santos, A.J. Airaksinen, E. Makila, T. Laaksonen, L. Peltonen, V.-P. Lehto, J. Hirvonen, and J. Salonen, ACS Nano **4**, 3023 (2010).

- ¹⁰⁷ J. Kang, D. Kim, J. Wang, Y. Han, J.M. Zuidema, A. Hariri, J.-H. Park, J.V. Jokerst, and M.J. Sailor, *Adv. Mater.* **30**, 1800512 (2018).
- ¹⁰⁸ D.V. Lim, *Proc. IEEE* **91**, 902 (2003).
- ¹⁰⁹ M. Thust, M.J. Schöning, S. Frohnhoff, R. Arens-Fischer, P. Kordos, and H. Lüth, *Meas. Sci. Technol.* **7**, 26 (1996).
- ¹¹⁰ S. Chan, Y. Li, L.J. Rothberg, B.L. Miller, and P.M. Fauchet, *Mater. Sci. Eng. C* **15**, 277 (2001).
- ¹¹¹ C.-F. Wang, M.P. Sarparanta, E.M. Mäkilä, M.L.K. Hyvönen, P.M. Laakkonen, J.J. Salonen, J.T. Hirvonen, A.J. Airaksinen, and H.A. Santos, *Biomaterials* **48**, 108 (2015).
- ¹¹² E. Tasciotti, X. Liu, R. Bhavane, K. Plant, A.D. Leonard, B.K. Price, M.M.-C. Cheng, P. Decuzzi, J.M. Tour, F. Robertson, and M. Ferrari, *Nat. Nanotechnol.* **3**, 151 (2008).
- ¹¹³ J. Salonen, A.M. Kaukonen, J. Hirvonen, and V.-P. Lehto, *J. Pharm. Sci.* **97**, 632 (2008).
- ¹¹⁴ P. Ghosh, G. Han, M. De, C.K. Kim, and V.M. Rotello, *Adv. Drug Deliv. Rev.* **60**, 1307 (2008).
- ¹¹⁵ A.S.-W. Goh, A.Y.-F. Chung, R.H.-G. Lo, T.-N. Lau, S.W.-K. Yu, M. Chng, S. Satchithanatham, S.L.-E. Loong, D.C.-E. Ng, B.-C. Lim, S. Connor, and P.K.-H. Chow, *Int. J. Radiat. Oncol.* **67**, 786 (2007).
- ¹¹⁶ D.J. Savage, X. Liu, S.A. Curley, M. Ferrari, and R.E. Serda, *Curr. Opin. Pharmacol.* **13**, 834 (2013).
- ¹¹⁷ W. Li, Z. Liu, F. Fontana, Y. Ding, D. Liu, J.T. Hirvonen, and H.A. Santos, *Adv. Mater.* **30**, 1703740 (2018).
- ¹¹⁸ L. Gu, L.E. Ruff, Z. Qin, M. Corr, S.M. Hedrick, and M.J. Sailor, *Adv. Mater.* **24**, 3981 (2012).
- ¹¹⁹ C. Lee, H. Kim, C. Hong, M. Kim, S. S. Hong, D. H. Lee, and W. In Lee, *J. Mater. Chem.* **18**, 4790 (2008).
- ¹²⁰ C. Hong, J. Lee, H. Zheng, S.-S. Hong, and C. Lee, *Nanoscale Res. Lett.* **6**, 321 (2011).
- ¹²¹ V.Yu. Timoshenko, A.A. Kudryavtsev, L.A. Osminkina, A.S. Vorontsov, Yu.V. Ryabchikov, I.A. Belogorokhov, D. Kovalev, and P.K. Kashkarov, *JETP Lett.* **83**, 423 (2006).
- ¹²² L.T. Canham, C.L. Reeves, D.O. King, P.J. Branfield, J.G. Crabb, and M.C.L. Ward, *Adv. Mater.* **8**, 850 (1996).
- ¹²³ B. Godin, J. Gu, R.E. Serda, S. Ferrati, X. Liu, C. Chiappini, T. Tanaka, P. Decuzzi, and M. Ferrari, *Control. Release Newsl. Control. Release Soc.* **25**, 9 (2008).
- ¹²⁴ D. Timmerman, J. Valenta, K. Dohnalová, W.D.A.M. de Boer, and T. Gregorkiewicz, *Nat. Nanotechnol.* **6**, 710 (2011).
- ¹²⁵ S.K. Brar and M. Verma, *TrAC Trends Anal. Chem.* **30**, 4 (2011).

- ¹²⁶ G. Korotcenkov and B.K. Cho, *Crit. Rev. Solid State Mater. Sci.* **35**, 153 (2010).
- ¹²⁷ N.H. Maniya, S.R. Patel, and Z.V.P. Murthy, *Mater. Res. Bull.* **57**, 6 (2014).
- ¹²⁸ J. Coates, in *Encycl. Anal. Chem.* (American Cancer Society, 2006).
- ¹²⁹ *J. Am. Chem. Soc.* **124**, 1830 (2002).
- ¹³⁰ I.R. Rao, *Nature* **125**, 600 (1930).
- ¹³¹ K.J. Nash, P.D.J. Calcott, L.T. Canham, M.J. Kane, and D. Brumhead, *J. Lumin.* **60–61**, 297 (1994).
- ¹³² E. Chistè, A. Ghafarinazari, M. Donini, V. Cremers, J. Dendooven, C. Detavernier, D. Benati, M. Scarpa, S. Dusi, and N. Daldosso, *J. Mater. Chem. B* **6**, 1815 (2018).
- ¹³³ L. Pavesi and M. Ceschini, *Phys. Rev. B* **48**, 17625 (1993).
- ¹³⁴ J. Fuzell, A. Thibert, T.M. Atkins, M. Dasog, E. Busby, J.G.C. Veinot, S.M. Kauzlarich, and D.S. Larsen, *J. Phys. Chem. Lett.* **4**, 3806 (2013).
- ¹³⁵ V. Švrček, T. Sasaki, R. Katoh, Y. Shimizu, and N. Koshizaki, *Appl. Phys. B* **94**, 133 (2008).
- ¹³⁶ A.B. Jindal, *Int. J. Pharm.* **532**, 450 (2017).
- ¹³⁷ J.P. Best, Y. Yan, and F. Caruso, *Adv. Healthc. Mater.* **1**, 35 (2012).
- ¹³⁸ N. Mandzy, E. Grulke, and T. Druffel, *Powder Technol.* **160**, 121 (2005).
- ¹³⁹ J.S. Taurozzi, V.A. Hackley, and M.R. Wiesner, *Nanotoxicology* **5**, 711 (2011).
- ¹⁴⁰ N. Daldosso, A. Ghafarinazari, P. Cortelletti, L. Marongiu, M. Donini, V. Paterlini, P. Bettotti, R. Guider, E. Froner, S. Dusi, and M. Scarpa, *J. Mater. Chem. B* **2**, 6345 (2014).
- ¹⁴¹ N.K. Hon, Z. Shaposhnik, E.D. Diebold, F. Tamanoi, and B. Jalali, *ECS Trans.* **45**, 7 (2013).
- ¹⁴² J. Joo, J.F. Cruz, S. Vijayakumar, J. Grondek, and M.J. Sailor, *Adv. Funct. Mater.* **24**, 5688 (2014).
- ¹⁴³ K.-H. Wu, C.-W. Li, and J.-H. Liu, *Microelectron. Eng.* **148**, 70 (2015).
- ¹⁴⁴ F. Cunin, in *Handb. Porous Silicon*, edited by L. Canham (Springer International Publishing, Cham, 2014), pp. 647–663.
- ¹⁴⁵ B. Godin, E. Tasciotti, X. Liu, R.E. Serda, and M. Ferrari, *Acc. Chem. Res.* **44**, 979 (2011).
- ¹⁴⁶ S.K. Nitta and K. Numata, *Int. J. Mol. Sci.* **14**, 1629 (2013).
- ¹⁴⁷ X. Wang, H.J. Kim, P. Xu, A. Matsumoto, and D.L. Kaplan, *Langmuir* **21**, 11335 (2005).
- ¹⁴⁸ R. Müller, J. Abke, E. Schnell, F. Macionczyk, U. Gbureck, R. Mehrl, Z. Ruszczak, R. Kujat, C. Englert, M. Nerlich, and P. Angele, *Biomaterials* **26**, 6962 (2005).

- ¹⁴⁹ J.P. Martins, R. D'Auria, D. Liu, F. Fontana, M.P.A. Ferreira, A. Correia, M. Kemell, K. Moslova, E. Mäkilä, J. Salonen, L. Casettari, J. Hirvonen, B. Sarmiento, and H.A. Santos, *Small* **14**, 1800462 (2018).
- ¹⁵⁰ M.N.V. Ravi Kumar, *React. Funct. Polym.* **46**, 1 (2000).
- ¹⁵¹ H. Zhang, Y. Zhu, L. Qu, H. Wu, H. Kong, Z. Yang, D. Chen, E. Mäkilä, J. Salonen, H.A. Santos, M. Hai, and D.A. Weitz, *Nano Lett.* **18**, 1448 (2018).
- ¹⁵² D. Longrie, D. Deduytsche, J. Haemers, K. Driesen, and C. Detavernier, *Surf. Coat. Technol.* **213**, 183 (2012).
- ¹⁵³ D. Longrie, D. Deduytsche, and C. Detavernier, *J. Vac. Sci. Technol. A* **32**, 010802 (2013).
- ¹⁵⁴ R.W. Johnson, A. Hultqvist, and S.F. Bent, *Mater. Today* **17**, 236 (2014).
- ¹⁵⁵ C. Detavernier, J. Dendooven, S.P. Sree, K.F. Ludwig, and J.A. Martens, *Chem. Soc. Rev.* **40**, 5242 (2011).
- ¹⁵⁶ N. Avci, J. Musschoot, P.F. Smet, K. Korthout, A. Avci, C. Detavernier, and D. Poelman, *J. Electrochem. Soc.* **156**, J333 (2009).
- ¹⁵⁷ I. Iatsunskyi, M. Pavlenko, R. Viter, M. Jancelewicz, G. Nowaczyk, I. Baleviciute, K. Załęski, S. Jurga, A. Ramanavicius, and V. Smyntyna, *J. Phys. Chem. C* **119**, 7164 (2015).
- ¹⁵⁸ S. Mahurin, L. Bao, W. Yan, C. Liang, and S. Dai, *J. Non-Cryst. Solids* **352**, 3280 (2006).
- ¹⁵⁹ M.K. Wiedmann, D.H.K. Jackson, Y.J. Pagan-Torres, E. Cho, J.A. Dumesic, and T.F. Kuech, *J. Vac. Sci. Technol. A* **30**, 01A134 (2011).
- ¹⁶⁰ Q. Xie, Y.-L. Jiang, C. Detavernier, D. Deduytsche, R.L. Van Meirhaeghe, G.-P. Ru, B.-Z. Li, and X.-P. Qu, *J. Appl. Phys.* **102**, 083521 (2007).
- ¹⁶¹ P.G. Pai, S.S. Chao, Y. Takagi, and G. Lučovský, *J. Vac. Sci. Technol. A* **4**, 689 (1986).
- ¹⁶² A. León, P. Reuquen, C. Garín, R. Segura, P. Vargas, P. Zapata, and P.A. Orihuela, *Appl. Sci.* **7**, 49 (2017).
- ¹⁶³ C. Uboldi, P. Urbán, D. Gilliland, E. Bajak, E. Valsami-Jones, J. Ponti, and F. Rossi, *Toxicol. In Vitro* **31**, 137 (2016).
- ¹⁶⁴ U. Balachandran and N.G. Eror, *J. Solid State Chem.* **42**, 276 (1982).
- ¹⁶⁵ M.B. Gongalsky, A.Y. Kharin, L.A. Osminkina, V.Y. Timoshenko, J. Jeong, H. Lee, and B.H. Chung, *Nanoscale Res. Lett.* **7**, 446 (2012).
- ¹⁶⁶ K. Schäkel, *Exp. Dermatol.* **18**, 264 (2009).
- ¹⁶⁷ R.M. Steinman and J. Swanson, *J. Exp. Med.* **182**, 283 (1995).
- ¹⁶⁸ J. Banchereau, F. Briere, C. Caux, J. Davoust, S. Lebecque, Y.-J. Liu, B. Pulendran, and K. Palucka, *Annu. Rev. Immunol.* **18**, 767 (2000).

- ¹⁶⁹ V.P. Shirinsky and G.G. Borisenko, *Encyclopedia of Life Sciences* (John Wiley & Sons Ltd, 2007).
- ¹⁷⁰ A. Lanzavecchia and F. Sallusto, *Cell* **106**, 263 (2001).
- ¹⁷¹ R. Klippstein and D. Pozo, *Nanomedicine Nanotechnol. Biol. Med.* **6**, 523 (2010).
- ¹⁷² C. Chang and M.E. Gershwin, *J. Autoimmun.* **34**, J266 (2010).
- ¹⁷³ M. Di Gioacchino, C. Petrarca, F. Lazzarin, L. Di Giampaolo, E. Sabbioni, P. Boscolo, R. Mariani-Costantini, and G. Bernardini, *Int. J. Immunopathol. Pharmacol.* **24**, 65S (2011).
- ¹⁷⁴ J.K. Elmquist, T.E. Scammell, and C.B. Saper, *Trends Neurosci.* **20**, 565 (1997).
- ¹⁷⁵ A.F. Suffredini, G. Fantuzzi, R. Badolato, J.J. Oppenheim, and N.P. O'Grady, *J. Clin. Immunol.* **19**, 203 (1999).
- ¹⁷⁶ D.A.A. Vignali and V.K. Kuchroo, *Nat. Immunol.* **13**, 722 (2012).
- ¹⁷⁷ L.T. Canham, *Adv. Mater.* **7**, 1033 (1995).
- ¹⁷⁸ M.J. Sweetman, F.J. Harding, S.D. Graney, and N.H. Voelcker, *Appl. Surf. Sci.* **257**, 6768 (2011).
- ¹⁷⁹ A.H. Mayne, S.C. Bayliss, P. Barr, M. Tobin, and L.D. Buckberry, *Phys. Status Solidi A* **182**, 505 (2000).
- ¹⁸⁰ A.M. Noval, V.S. Vaquero, E.P. Quijorna, V.T. Costa, D.G. Pérez, L.G. Méndez, I. Montero, R.J.M. Palma, A.C. Font, J.P.G. Ruiz, and M.M. Silván, *J. Biomed. Mater. Res. A* **100A**, 1615 (2012).
- ¹⁸¹ D. Kovalev, E. Gross, J. Diener, V.Yu. Timoshenko, and M. Fujii, *Appl. Phys. Lett.* **85**, 3590 (2004).
- ¹⁸² K.M. Ainslie, S.L. Tao, K.C. Popat, and T.A. Desai, *ACS Nano* **2**, 1076 (2008).
- ¹⁸³ F. De Angelis, A. Pujia, C. Falcone, E. Iaccino, C. Palmieri, C. Liberale, F. Mecarini, P. Candeloro, L. Luberto, A. de Laurentiis, G. Das, G. Scala, and E. Di Fabrizio, *Nanoscale* **2**, 2230 (2010).
- ¹⁸⁴ B. Godin, C. Chiappini, S. Srinivasan, J.F. Alexander, K. Yokoi, M. Ferrari, P. Decuzzi, and X. Liu, *Adv. Funct. Mater.* **22**, 4225 (2012).
- ¹⁸⁵ S.P. Low, K.A. Williams, L.T. Canham, and N.H. Voelcker, *Biomaterials* **27**, 4538 (2006).
- ¹⁸⁶ C.-Y. Yang, L.-Y. Huang, T.-L. Shen, and J.A. Yeh, *Eur. Cell. Mater.* **20**, 415 (2010).
- ¹⁸⁷ E.J. Anglin, L. Cheng, W.R. Freeman, and M.J. Sailor, *Adv. Drug Deliv. Rev.* **60**, 1266 (2008).
- ¹⁸⁸ T. Tanaka, L.S. Mangala, P.E. Vivas-Mejia, R. Nieves-Alicea, A.P. Mann, E. Mora, H.-D. Han, M.M.K. Shahzad, X. Liu, R. Bhavane, J. Gu, J.R. Fakhoury, C. Chiappini, C. Lu,

- K. Matsuo, B. Godin, R.L. Stone, A.M. Nick, G. Lopez-Berestein, A.K. Sood, and M. Ferrari, *Cancer Res.* **70**, 3687 (2010).
- ¹⁸⁹ I.M. Meraz, B. Melendez, J. Gu, S.T.C. Wong, X. Liu, H.A. Andersson, and R.E. Serda, *Mol. Pharm.* **9**, 2049 (2012).
- ¹⁹⁰ N. Kawana, Y. Yamamoto, Y. Kino, and J. Satoh, 10 (n.d.).
- ¹⁹¹ B. Alberts, A. Johnson, J. Lewis, M. Raff, K. Roberts, and P. Walter, *Molecular Biology of the Cell*, 4th ed. (Garland Science, 2002).
- ¹⁹² R. E. Serda, S. Ferrati, B. Godin, E. Tasciotti, X. Liu, and M. Ferrari, *Nanoscale* **1**, 250 (2009).
- ¹⁹³ M. Donini, E. Zenaro, N. Tamassia, and S. Dusi, *Eur. J. Immunol.* **37**, 1194 (2007).
- ¹⁹⁴ R. Perret, S.R. Sierro, N.K. Botelho, S. Corgnac, A. Donda, and P. Romero, *Cancer Res.* **73**, 6597 (2013).
- ¹⁹⁵ O.S. Sjøgaard, N. Lohse, Z.B. Harboe, R. Offersen, A.R. Bukh, H.L. Davis, H.C. Schønheyder, and L. Østergaard, *Clin. Infect. Dis.* **51**, 42 (2010).
- ¹⁹⁶ Z.R. Stephen, F.M. Kievit, and M. Zhang, *Mater. Today* **14**, 330 (2011).
- ¹⁹⁷ S. Mornet, S. Vasseur, F. Grasset, and E. Duguet, *J. Mater. Chem.* **14**, 2161 (2004).
- ¹⁹⁸ J.R. McCarthy and R. Weissleder, *Adv. Drug Deliv. Rev.* **60**, 1241 (2008).
- ¹⁹⁹ C.F.G.C. Geraldles and S. Laurent, *Contrast Media Mol. Imaging* **4**, 1 (2009).
- ²⁰⁰ M. Rohrer, H. Bauer, J. Mintorovitch, M. Requardt, and H.-J. Weinmann, *Invest. Radiol.* **40**, 715 (2005).
- ²⁰¹ P. Caravan, J.J. Ellison, T.J. McMurry, and R.B. Lauffer, *Chem. Rev.* **99**, 2293 (1999).
- ²⁰² C.-H. Huang and A. Tsourkas, (2013).
- ²⁰³ E. Amstad, J. Kohlbrecher, E. Müller, T. Schweizer, M. Textor, and E. Reimhult, *Nano Lett.* **11**, 1664 (2011).
- ²⁰⁴ W.-Y. Huang, G.-L. Davies, and J. J. Davis, *Chem. Commun.* **49**, 60 (2013).
- ²⁰⁵ L. Li, W. Jiang, K. Luo, H. Song, F. Lan, Y. Wu, and Z. Gu, *Theranostics* **3**, 595 (2013).
- ²⁰⁶ J. Wahsner, E.M. Gale, A. Rodríguez-Rodríguez, and P. Caravan, *Chem. Rev.* **119**, 957 (2019).
- ²⁰⁷ R.E. Serda, N.L. Adolphi, M. Bisoffi, and L.O. Sillerud, *Mol. Imaging* **6**, 277 (2007).
- ²⁰⁸ R. Weissleder, P.F. Hahn, D.D. Stark, E. Rummeny, S. Saini, J. Wittenberg, and J.T. Ferrucci, *AJR Am. J. Roentgenol.* **149**, 723 (1987).
- ²⁰⁹ G. Kandasamy and D. Maity, *Int. J. Pharm.* **496**, 191 (2015).
- ²¹⁰ A. Roch, R.N. Muller, and P. Gillis, *J. Chem. Phys.* **110**, 5403 (1999).
- ²¹¹ A.-H. Lu, E.L. Salabas, and F. Schüth, *Angew. Chem. Int. Ed.* **46**, 1222 (2007).

- ²¹² V. Zavisova, M. Koneracka, A. Gabelova, B. Svitkova, M. Ursinyova, M. Kubovcikova, I. Antal, I. Khmara, A. Jurikova, M. Molcan, M. Ognjanović, B. Antić, and P. Kopcansky, *J. Magn. Magn. Mater.* **472**, 66 (2019).
- ²¹³ I. Antal, M. Kubovcikova, V. Zavisova, M. Koneracka, O. Pechanova, A. Barta, M. Cebova, V. Antal, P. Diko, M. Zduriencikova, M. Pudlak, and P. Kopcansky, *J. Magn. Magn. Mater.* **380**, 280 (2015).
- ²¹⁴ M.A. Agotegaray and V.L. Lassalle, *Silica-Coated Magnetic Nanoparticles: An Insight into Targeted Drug Delivery and Toxicology* (Springer, 2017).
- ²¹⁵ L. Gu, J.-H. Park, K.H. Duong, E. Ruoslahti, and M.J. Sailor, *Small* **6**, 2546 (2010).
- ²¹⁶ R.R. Castillo and M. Vallet-Regí, *Int. J. Mol. Sci.* **20**, 929 (2019).
- ²¹⁷ A. Gabizon, H. Shmeeda, A.T. Horowitz, and S. Zalipsky, *Adv. Drug Deliv. Rev.* **56**, 1177 (2004).
- ²¹⁸ J. Lu and C.-J. Tsai, *Nanoscale Res. Lett.* **9**, 230 (2014).
- ²¹⁹ T.G.F. Souza, V.S.T. Ciminelli, and N.D.S. Mohallem, *J. Phys. Conf. Ser.* **733**, 012039 (2016).
- ²²⁰ F. Granucci, I. Zanoni, and P. Ricciardi-Castagnoli, *Cell. Mol. Life Sci.* **65**, 1683 (2008).

Appendix A1: Characterization techniques

Here, the techniques used for the sample characterization are reported, organized by type of characterization.

Surface and chemical characterization

- FT-IR Spectroscopy

The surface characterization, in particular, the chemical groups present at the surface were investigated by a *Thermo Scientific, Nicolet iN10* micro-FTIR (Fourier Transform InfraRed) instrument, with a liquid nitrogen-cooled detector. A drop of each sample was deposited on a ZnSe slab and let dry with a flow of nitrogen in the case of samples in ethanol, or let evaporate in an oven at 50°C overnight in the case of aqueous samples. The spectra were acquired in transmission mode from 900 to 3600 cm^{-1} with a resolution of 4 cm^{-1} .

- Raman spectroscopy

Vibrational modes of the samples were analysed by triple-monochromator *T-64000, Horiba-Jobin Yvon* Raman spectrometer, equipped with Olympus (BX-41) microscope (100x objective), a CCD detector (256×1024 pixels) cooled by liquid nitrogen, and under water-cooled Ar/Kr gas laser (*Stabilite RM2018, Spectra Physics*) excitation. The coated pSi microparticles samples were investigated 514,5 nm laser (5 mW) with 600 s integration time.

SPIONs were investigated by *Thermo Scientific, DXR2* Raman microscope equipped with a 633 nm laser (3mW power) and single exposure CCD detector.

- XRD (X-ray Diffraction) spectroscopy

The presence of crystalline phases was investigated by *Thermo ARL X'TRA* powder diffractometer, equipped with a copper anode X-rays source ($K\alpha$, $\lambda = 1.5418 \text{ \AA}$) and Peltier Si (Li) cooled solid-state detector.

- ζ -potential measurement (Dynamic light scattering)

The microparticles surface charge (ζ -potential) was analysed by Zetasizer Nano-SZ (Malvern) instrument, with a 633 nm laser beam. The ζ -Potential was determined

after resuspension of the microparticles in phosphate-buffered saline (PBS at pH 7.4). The measurements were performed at 25 °C, repeated three times and averaged. Before the measurements, the samples were sonicated in a thermal bath for 45 minutes to homogenize the samples and reduce the agglomeration.

Optical characterization

- Fluorescence spectroscopy

Fluorescence spectroscopy was used to determine steady-state and time-resolved photoluminescence. The samples under investigation were analysed by a *Horiba Jobin-Yvon Nanolog* Spectrofluorometer, with a 54W xenon lamp and PMT detector.

The samples photoluminescence (PL) spectra were acquired by excitation at 350 nm, 3 nm slit size, 1200 g/mm density grating (blazed at 500 nm), 0.2 s integration time and with a 370 nm cut-off filter. For the PLE experiments, PL was investigated for each sample as a function of the exciting wavelength, which was varied from 325nm to 450nm, with a step of 25nm. Photoluminescence decay curves were studied by TCSPC (time-correlated single-photon counting) method.

The PL lifetime of the orange-red band (600 - 700 nm, characterized by μ s range lifetime) was analysed by a xenon pulsed lamp with a pulse width of 1.1 μ s, exciting at 325 nm and fixing the emission at the maximum wavelength of the PL band for each sample. The lifetime values τ were obtained by fitting the decay curve with a stretched exponential $I = I_0 e^{-(t/\tau)^\beta}$, where β is the stretched parameter. The lifetime of the small blue band, characterized by ns range lifetime, was investigated by a 335 nm nanoLED source with a pulse width < 1 ns. The emission wavelength was fixed at 420 nm (i.e. the centre of the blue band) and the data were fitted with an exponential decay curve, $I = I_0 e^{-(t/\tau)}$, to obtain the average lifetime.

The light efficiency of the samples was evaluated by quantum yield (QY) measurements by means of the comparative method,¹²⁴ where the unknown QYs is determined from a known QY_r of a reference material through the following formula, where “s” and “r” refers to “sample” and “reference”, respectively

$$QY_s = QY_r \frac{I_s}{I_r} \frac{A_r}{A_s} \left(\frac{n_s}{n_r} \right)^2$$

The integrated emission intensity (I) is recorded as a function the absorbance A of the sample and n is the refractive index of the buffer solution. For the measurements to be reliable and to minimize the non-uniform radiation, the concentration of the sample was less than 0.1 mg/mL. pSi-COOH microparticles were used as standard, whose QY was previously determined with respect to Rhodamine 101 and Fluorescein.¹⁴⁰

Structural and morphological characterization

- Size measurement (Dynamic light scattering)

The microparticles size distribution were analysed by Zetasizer Nano-SZ (Malvern) instrument, with a 633 nm laser beam. The size measurements were performed at 25 °C in ethanol, repeated three times and averaged. Before the measurements, the samples were sonicated in a thermal bath for 45 minutes to homogenize the samples and reduce the agglomeration.

- TEM (Transmission electron microscopy) – EDS (energy dispersive X-rays spectroscopy)

Dimension, shape and microparticles size were analysed by TEM imaging, with a Philips CM12 microscope operating at 120 keV, after depositing a drop of each sample (about 30 µL) on a copper grid coated with a perforated carbon film. The coupling to the EDS (Energy dispersion X-Ray) spectroscopy allows the chemical composition analysis. The integration spectrum relative to the diffraction pattern obtained by TEM was evaluated by using the software *ProcessDiffraction*.

- S/TEM (Scanning transmission electron microscopy) – EDS (energy dispersive X-rays spectroscopy)

S and TEM (Scanning and Transmission electron microscopy) analysis was performed with an S/TEM ThermoFisher Talos F200S operating at 200 kV. The microscope is equipped with an integrated EDS (Energy Dispersive X-rays Spectroscopy) system with two windowless silicon drift detectors (SDD). The samples were observed in both TEM and STEM, which allows evaluating the actual elemental distribution in the sample collecting EDS maps. To support the samples during the observation it was dissolved PBS (and then water), a 50 µL drop of those solutions

was deposited on a TEM copper support grids covered by a holey amorphous carbon film.

- SEM (Scanning electron microscopy)

The morphology of the samples was studied by SEM Jeol JSM IT300 operating at 20 keV in high vacuum condition. The sample preparation consists in the deposition of a drop of each sample (about 30 μL) on a copper grid coated with a perforated carbon film.

Magnetic characterization

- MRI (magnetic resonance imaging)

The magnetic properties of the samples were investigated by using a *Pharmascan* system operating at 7 T (*Bruker, Germany*).

Each sample under investigation was prepared in different concentrations and stored in Eppendorf vials, which were placed in a polystyrene box, to be imaged at the same time. The longitudinal (T_1) and transversal (T_2) relaxation times were measured by acquiring an MSME (multi-spin multi-echo) pulse sequence [26]. It consists of a 90° excitation RF pulse, followed by repeated 180° refocusing pulses, separated by a constant interval or echo-time. The signals coming from each point of the images were mediated to obtain the relaxation curve decays, that were fitted with an exponential decay function to obtain the T_1 and T_2 values.

Afterwards, the longitudinal and transversal relaxivities r_1 and r_2 were determined by plotting the relaxation rate against the sample concentration and fitting the data with the formula:

$$\frac{1}{T_i} = \frac{1}{T_{i,0}} + r_i \cdot c$$

Appendix A2: In-vitro cellular studies

Cytotoxicity and immune response evaluation

- alamarBlue® assay

The monocytes, dendritic cell and lymphocytes cell viability was evaluated using an alamarBlue® assay (Invitrogen, Thermo Fischer Scientific, Waltham, MA, USA) under the manufacturer's instructions. alamarBlue® is a colourimetric redox assay of metabolic activity, which contains a fluorescent blue dye (resazurin), that becomes highly pink fluorescent when it is reduced: the higher the emission, the higher the number of living cells. The cells were incubated for 24 hours with different microparticle concentrations, the reagent was added to the culture medium at 10% concentration and then, the absorbance was measured at 570 and 600 nm.

- ELISA assays

Enzyme-linked immunosorbent assay (ELISA) was used to estimate the cytokine production in culture supernatants: TNF- α , IL-6 and IL-12 presence was investigated. After DCs stimulation with microparticles (for 24 hours), the supernatants were collected. The protein levels of TNF- α (4–500 pg/mL), IL-6 (10–1000 pg/mL) and IL-12 (p70) (6–600 pg/mL) were tested by ELISA development kits purchased from Mabtech (Nacka Strand, Sweden). The plates were read at 450 nm using a *Perkin Elmer Victor 1420 Multilabel Counter (Waltham, MA, USA)*.

- Superoxide anion production

The superoxide anion production was evaluated by Cytochrome C reduction assay²²⁰. The cell culture medium is replaced with HBSS at pH 7.4, containing 80 mM ferricytochrome C and the required stimulus. The reduction of Cytochrome C was assessed by measuring the absorbance at 550 nm by *ELx808t Absorbance Microplate Reader (BioTek Instruments, Inc)*.

The statistical analysis was performed by one-way ANOVA followed by the Dunnett's Multiple Comparison Test, by considering statistically significant the p-values lower than 0.05.

Cell imaging

- TEM (Transmission electron microscopy)

The up-taking of the pSi-TiO₂ microparticles by DCs was evaluated by TEM Morgagni 268D Electron microscope (Philips). The sample was prepared by 2 h fixation in 2% glutaraldehyde in Sorensen buffer (pH 7.4), 2 hours fixation in 1% OsO₄ in aqueous solution, dehydrated in graded concentrations of acetone and then, embedded in an Epon–Araldite mixture (Electron Microscopy Sciences, Fort Washington, PA). The sample was cut into 1 mm-thick section, examined by light microscopy and stained with toluidine blue. Then, ultrathin section, of about 70 nm, was cut and deposited on Cu/Rh grids by an Ultracut E (Reichert, Wien, Austria).

- Two-photon absorption (2PA) experiments

The two-photon absorption (2PA) experiments were performed by Multiphoton microscope TCS SP5 AOBS (Leica), with a Chameleon ULTRA II laser (Coherent) and a 20 objective, immersed in water, with an NA of 1, to verify if the microparticles were still luminescent after the cell internalization. The DCs incubated with pSi microparticles were washed with PBS and deposited on a microscope slide for the observation. The sample was observed by 488 nm laser in total reflection modality. The fluorescence images were obtained upon 700 nm excitation (perfectly matching the 350 nm excitation of standard PL measurements) and z-stack images were acquired and merged to obtain a maximum projection image.